

Gasdynamic performance in relation to the power extraction of an MHD generator

Citation for published version (APA):

Masse, P. (1983). *Gasdynamic performance in relation to the power extraction of an MHD generator*. [Phd Thesis 1 (Research TU/e / Graduation TU/e), Electrical Engineering]. Technische Hogeschool Eindhoven. <https://doi.org/10.6100/IR58843>

DOI:

[10.6100/IR58843](https://doi.org/10.6100/IR58843)

Document status and date:

Published: 01/01/1983

Document Version:

Publisher's PDF, also known as Version of Record (includes final page, issue and volume numbers)

Please check the document version of this publication:

- A submitted manuscript is the version of the article upon submission and before peer-review. There can be important differences between the submitted version and the official published version of record. People interested in the research are advised to contact the author for the final version of the publication, or visit the DOI to the publisher's website.
- The final author version and the galley proof are versions of the publication after peer review.
- The final published version features the final layout of the paper including the volume, issue and page numbers.

[Link to publication](#)

General rights

Copyright and moral rights for the publications made accessible in the public portal are retained by the authors and/or other copyright owners and it is a condition of accessing publications that users recognise and abide by the legal requirements associated with these rights.

- Users may download and print one copy of any publication from the public portal for the purpose of private study or research.
- You may not further distribute the material or use it for any profit-making activity or commercial gain
- You may freely distribute the URL identifying the publication in the public portal.

If the publication is distributed under the terms of Article 25fa of the Dutch Copyright Act, indicated by the "Taverne" license above, please follow below link for the End User Agreement:

www.tue.nl/taverne

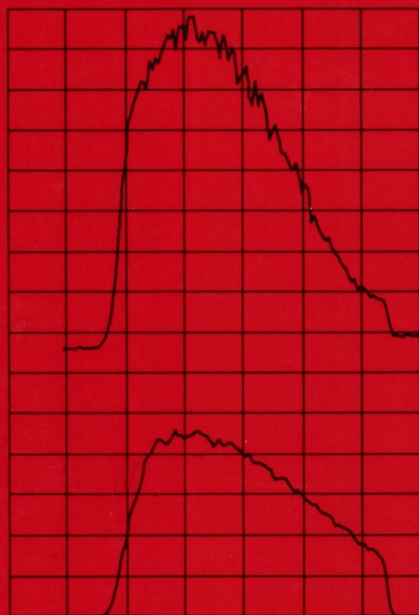
Take down policy

If you believe that this document breaches copyright please contact us at:

openaccess@tue.nl

providing details and we will investigate your claim.

**GASDYNAMIC PERFORMANCE
IN RELATION TO
THE POWER EXTRACTION OF
AN MHD GENERATOR**



P. MASSEE

**GASDYNAMIC PERFORMANCE
IN RELATION TO
THE POWER EXTRACTION OF
AN MHD GENERATOR**

PROEFSCHRIFT

**TER VERKRIJGING VAN DE GRAAD VAN DOCTOR
IN DE TECHNISCHE WETENSCHAPPEN AAN DE
TECHNISCHE HOGESCHOOL EINDHOVEN, OP GEZAG
VAN DE RECTOR MAGNIFICUS,
PROF. DR. S.T.M. ACKERMANS,
VOOR EEN COMMISSIE AANGEWEEZEN
DOOR HET COLLEGE VAN DEKANEN IN HET
OPENBAAR TE VERDEDIGEN OP
VRIJDAG 23 DECEMBER 1983 TE 16.00 UUR**

DOOR

PETER MASSEE

GEBOREN TE AMSTERDAM

Dit proefschrift is goedgekeurd
door de promotoren

Prof. Dr. L.H.Th. Rietjens

en

Prof. Dr. Ir. J.A. Steketee

Co-promotor

Dr. Ir. J.H. Blom

Aan Anja
Aan mijn ouders
Aan mijn kinderen

The figure on the front page shows the coupling between gasdynamical and electrical phenomena. The upper curve shows the pressure in the second half of the MHD generator as a function of time during run 302. The lower curve shows the electric power during run 302 on the same time scale. More details on these curves can be found in chapter 4.

This work was performed as a part of the research program of the group Direct Energy Conversion of the Eindhoven University of Technology, the Netherlands.

The research project is supported by the Department of Economic Affairs of the Netherlands.

ERRATUM

page 68 - the last sentence should read:

The calculation of the Reynolds analogy parameter $\alpha = 2St/C_{fr}$ then follows from empirical relations in terms of the friction velocity v^* already defined in (2.66) and the Stanton number for the laminar sublayer St^* in the form

$$St^* = 2\left(\frac{v^*k^*}{v_t}\right)^{-0.45} Pr_t^{-0.8}$$

$$\alpha = \left(1 + \frac{v^*}{u_\infty St^*}\right)^{-1} \quad (2.108)$$

Contents

Summary	7
Nomenclature	8
1. Introduction	14
1.1 Background	14
1.2 Review of related work	18
1.3 Scope of the present work	23
2. Theoretical description of turbulent boundary layer development	24
2.1 Formulation of the problem	24
2.2 The basic equations of MHD flows	29
2.3 The core flow equations	41
2.4 The integral boundary layer equations	43
2.5 The coupling of the core flow and the boundary layer	50
2.6 Velocity and enthalpy profiles in MHD and in non-MHD boundary layers; a review of the literature	51
2.7 Relations for a normal shock wave interacting with the boundary layer	61
2.8 Relations for the skin friction and the heat transfer coefficients and for the dissipation integral	64
2.9 The calculation of the voltage drop and the current density displacement thickness	71
3. Results of numerical calculations	75
3.1 Quasi-one-dimensional MHD flow model	76
3.2 The model of MHD core flow and non-MHD boundary layers	77
3.3 The model of MHD core flow and MHD boundary layers	80
Figures 8 to 25	83

4. Experimental results	92
4.1 Description of the experimental set up	92
4.2 Electrical behaviour of the generator	94
4.3 Gasdynamical behaviour of the hot flow train	100
Figures 26 to 39	109
5. Confrontation of theory and experiment	123
5.1 A review of the numerical model which will be verified	123
5.2 Analysis of the electrical performance	130
5.3 Analysis of the gasdynamical behaviour	137
Figures 41 to 51	141
6. Conclusions and recommendations	147
References	150
Appendix A. Useful relations between MHD boundary layer thicknesses and parameters.	157
Samenvatting	158
Acknowledgement	159
Curriculum vitae	160

Summary

A study of the gasdynamical processes in MHD generators has been made both theoretically and experimentally. These processes are strongly influenced by the power production of the MHD generator. The experimental part of the study has been performed in the 5 Mwt blow-down facility which is in operation at the Eindhoven University of Technology. Under the influence of the MHD interaction the measured profile of the static pressure shows a strong increase in the second half of the generator, which can be explained by thick boundary layers. Such a situation can not be described by the usual quasi-one-dimensional model in which the effects of friction and heat conduction are smeared out over the circumference of the channel cross-section. Therefore a core flow and boundary layer model has been developed. In order to obtain a fast computer code which can be used for engineering purposes the quasi-one-dimensional approximation is used. It is shown in this thesis that the boundary layers have to be calculated from integral equations describing momentum, kinetic energy and stagnation enthalpy respectively, when the MHD effects in the boundary layers are properly taken into account. Calculations with the developed core flow and boundary layer model have shown that the electrical power output is limited by the design of the existing facility and have indicated possibilities to circumvent this limitation. In the process of confrontation of theory and experiment it has appeared that the model can also indicate shortcomings in the operation of the MHD generator. In particular it has been shown that the operation of the MHD generator has been limited up to now by Hall shorting. Special future experiments are recommended in order to study whether Hall shorting can be avoided. A complete validation of the developed model has to wait for the results of these future experiments.

Nomenclature

A	geometrical channel cross-section
A*	coefficient in the approximation for the current density (eq. 2.122).
A _{eff}	effective channel cross-section or core area (eq. 2.62)
a	coefficient in eq. (2.74)
a'	coefficient in eq. (2.106)
\vec{B}	magnetic induction vector
B	magnitude of the magnetic induction
B'	constant in eq. (2.65)
B*	coefficient in the approximation for σ_{app} (eq. 5.3)
b	coefficient in eq. (2.74) (section 2.6 only), channel width
b'	coefficient in eq. (2.106)
C	perimeter of the generator cross-section
C*	coefficient in the approximation for σ_{app} (eq. 5.13)
C _D , C _{D,q}	dissipation integral
C _{D0}	dissipation integral without MHD effects (eq. 2.114)
C _{DS}	dissipation integral for smooth wall conditions
C _f , C _{f,q}	friction coefficient
C _{f0}	friction coefficient without MHD effects (eq. 2.114)
C _{fr}	rough wall friction coefficient
C _{fr} *	Schlichting's rough wall friction coefficient (eq. 2.112)
C _{fs} *	Schlichting's smooth wall friction coefficient (eq. 2.112)
C _p	specific heat at constant pressure
D _q	logarithmic derivative of the side-wall width (eq. 2.47)
d _s	thickness of a radiating plasma slab (eq. 2.30)
\vec{E}	electric field vector
\vec{E}^*	electric field vector in moving coordinate system = $\vec{E} + \vec{u} \times \vec{B}$
E*	magnitude of the electric field in moving coordinate system
E _I	ionization potential
e	charge of the electron
F _{Rx} , F _S , F _δ	functions in the expressions for the friction coefficient (eq. 2.104 and 2.105)
H	stagnation enthalpy
<H>	stagnation enthalpy averaged over the channel cross-section

\bar{H}_{12} , $\bar{H}_{12,q}$	incompressible boundary layer shape factor ($= \bar{\delta}_{1,q}/\bar{\delta}_{2,q}$)
h	static enthalpy (section 2.2 only), height of generator
h'	turbulent static enthalpy fluctuation
h_{eff}	effective height of generator (eq. 5.7)
I_{el}	current per electrode pair
I_n	current of electrode pair n
\vec{j}	electric current density vector
j	magnitude of the electric current density
k	Boltzmann's constant
k^*	roughness height (eq. 2.65 and 2.108)
k_f	ionization rate coefficient
k_r	recombination rate coefficient
L_r	current relaxation length
l	Prandtl's mixing length (eq. 2.70)
M	Mach number
$M_{\alpha\beta}$	Hall tensor (eq. 2.28)
\dot{m}	mass flow rate
m_A	mass of an argon atom or ion
m_C	mass of a cesium atom or ion
m_e	mass of an electron
m_j	mass of species j
N	exponent in the boundary layer profile (eq. 2.56)
N^*	MHD interaction parameter
N_e	exponent in the velocity profile for the electrode wall boundary layer (eq. 2.87)
N_s	number of streamers per sec
Nu_x	Nusselt number expressed in terms of x
n	total number density
n^*	exponent in eq. (2.109)
n_A	number density of argon atoms and ions
n_C	number density of cesium atoms and ions
n_a	number density of atoms
n_e	number density of electrons
n_i	number density of ions
P_e	electrical power output of the generator
Pr_t	turbulent Prandtl number
p	total static pressure

p_{dk}	static pressure in the diffuser at location k
p_{gk}	static pressure in the generator at location k
p_s	stagnation pressure
$\langle p_s \rangle$	stagnation pressure averaged over the channel cross-section
Q	parameter in eq. (2.83)
ΔQ	excess heat flux to the wall due to Joule dissipation in the boundary layer (eq. 2.85)
Q_{ea}	electron-atom momentum transfer cross-section
Q_{ei}	electron-ion momentum transfer cross-section
Q_j	momentum transfer cross-section ($j = ea, ei$)
Q_0	heat flux to the wall without MHD effects in the boundary layer (eq. 2.85)
\vec{q}	heavy species heat flux vector
\vec{q}_e	electron heat flux vector
R	gas constant for the argon-cesium mixture
\dot{R}	radiation loss (eq. 2.30)
R_{BL}	resistance due to the boundary layer (fig. 5)
$Re_\delta, Re_{\delta_2}, Re_x$	Reynolds number expressed in terms of δ, δ_2 or x respectively
R_f	roughness factor (eq. 2.112)
R_i	overshoot parameter for the insulator wall boundary layer (eq. 2.91)
R_{in}	internal resistance of a generator segment (eq. 5.6)
R_L	load resistance
R_s	resistance due to the Debye sheath (fig. 5)
r	recovery factor (eq. 2.81)
S, S_0	parameters in eq. (2.83)
St, St_q	Stanton number
St_0	Stanton number without MHD effects in the boundary layer (eq. 2.113 and 2.114)
St^*	Stanton number of the laminar sublayer (eq. 2.108)
s	electrode pitch
sr	seed ratio
T	heavy species temperature
T_{aw}	adiabatic wall temperature
T_e	electron temperature
$\langle T_s \rangle$	stagnation temperature averaged over the channel cross-section

t	time
U	dimensionless velocity in the boundary layer ($= u/u_\infty$)
U_T	dimensionless velocity at the laminar-turbulent transition point in the velocity profile (eq. 2.86)
\vec{u}	heavy species flow velocity vector
u	x-component of the heavy species flow velocity
\vec{u}_e	electron drift velocity vector
u_{eff}	van Driest effective velocity (eq. 2.78)
u'_α, u'_β	turbulent fluctuation in velocity components
Δu_1	wall roughness correction factor (eq. 2.105)
Δu_2	pressure gradient correction factor (eq. 2.105)
V_{el}	potential difference between the electrodes of a generator segment
V_H	local Hall potential (with respect to $x = 0$)
$V_k V_l$	Hall potential difference between electrode k and electrode l
ΔV	total voltage drop
$\Delta V_{an}, \Delta V_{cat}$	anode and cathode voltage drop
v	y-component of the heavy species flow velocity
v^*	friction velocity (eq. 2.66)
w	z-component of the heavy species flow velocity
x	Cartesian coordinate
x_r	distance along a rough flat plate (eq. 2.111)
x_s	distance along a smooth flat plate (eq. 2.111)
x_α, x_β	Cartesian coordinates for $\alpha, \beta = 1, 2, 3$ respectively
y	Cartesian coordinate
y'	transformed y-coordinate (eq. 2.57)
z	Cartesian coordinate
α, α_q	Reynolds analogy parameter (eq. 2.108)
α^*	pressure gradient parameter (eq. 2.82)
β	Hall parameter
β'	Clausner's equilibrium parameter (eq. 2.68)
β^*	heat transfer parameter (eq. 2.81)
β_{app}	apparent Hall parameter (section 5.1)
β_{crit}	critical Hall parameter
β_{eff}	effective Hall parameter (section 2.2.3)
γ	ratio of specific heats
γ^*	compressibility parameter (eq. 2.81)

γ_t	coefficient in eq. (2.109)
δ	energy loss factor (section 2.2), boundary layer thickness
δ', δ'_q	transformed boundary layer thickness (eq. 2.57)
$\delta_1, \delta_{1,q}$	displacement thickness
$\delta_2, \delta_{2,q}$	momentum thickness
$\delta_3, \delta_{3,q}$	kinetic energy thickness
$\delta_{4,q}$	density defect thickness
$\delta_{Ej,q}$	power density displacement thickness (eq. 2.54)
$\delta_H, \delta_{H,q}$	stagnation enthalpy thickness
$\delta_{j,q}$	current density displacement thickness (eq. 2.44)
$\delta_{ju,q}$	displacement thickness for the moment of the current density (eq. 2.49)
δ_T	thickness of the temperature boundary layer
δ_u	thickness of the velocity boundary layer
η_{ent}	enthalpic efficiency
θ	wall temperature parameter (eq. 2.106)
κ	heat conduction coefficient of heavy species
κ'	Von Kármán's mixing length constant (eq. 2.71)
κ_e	heat conduction coefficient of electrons
κ_t	turbulent heat conduction coefficient of heavy species
λ	boundary layer parameter (eq. 2.100 and 2.101)
λ_{in}	characteristic length for the inertia of electrons (eq. 2.10)
μ	viscosity coefficient of heavy species
μ_t	turbulent viscosity coefficient of heavy species
ν_j	collision frequency of electrons and species j
ν_t	turbulent kinematic viscosity ($= \mu_t/\rho$)
ξ	integration variable (section 2.4.1 only), dimensionless
\tilde{y}	transformed y-coordinate (eq. 2.57)
$\tilde{\pi}$	wake parameter (eq. 2.65)
ρ	mass density
ρ'	turbulent mass density fluctuation
ρ_u	external specific resistivity (eq. 5.9)
σ	electrical conductivity
σ_{app}	apparent electrical conductivity (section 5.1)
σ_{eff}	effective electrical conductivity (eq. 2.32)
$\tau_{\alpha\beta}$	shear stress tensor (eq. 2.11)
τ_t	turbulent shear stress (section 2.6.2)

ϕ parameter in eq. (2.83)

Subscripts

A argon
C cesium
q denotes either the electrode wall ($q = e$) or the insulator wall boundary layer ($q = i$)
w wall
x,y,z Cartesian coordinate components
x upstream of a normal shock wave (section 2.7 only)
y downstream of a normal shock wave (section 2.7 only)
 ∞ core flow
 α, β tensor indices

Superscript

— time average (section 2.2.1 only), incompressible

1. Introduction

1.1 Background

Although the recent reduction in the price of crude oil and frequent discoveries of new oil and gas fields have influenced the public to believe that the energy problem is not a serious one, the opposite must be feared. Especially when the economies in the Western world recover from the present low level of activities, the energy consumption will increase and the oil and gas prices can be expected to rise again. The importance of increasing the efficiency of energy conversion systems remains therefore unimpaired and the MHD topping system is one of the possibilities. This potential for MHD results from the fact that it opens up the possibility to use a larger range of temperatures for the generation of electric power. According to thermodynamics this leads to an increase in efficiency in comparison with modern steam systems.

Three different MHD systems can be distinguished in view of the working medium which passes through the MHD generator.

In a liquid metal MHD generator kinetic energy is converted into electric energy. The crucial problem is how to increase the kinetic energy of the incompressible medium efficiently before it enters the MHD generator. This is often done by making the medium compressible by mixing it with a gas and accelerating it through a nozzle. It is, however, very difficult to control the behaviour of the two-phase fluid in the flow train and especially in the generator. Besides the gas has to be separated from the liquid metal before the medium enters the heat source and the separation process has a low efficiency. Therefore the liquid metal system has little attraction for large scale power generation systems [Hol] and the amount of work in this area has been limited. It is, however, proposed for special applications such as space missions and recently also as a system for the conversion of solar energy [Geyl].

In an open cycle MHD generator the combustion products of a fossil fuel are directly used as the working medium. The combustion temperature has to reach 2700 K and the fuel is seeded with an alkali metal compound so that a plasma with sufficient electrical conductivity is obtained. This system is very promising for countries with large supplies of fossil fuel and is in an advanced state of development especially in the USA and the USSR. In the USA the development is oriented entirely towards direct coal burning. The progress in performance and operating time is illustrated in figure 1. In this figure some points for the closed cycle MHD system have also been included. The difference in the state of development between the two systems is very noticeable as illustrated by this figure. One point which can not be illustrated in the figure has to be mentioned here. This is the fact that in Russia the construction has begun of the U500 in Ryazan, 250 km from Moscow. This 500 MWe power plant will generate 250 MWe from the MHD topping system and is planned to come into operation in

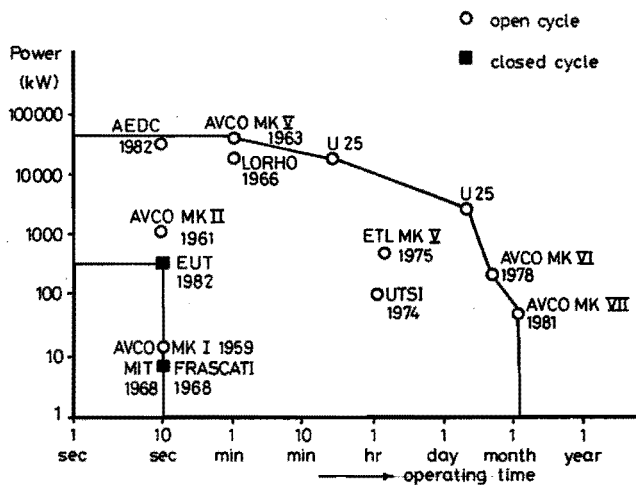


Fig. 1 Progress in the performance of major MHD generator experiments. (Note that the horizontal scale is nonlinear).

1986. The power plant will be fired with natural gas but the next generation of power plants should demonstrate coal burning MHD power generation.

The closed cycle MHD system has obtained its name from the fact that the working medium is not exhausted into the atmosphere as in the open cycle system. Instead it is recompressed downstream of the generator and then fed back to the heat source. This is necessary because of the expensive working medium, consisting of a noble gas seeded with an alkali metal. Until 1972 the gas cooled nuclear reactor was considered to be the heat source for the closed cycle MHD system. At that time an examination of the requirements that this nuclear reactor had to meet, led to the conclusion that a time of at least 15 years and a multi-billion dollar budget would be necessary for the development of a suitable reactor. The conclusion that the heat source for the closed cycle system would not be available in a reasonable time led countries as England, France, Germany, Italy and Sweden to discontinue their efforts in the MHD field. Therefore the closed cycle MHD system is now lagging behind in development with respect to the open cycle system. At present a system of regenerative heat exchangers is considered a suitable heat source for the closed cycle MHD system. This has the advantage that it can also be heated by coal firing. The drawback is the investment cost for the heat exchangers which determines to a large extent the cost of electricity. If the maximum cycle temperature can be lowered from 2000 to 1700 K a recuperative heat exchanger can be used as the heat source [Rot1] and the disadvantage of high cost can be avoided. Since the efficiency of the open cycle MHD system decreases due to increasing heat losses of the MHD generator in the range of power from 200 MWe down, the closed cycle system is an attractive alternative for smaller unit sizes.

At the Eindhoven University of Technology (EUT) the effort in closed cycle MHD has been a continuous one since 1965. In shock-tunnel MHD experiments both at EUT and at General Electric (GE) USA power densities up to 140 MW/m^3 and enthalpy extractions up to 24% have been achieved over test times of about 5 msec. At an inlet

stagnation temperature of 2000 K and a magnetic induction of 3 T an enthalpy extraction up to 11.5% has been measured [Veel]. In 1975 GE proposed to approach more realistic test times and generator conditions by building a 50 MWt blow-down experiment [Zal] but did not obtain the necessary funding. Around the same time similar plans arose at EUT and in 1976 the Department of Economic Affairs of the Netherlands supported this plan and the construction of a 5 MWt blow-down experiment was started. Up to now five measurement series have been performed in which a maximum electric power of 360 kW has been generated. Apart from the increase in test time with respect to the shock-tunnel experiment from 5 msec to 10 sec the EUT blow-down experiment offers an increase in magnetic induction from 3 to 5.3 T and the Ar - Cs plasma is heated in a realistic heat source namely a propane fired regenerative heat exchanger.

In addition to different MHD systems also various forms of the MHD generator itself have been developed. In the present study, however, the attention is focussed exclusively on the processes occurring in linear closed cycle MHD generators in the segmented Faraday configuration (figure 2). The operation of the MHD generator results from the fact that an electric field E_{ind} is created in an electrically conducting gas flowing through a magnetic field perpendicular to the flow direction. Due to the fact that the current in the generator is carried almost completely by the electrons a so called Hall electric field is created in the axial direction. In order to avoid a shorting of the Hall field the upper and lower wall electrodes are segmented. Each electrode segment is insulated from its neighbours and is connected to a separate resistor acting as the load.

This study is devoted to the development of a core flow and boundary layer model in a quasi-one-dimensional approximation. This model is needed for the description of the electrical and gasdynamical behaviour under conditions of substantial MHD interaction. This insight has resulted from the measured distribution of static pressures along the MHD generator of the EUT blow-down experiment. These measurements show a strong increase of

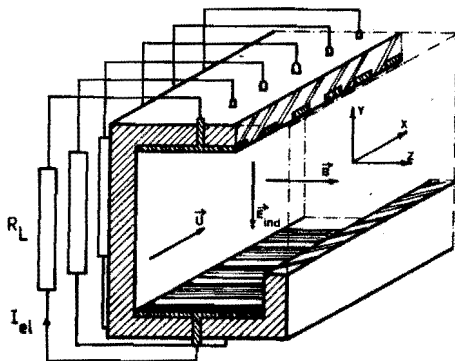


Fig. 2 Principle of a segmented Faraday generator \vec{u} denotes the velocity of the plasma, \vec{B} the magnetic induction, I_{el} the current through a generator segment and R_L the load of that segment.

static pressure in the second half of the MHD generator, which can only be explained by very thick boundary layers or possibly by shocks in the generator channel. The quasi-one-dimensional approximation is used in order to develop a fast computer code for engineering purposes.

1.2 Review of related work

MHD boundary layers have been investigated theoretically by several authors but experimentally far less work has been done. In describing the various theories the attention will be focussed exclusively on closed cycle compressible MHD flows. Thus the medium consists of several components namely free electrons, alkali metal ions and atoms and noble gas ions and atoms. Because of the limited amount of experimental information, also results from open cycle experiments will be mentioned when they can be of importance for the present work.

Theoretical studies

The treatment of the boundary layer and the gasdynamic equations by various investigators differs primarily in the method of solution and the description of the interaction between the plasma and the wall. Kerrebrock [Ke1, Ke2] carried out some early attempts to analyse MHD boundary layers. The electron energy equation was neglected and an equilibrium plasma was assumed. Later Hale and Kerrebrock [Hal1] allowed for the dependence of the electrical conductivity on the current density by means of an algebraical relation. Local similarity was assumed in all previous work. Sherman and Reshotko [Sh1, Sh2] considered a steady laminar, two-dimensional boundary layer in a cesium seeded argon plasma. They assumed that the electron density was determined by the Saha equation in [Sh1] but allowed for finite rates in [Sh2]. The equations were solved by means of a finite difference scheme. Cott [Cot1] studied the boundary layer over the insulator wall of an MHD accelerator and took finite reaction rates and ambipolar diffusion into account. The numerical solution was obtained by means of the finite difference scheme of Patankar and Spalding [Pa1]. All the work mentioned so far has been for laminar flow. Merck [Me1] obtained a solution for the turbulent boundary layer in an MHD generator along the insulator wall by using the eddy viscosity concept. The solution is not truly two-dimensional since the axial gradients of pressure and temperature follow from a one-dimensional approximation and are fixed parameters when the boundary layer equations are solved. High and Felderman [Hi1] extended the work of Cott to turbulent flow using the eddy viscosity concept and assuming a collisionless sheath along the wall. Demetriades [De1] and Argyropoulos [Ar1] indicated that the key in determining the behaviour of a closed cycle MHD generator is to separate the problem into two parts. In the gasdynamic part the current or electric field distribution is known and in the electrical part of the problem the gasdynamic parameters are treated as known. These two partial solutions can then be used to get the complete solution by means of an iteration procedure. Doss [Do1] extended the work of Sherman and Reshotko and showed the influence of segmentation, ambipolar diffusion and finite rate

effects. Doss took the electron gas equations into account but used prescribed profiles of current density and electric field which are approximate solutions of the Maxwell equations. Doss mainly concentrated on the profiles for electron density and electron temperature in the electrode wall boundary layer. Snel and Lindhout [Snl] obtained a two-dimensional solution at the insulator wall in which the interaction between the core flow and the boundary layer is accounted for. They also improved on the electrical part of the problem by using the complete solution of Houben [Hol] as input into their program. Pian and Merck [Pil] again considered the electrode wall boundary layer and extended the approach of Doss to a situation where boundary layer separation occurs. They considered laminar boundary layers and used a similar approximate solution for the electrical part of the problem as used by Doss. They do not solve the equations for the electron gas, however, but use the algebraic relation between the electrical conductivity and the electric current density introduced by Hale and Kerrebrock. A strong influence of segmentation is found since the skin friction decreases rapidly at each end of an electrode until finally $C_f=0$ and thus separation is reached. Arts and Merck [Artl] have extended the work of Pian and Merck to turbulent flow and tried both the approximate solution of Doss and the complete solution of Houben for the electrical part of the problem. They use the Saha equation and assume the energy equation of the electrons to be in equilibrium to calculate profiles of electron density and electron temperature. Arts and Merck concentrate on the electrode wall boundary layer and find undistorted velocity profiles but gas temperature profiles with a distinct overshoot. They conclude that a very accurate calculation of the Joule heating in the boundary layer is necessary in the finite difference approach, in order to be able to predict correctly the separation of the electrode wall boundary layer.

Up to this point integral methods have not been discussed since they represent a completely different approach of boundary layer problems. Teno [Tel] and Sonju [Sonl] were the first to use the

integral method. They were especially interested in boundary layer separation since this limited the performance of their supersonic open cycle MHD generator. They used the von Kármán momentum integral equation and an empirical aerodynamical correlation equation for one of the boundary layer shape factors. This implies that MHD terms are present only in the core flow equations but not in the boundary layer equations. Massee [Ma1] applied the same set of equations to conditions of a closed cycle MHD generator and showed that the disadvantage of these equations is an unrealistic behaviour of the displacement thickness at increasing MHD interaction. Gertz et al. [Ge1] extended the work of Teno and Sonju by deriving a set of integral boundary layer equations which includes the necessary MHD terms. Results of the calculations are verified by means of numerical results of the STAN-5 two-dimensional computer code [Cr1]. Gertz's method is used in designing the linear open cycle AVCO channels. Nakamura [Na1] applied the equations of Gertz to describe the boundary layers in an open cycle disk generator. Massee [Ma2] extended the approach of Gertz to the conditions of closed cycle MHD generators. This is also the subject of the present work. The numerical results of this approach will be compared in this thesis with experimental results obtained in the blow-down facility at the Eindhoven University of Technology.

Experimental work

Here the attention will be focussed completely on gaseous MHD flows. Results from open cycle MHD experiments will only be mentioned when they are important for the present study. The earliest experimental paper on MHD boundary layers is that of Olin [O11] who studied the fully developed turbulent flow in an electrically insulated duct in the plane perpendicular to the transverse magnetic field. He studied velocity profiles, skin friction and the suppression of turbulence due to MHD effects. Olin measured the velocity profiles by means of a water-cooled pitot probe under simulated open cycle MHD conditions. Due to suppression of the turbulence the velocity profiles have a more laminar character but otherwise they are similar to non-MHD profiles.

Brederlow et al. [Br1] measured velocity and temperature profiles in the electrode wall boundary layer of an MHD generator working with potassium seeded argon plasma. They used a pitot probe to measure velocity and a thermocouple probe together with a line-reversal method to determine gastemperature. The results were used to study the effect of boundary layers on open circuit voltage. Brown [Bro1] determined the electron density and electron temperature under non-MHD conditions in an argon plasma seeded with NaK at atmospheric pressure and a stagnation temperature of 2000 K. He measured profiles in the boundary layer over a cooled flat plate by means of an electrical conductivity probe and a spectroscopic technique. Tseng and Talbot [Ts1] and Merck [Me1] also used probes to measure boundary layer profiles in noble gas flows. Merck studied the boundary layer at the insulator wall of an MHD generator and found good agreement between his theory and the measured velocity and temperature profiles. He concluded that the heat and friction losses are determined by the turbulent character of the flow, and that the ratio of Reynolds and Hartmann number determines whether the flow is turbulent or not. Daily [Da1] measured velocity, temperature and electron density profiles in an open cycle MHD generator under both subsonic and supersonic conditions. The temperature and the electron density were measured spectroscopically and for the velocity a laser Doppler method was used. The electrode wall boundary layer was studied but no overshoot in the temperature profile was detected. Since the current density was only 0.005 A/cm^2 in the subsonic case this can be explained by very small MHD interaction. In the supersonic case the current density was about 0.5 A/cm^2 but Daily mentions that here the results were influenced by secondary cross flow patterns. Rankin [Ra1] measured only the velocity profile by means of a laser Doppler method in the insulator wall boundary layer of an open cycle MHD generator. He found a distinct overshoot in the velocity profile under subsonic MHD conditions and obtained good agreement between his measurements and numerical results from the STAN-5 computer code [Cr1]. The numerical results show moreover that the magnitude of the velocity overshoot depends on the ratio of wall to core static temperature. James [Ja1] measured

temperature profiles by spectroscopic means in the electrode wall boundary layer of an open cycle MHD generator. He was especially interested in Joule heating effects on the temperature profile, voltage drop and heat transfer. In order to determine the latter he measured the change in the wall temperature. He found a distinct influence of Joule heating on the heat transfer but did not measure an overshoot in the temperature profile. Just as in the experiments of Daily his results were probably influenced by secondary cross flow patterns. McClaine [Mc1] derived a Mach number distribution from measurements with a stagnation pressure probe 0.7 meter downstream of the exit of a subsonic MHD generator. The static pressure is measured at the same location and for the calculation of the Mach number a constant ratio of specific heats is assumed. The measurements were performed with strong MHD interaction, open cycle conditions. Distinct overshoots in the Mach number distribution are found in the plane between the insulator walls. In the plane between the electrode walls the Mach number distribution is very asymmetrical. McClaine expects that this results from a region of separated flow which may have been triggered by the probe. Anyhow this seems a confirmation of the fact that the electrode wall boundary layer is in general closer to separation than the insulator wall boundary layer.

1.3 Scope of the present work

It is the purpose of the present study to develop a fast computer code which can be used for designing closed cycle MHD generators. Since the boundary layer behaviour can influence the gasdynamics under conditions of strong MHD interaction a core flow and boundary layer description using the integral approach is required. In this approach specific MHD problems arise such as the choice of suitable velocity and temperature profiles, the selection of useful expressions for the gasdynamic transport coefficients and the determination of the voltage drop and the current density displacement thickness. The numerical results of the theoretical model are compared with experimental results obtained in the blow-down facility at the Eindhoven University of Technology.

2 Theoretical description of turbulent boundary layer development

2.1 Formulation of the problem

Since boundary layer separation can limit the enthalpy extraction of strong interaction MHD generators a single quasi-one-dimensional flow model is insufficient for designing these devices. This is evident since in these models the influence of boundary layers is not explicitly taken into account but is averaged over the circumference of the cross-section of the generator. In order to obtain a more realistic estimate of the performance of an MHD channel, the flow will be described by a coupled core flow and boundary layer model as shown schematically in figure 3.

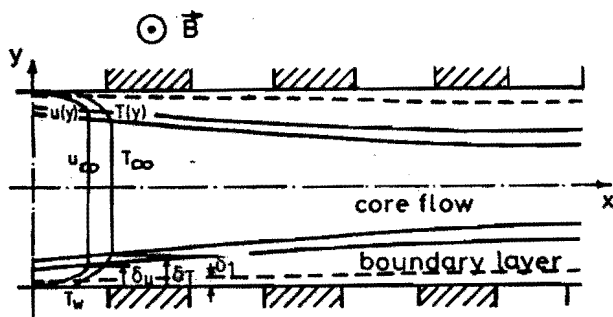


Fig. 3 Coupled core flow and boundary layer model.

δ_u = thickness of the velocity boundary layer

δ_T = thickness of the temperature boundary layer

δ_j = displacement thickness.

The flow in the core can be assumed to depend on x only so that the quasi-one-dimensional MHD flow equations can be used to calculate its development. In this thesis the growth of the boundary layers along the walls is calculated by means of the integral approach. The integral boundary layer equations are solved simultaneously with the core flow equations with the necessary coupling provided by the displacement thickness correction on the effective core

area. The core flow and boundary layer model can also be used when the boundary layer equations are solved by means of a finite difference formulation as for instance in the work of Arts and Merck [Art1]. With this approach, however, a large computer core storage is needed and computer run times are long. This implies that this method is not very suitable as a preliminary design tool, where the effects of variation of a large number of parameters must be investigated. The advantage of using the boundary layer equations in the integral form is that the problem is reduced to the solution of ordinary (rather than partial) differential equations. This implies an important reduction in required core storage and run time of the computer. The integral approach has the disadvantage of requiring assumptions of velocity and temperature profiles and of suitable expressions for the transport coefficients as an input into the program. Another disadvantage of the integral approach is that details of phenomena near the edges of electrodes can not be described and that the appearance of streamers can only be treated in an average sense. This may also be considered an advantage, however, since the mentioned phenomena are so complicated that a satisfactory description in the finite difference approach has not yet been found.

The boundary layer phenomena in MHD generators are distinctly different from those in gasdynamic turbulent duct flows due to the difference in boundary layer behaviour on electrode walls and insulator walls. The general boundary layer characteristics on the insulator walls are depicted schematically in figure 4. Consistent with one of the Maxwell equations the electric field E_y is constant through the insulator wall boundary layer and is therefore independent of z . The induced electric field $(\vec{u} \times \vec{B})_y$, however, will be nonuniform in the z -direction as a result of the velocity profile in the boundary layer on the insulator wall. In the core of an MHD generator $E_{y\infty}$ is smaller than $u_\infty B_z$ in order to be able to generate electric power. The local current density j_y is proportional to $(uB_z - E_y)$ so figure 4 shows that j_y will be smaller in the boundary layer than in the bulk and will even change sign close to the wall. This reversal of current density causes a

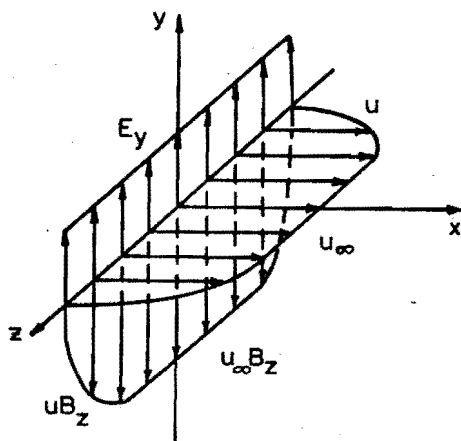


Fig. 4 Electrical characteristics of the insulator wall boundary layer.

direct reduction of the electrical power output of the generator integrated over the channel width. This is taken into account by introducing a current density displacement thickness $\delta_{j,i}$ such that $(b-2\delta_{j,i})$ is the effective width of the channel which is available for power production. Another consequence of the fact that j_y is smaller in the insulator wall boundary layer than in the core implies that the boundary layer is less retarded due to the Lorentz force $j_y B_z$ than the core. This can lead to an overshoot in the velocity profile of the insulator wall boundary layer which is a marked difference with the velocity profile in gasdynamic turbulent duct flow.

In this discussion and in the calculations in this thesis the effect of the corners is neglected. Lengyel [Le1] has performed two-dimensional calculations in the cross-sectional plane of an MHD generator. His results show that the effects of the corners may lead to a significant increase in the current density displacement thickness.

The general boundary layer characteristics on the electrode walls and the associated losses are shown schematically in figure 5. Simple considerations of current continuity ($\nabla \cdot \vec{J} = 0$), following from Maxwell's equations, require that the current density j_y is almost independent of the coordinate y . Thus the current density displacement thickness is zero at the electrode wall. As shown in figure 5 the electric field E_y in the electrode wall boundary layer is, however, distinctly different from the value in the core. This is more related to the temperature profile than to the velocity profile, since the first implies lower values of temperature and therefore of electrical conductivity σ in the electrode wall boundary layer. This implies that the internal resistance in the boundary layer is larger than in the core or in other words that the electrical influence of the boundary layer can be represented by an additional series resistance R_{BL} . This series resistance can not be measured directly but if the voltage profile is measured by means of potential probes in the insulator wall its influence is discovered as the voltage drop ΔV . As indicated in figure 5 the voltage drop is not only the result of R_{BL} but also of a second series resistance R_S . This resistance R_S has no connection with the flow boundary layer but is related to an electrostatic boundary layer or sheath. The thickness of this sheath equals the Debye length λ_D which is much smaller than the flow boundary layer thickness (not drawn on scale in figure 5). In this sheath the plasma can no longer be considered as quasi-neutral and here the electric fields connected with field emission and arcing phenomena will be present. In section 2.9 a theoretical calculation of R_{BL} will be presented but no model will be set up in this thesis for determining R_S . The consequence for the boundary layer of the presence of the resistances R_{BL} and R_S is that the Joule dissipation in the electrode wall boundary layer will be larger than in the core. This can lead to an overshoot in the temperature profile which makes the electrode wall boundary layer also distinctly different from boundary layers in gasdynamic turbulent duct flows. Since the Lorentz force in the electrode wall boundary layer equals the value in the core it is clear that boundary layer separation will start at the electrode wall and not at the

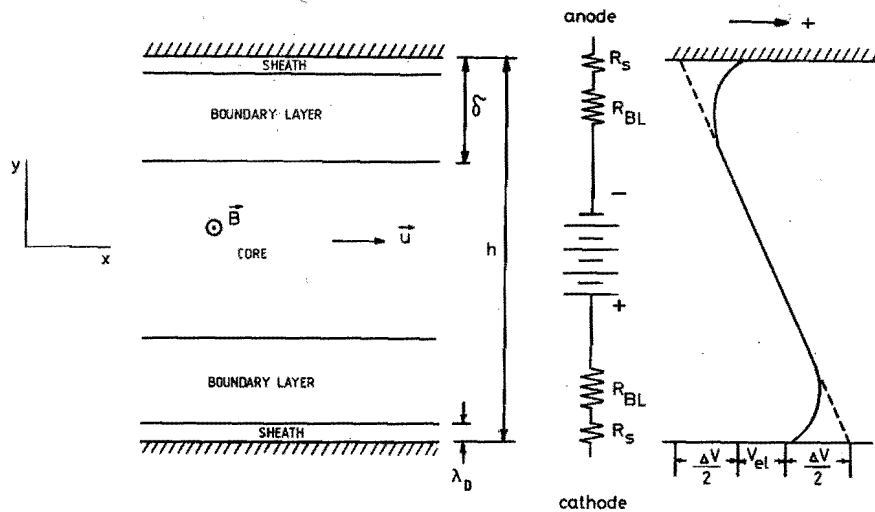


Fig. 5 Electrical characteristics of the electrode wall boundary layer.

Note: it is not suggested here that R_{BL} and R_s are necessarily constant nor that they are purely resistive.

insulator wall. The appearance of boundary layer separation is directly related to the amount of generated electric power and sets an upper limit to the enthalpy extraction especially in high interaction supersonic MHD generators [Tel; see also chapter 3].

2.2 The basic equations of MHD flows

2.2.1 The general form using the MHD approximation

The working medium in a closed cycle MHD generator consists of a noble gas with a small addition of seed material. In the present work the plasma consists of argon seeded with cesium. The plasma has a stagnation temperature of 2000 K and a stagnation pressure of several bars. Under these conditions the plasma consists of electrons, singly ionized argon and cesium ions, and argon and cesium atoms.

The properties of the plasma are determined by the distribution functions of each of the species. These functions can be obtained by solving the Boltzmann equation for each of the species. From the solutions the continuity, momentum and energy equations may be derived, which have to be supplemented by the Maxwell equations to describe the electromagnetic fields. An extensive treatment of the procedure is presented in Sutton and Sherman [Sul]. For the specific case of a plasma flowing through an MHD generator channel a number of simplifying assumptions can be made.

- a. Given the strong collisional interaction between the ions and atoms at the pressure considered, the temperature and flow velocity can both be assumed to be equal for all the heavy species. This assumption results in one momentum and one energy equation for the heavy particles.
- b. The magnetic Reynolds number is small in MHD generator plasmas, i.e. the magnetic induction associated with the current density in the plasma is negligible compared to the applied magnetic induction.

c. The space charge density is assumed to be small

$$\frac{|n_e - n_i|}{n_e} \ll 1 \quad (2.1)$$

This means that the minimum characteristic length in the plasma to be described is the Debye length. Using equation (2.1), n_e can be substituted for $n_i + n_i C$ in the conservation equations. Then these equations do not give any information about the space charge density and the Poisson equation can be used to check the validity of equation (2.1) after a solution has been found.

d. If the problems studied are restricted to phenomena at frequencies that are low compared to the plasma frequency, and with the previous assumptions of small magnetic Reynolds number and small space charge density, the Maxwell equations are reduced to

$$\nabla \cdot \vec{j} = 0 \quad (2.2)$$

$$\nabla \times \vec{E} = 0 \quad (2.3)$$

Equation (2.2) can also be obtained from the continuity equations for ions and electrons, which means that equation (2.2) does not provide any new information. The only Maxwell equation which has to be given is (2.3). The assumptions c. and d. form the usual MHD approximation.

The set of equations that describes the plasma is presented in table I. In this set the mass of an electron is neglected with respect to the mass of a heavy particle. The mass of an argon atom is assumed to be equal to that of its ion, and the same applies to cesium. In the temperature and pressure range chosen the minimum electron density will be 10^{19} m^{-3} and the minimum electron temperature will be equal to the heavy particle temperature. Under these conditions the dominant ionization process takes place by electron-atom collisions, while the recombination process is governed by three-body collisions. The collisional-radiative

CONTINUITY EQUATIONS

ELECTRONS : $\frac{\partial}{\partial t} n_e + \nabla \cdot (n_e \vec{u}_e) = n_e n_{aA} k_{fA} + n_e n_{aC} k_{fC} - n_e^2 n_{iA} k_{rA} - n_e^2 n_{iC} k_{rC}$

ARGON IONS : $\frac{\partial}{\partial t} n_{iA} + \nabla \cdot (n_{iA} \vec{u}) = n_e n_{aA} k_{fA} - n_e^2 n_{iA} k_{rA}$

CESIUM IONS : $\frac{\partial}{\partial t} n_{iC} + \nabla \cdot (n_{iC} \vec{u}) = n_e n_{aC} k_{fC} - n_e^2 n_{iC} k_{rC}$

ARGON ATOMS : $\frac{\partial}{\partial t} n_{aA} + \nabla \cdot (n_{aA} \vec{u}) = -n_e n_{aA} k_{fA} + n_e^2 n_{iA} k_{rA}$

CESIUM ATOMS : $\frac{\partial}{\partial t} n_{aC} + \nabla \cdot (n_{aC} \vec{u}) = -n_e n_{aC} k_{fC} + n_e^2 n_{iC} k_{rC}$

MOMENTUM EQUATIONS

ELECTRONS : $0 = -\nabla(n_e kT_e) - n_e e(\vec{E} + \vec{u}_e \times \vec{B}) + n_e m_e (\vec{u} - \vec{u}_e) \sum_{j=1}^4 v_j$

HEAVY SPECIES : $\frac{\partial}{\partial t} (n_A m_A + n_C m_C) \vec{u} + \nabla \cdot [(n_A m_A + n_C m_C) \vec{u} \vec{u}] = -\nabla(nkT) + (n_{iA} + n_{iC}) e(\vec{E} + \vec{u} \times \vec{B}) - n_e m_e (\vec{u} - \vec{u}_e) \sum_{j=1}^4 v_j + \nabla \cdot \tau_{\alpha\beta}$

ENERGY EQUATIONS

ELECTRONS : $\frac{\partial}{\partial t} \left[\frac{3}{2} n_e kT_e + n_{iA} E_{iA} + n_{iC} E_{iC} \right] + \nabla \cdot \left[\left(\frac{3}{2} n_e kT_e + n_{iA} E_{iA} + n_{iC} E_{iC} \right) \vec{u}_e \right] = -\vec{u}_e \cdot \nabla(n_e kT_e) - (n_e kT_e) \nabla \cdot \vec{u}_e - n_e e \vec{E} \cdot \vec{u}_e + n_e m_e \vec{u} \cdot (\vec{u} - \vec{u}_e) \sum_{j=1}^4 v_j$
 $- \frac{3}{2} \delta n_e m_e k(T_e - T) \sum_{j=1}^4 \frac{v_j}{m_j} - \dot{R} - \nabla \cdot \vec{q}_e$

HEAVY SPECIES : $\frac{\partial}{\partial t} \left[\frac{3}{2} nkT + \frac{1}{2} (n_A m_A + n_C m_C) u^2 \right] + \nabla \cdot \left[\left(\frac{3}{2} nkT + \frac{1}{2} (n_A m_A + n_C m_C) u^2 \right) \vec{u} \right] = -\vec{u} \cdot \nabla(nkT) - (nkT) \nabla \cdot \vec{u} + (n_{iA} + n_{iC}) e \vec{E} \cdot \vec{u} - n_e m_e \vec{u} \cdot (\vec{u} - \vec{u}_e) \sum_{j=1}^4 v_j$
 $+ \frac{3}{2} \delta n_e m_e k(T_e - T) \sum_{j=1}^4 \frac{v_j}{m_j} - \nabla \cdot \vec{q} - \frac{\partial}{\partial x_\alpha} (\tau_{\alpha\beta} u_\beta)$

MAXWELL'S EQUATIONS

$\nabla \times \vec{E} = 0$

where j = 1,2,3 and 4 denotes argon atoms, argon ions, cesium atoms and cesium ions respectively

Table 1 Basic equations of two-temperature plasmas.

recombination coefficients, which also take into account the influence of two-body recombinations, are used [Bal]. The values for k_{rA} and k_{rC} have been taken from [Hof1] and [Tal] respectively

$$k_{rA} = 1.29 \cdot 10^{-44} (11.5 \frac{e}{kT_e} + 2) \exp(4.25 \frac{e}{kT_e}) \quad (2.4)$$

$$k_{rC} = 2.58 \cdot 10^{-39} \exp(1.337 \frac{e}{kT_e}) \quad (2.5)$$

Expressions of this type have already been given by von Engel and Steenbeck [En1].

When the recombination rate coefficients are given, the ionization rate coefficients follow from the Saha equations, because if the number of ionizations is equal to that of recombinations, the continuity equations change into

$$\frac{n_e n_{iC}}{n_{aC}} = \frac{k_{fC}}{k_{rC}} = 2.42 \cdot 10^{21} T_e^{3/2} \exp(-\frac{3.893e}{kT_e}) \quad (2.6)$$

$$\frac{n_e n_{iA}}{n_{aA}} = \frac{k_{fA}}{k_{rA}} = 2.42 \cdot 10^{22} T_e^{3/2} \exp(-\frac{15.75e}{kT_e}) \quad (2.7)$$

Since the processes of ionization and recombination are assumed to take place as a result of the interaction with electrons only, they will be determined by the temperature of the electrons. In cases where the electron temperature differs from the heavy particle temperature the rate coefficients and the Saha equation have to be evaluated at the electron temperature, as indicated in equations (2.6) and (2.7).

The collision frequencies used in the momentum and energy equations are calculated from the elastic collision cross sections. Thus

$$\nu_j = n_j Q_j \sqrt{\frac{8kT_e}{\pi m_e}} \quad (2.8)$$

where j denotes aA , aC , iA , and iC for argon atoms, cesium atoms, argon ions and cesium ions respectively. Q_{eaC} is approximated by

the constant value $5 \cdot 10^{-18} \text{ m}^2$ [Bro2] whereas Q_{eaA} is approximated by [Mil]

$$Q_{eaA} = 2.79841 \cdot 10^{-21} \left(\frac{1.46 T_e}{1000} - 0.535 \right) \text{ m}^2 \quad (2.9)$$

Q_{eiA} and Q_{eiC} are obtained from Spitzer [Spl].

The collision frequencies are obtained by averaging over the velocity distribution function of the species. The momentum equation for the electrons provides a solution for the drift velocity; the inertia term in this equation can be neglected. A comparison of the inertia term with the collision term in the right-hand side of the equation defines another minimum characteristic length

$$\lambda_{in} = \frac{u_e}{\sum_j \nu_j} \quad (2.10)$$

For the plasma under consideration this length is always smaller than the Debye length, so the neglect of the inertia term is consistent with the previous approximation regarding the space charge density [Vee2]. In the electron energy equation the kinetic energy connected with the drift velocity $\frac{1}{2} m_e u_e^2$ is small with respect to the total energy $\frac{3}{2} k T_e + E_I$ and can be neglected. The total energy $\frac{3}{2} k T_e + E_I$ is defined with respect to the energy of a bound electron. The fractional energy loss factor δ in the energy loss term on the right-hand side of the energy equations is taken to be equal to 2, because in atomic gases the energy is transferred via elastic collisions.

In the left-hand side of the electron energy equation the change in energy of the electron cloud by ionizations and recombinations is included. The term \dot{R} in the electron energy equation denotes the radiation loss that the electron cloud experiences, which is mainly caused by resonant radiation from the cesium atom. The calculation of \dot{R} is quite complicated for the three-dimensional situation. An expression for \dot{R} in a one-dimensional approximation will be discussed in section 2.2.3.

The effects of the generator walls are felt through the viscous stress tensor $\tau_{\alpha\beta}$ and the heat flux vector \vec{q} in the heavy particle momentum and energy equation. It is customary to neglect viscous effects in the equations for the electron gas [Dol], but the electron heat flux vector \vec{q}_e will in general contribute to the electron energy balance. It has been shown by White [Whl] and Merck [Mel] that the set of equations in table I may also be used to describe turbulent flows. In that case densities, velocities and temperatures have to be interpreted as quantities, which have been averaged over the turbulent field. The effect of the turbulence is then taken into account as additional contributions to the parameters $\tau_{\alpha\beta}$ and \vec{q} . Following White [Whl] these quantities can be written as

$$\tau_{\alpha\beta} = \mu \left(\frac{\partial u_\alpha}{\partial x_\beta} + \frac{\partial u_\beta}{\partial x_\alpha} \right) - \overline{\rho' u'_\alpha u'_\beta} = \mu_t \left(\frac{\partial u_\alpha}{\partial x_\beta} + \frac{\partial u_\beta}{\partial x_\alpha} \right) \quad (2.11)$$

$$q_\alpha = -\kappa \frac{\partial T}{\partial x_\alpha} + \overline{\rho' u'_\alpha h'} = -\kappa_t \frac{\partial T}{\partial x_\alpha} \quad (2.12)$$

In these expressions the prime indicates a turbulent quantity and the bar indicates a time average. As Doss [Dol] has pointed out the electron transport properties are negligibly affected by gasdynamic turbulence due to the high mobility of the electrons. Therefore there is no turbulent contribution to the heat flux vector of the electrons, which can be written as [Mesl]

$$q_{e,\alpha} = -\kappa_e \sum_\beta M_{\alpha\beta} \frac{\partial T_e}{\partial x_\beta} \quad (2.13)$$

Here $M_{\alpha\beta}$ is the Hall tensor which will be specified in section 2.2.3. With this the set of equations which can be used to describe the compressible, turbulent flow of two-temperature plasmas has been completed in its general form. In the next sections simplifications will be introduced in order to describe boundary layer and quasi-one-dimensional phenomena.

2.2.2 The global, quasi-one-dimensional equations

The global, three-dimensional equations for turbulent MHD flow can be obtained by adding the equations for the electron and for the heavy particle gas in the general form which were presented in section 2.2.1. In this process the terms describing the collisional interaction between the electrons and the heavy particle gas vanish. Taking into account that only the axial component of the momentum equation is needed to describe the boundary layers and the flow through a channel of slowly varying cross-section, the global equations are

$$\frac{\partial}{\partial x} (\rho u) + \frac{\partial}{\partial y} (\rho v) + \frac{\partial}{\partial z} (\rho w) = 0 \quad (2.14)$$

$$\rho u \frac{\partial u}{\partial x} + \rho v \frac{\partial u}{\partial y} + \rho w \frac{\partial u}{\partial z} = - \frac{\partial p}{\partial x} + j_y B_z + \frac{\partial}{\partial y} (\mu_t \frac{\partial u}{\partial y}) + \frac{\partial}{\partial z} (\mu_t \frac{\partial u}{\partial z}) \quad (2.15)$$

$$\begin{aligned} \rho u \frac{\partial H}{\partial x} + \rho v \frac{\partial H}{\partial y} + \rho w \frac{\partial H}{\partial z} = \vec{j} \cdot \vec{E} + \frac{\partial}{\partial y} (\kappa_t \frac{\partial T}{\partial y}) + \frac{\partial}{\partial z} (\kappa_t \frac{\partial T}{\partial z}) \\ + \frac{\partial}{\partial y} (\mu_t u \frac{\partial u}{\partial y}) + \frac{\partial}{\partial z} (\mu_t u \frac{\partial u}{\partial z}) \end{aligned} \quad (2.16)$$

The set of equations has been written such that it can be applied both to the electrode wall and to the insulator wall. The right-hand side of the equations has been simplified by assuming that u is the largest velocity component and that the largest components of the gradients of u and T are in the direction perpendicular to the walls. The resulting set of global equations is very similar to that presented by Doss [Do1] and Merck [Me1]. In writing down the set of equations, stationary conditions have been assumed and the following definitions have been used

$$\rho = \sum_j n_j m_j = n_a m_A + n_c m_C \quad (2.17)$$

$$H = \frac{5}{2} RT + \frac{u^2}{2} = C_p T + \frac{u^2}{2} \quad (2.18)$$

$$p = \sum_j n_j k T_j \approx (n_A + n_C) k T = nkT \quad (2.19)$$

$$\vec{j} = en_e (\vec{u} - \vec{u}_e) \quad (2.20)$$

In writing down these equations the contribution of the electrons to ρ , p and ρH is neglected because $n_e \ll n$ and $m_e \ll m_A, m_C$. Since the heat conduction coefficient is in first approximation proportional to the density, \vec{q}_e has been neglected with respect to \vec{q} in equation (2.16). An estimate of the magnitude of the radiation loss \dot{R} shows that its contribution in equation (2.16) can be neglected under closed cycle MHD conditions. Finally turbulent viscosity and heat conduction coefficients have been introduced in equations (2.15) and (2.16) which also take into account the turbulent contributions specified in section 2.2.1.

The quasi-one-dimensional equations can be easily derived from the equations (2.14) to (2.16) by assuming that the cross-section of the channel varies so slowly that the velocity components v and w and the derivatives in the y and z direction can be neglected. The effects of friction and heat conduction are only felt near the walls and are smeared out over the circumference of the cross-section. After averaging over the cross-section the equations can then be written as

$$\frac{d}{dx} (\rho u A) = 0 \quad (2.21)$$

$$\rho u \frac{du}{dx} = - \frac{dp}{dx} + j_y B_z + \tau_{xy,w} \frac{C}{A} \quad (2.22)$$

$$\rho u \frac{dH}{dx} = \vec{j} \cdot \vec{E} - q_{y,w} \frac{C}{A} \quad (2.23)$$

A comparison with equation (2.16) shows that a term $(u \tau_{xy,w}) C/A$ would have been expected in the right-hand side of equation (2.23). This term vanishes, however, due to the boundary condition that $u=0$ at the wall. In the quasi-one-dimensional approximation the effects of the walls are not considered in detail. Therefore $\tau_{xy,w}$ and $q_{y,w}$ can not be determined from du/dy and dT/dy . Instead empirical correlations found in the literature are used, which will be discussed in section 2.8. It will be clear that the equations (2.21) to (2.23) can only be used to describe the phenomena in an MHD generator, as long as the boundary layer development does not influence the distribution of the properties in the core flow.

Results of calculations with this set of equations will be presented in section 3.1.

2.2.3 The simplified equations for the electron gas

It will be clear that the equations for the electron gas in table I can be used to describe the boundary layers of n_e and T_e along the generator walls. The boundary layers of n_e and T_e do not influence in first approximation the gasdynamic behaviour, although there is an indirect effect since the n_e and T_e profiles determine the voltage drop. Moreover the definition of the boundary conditions on n_e and T_e is a complicated problem [Kol] which has not yet been solved for realistic conditions, since it would have to include streamers and arc spots. Therefore the equations of the electron gas will be simplified by assuming that the derivatives of n_e , T_e and \vec{u}_e can be neglected with respect to the algebraic terms. Under these conditions the continuity equations give a balance between the algebraic terms, resulting in the Saha equations for cesium ions and for argon ions, which have already been given in equations (2.6) and (2.7). The momentum equation for the electrons can be written in the form of a generalized Ohm's law by using (2.20) and the definitions

$$\sigma = \frac{e^2 n_e}{m_e \sum_j v_j} \quad (2.24)$$

$$\beta = \frac{eB}{m_e \sum_j v_j} \quad (2.25)$$

The generalized Ohm's law can then be written in vector form as

$$\vec{j} = \sigma(\vec{E} + \vec{u} \times \vec{B}) - \frac{\beta}{B} (\vec{j} \times \vec{B}) \quad (2.26)$$

and may also be written in an equivalent form by using the Hall tensor as

$$j_\alpha = \sigma \sum_\beta M_{\alpha\beta} (\vec{E} + \vec{u} \times \vec{B})_\beta \quad (2.27)$$

The Hall tensor can be written in matrix form as

$$\left[M_{\alpha\beta} \right] = \frac{1}{1 + \beta^2} \begin{bmatrix} 1 & -\beta & 0 \\ \beta & 1 & 0 \\ 0 & 0 & 1 + \beta^2 \end{bmatrix} \quad (2.28)$$

This matrix form shows clearly how the influence of the applied magnetic field makes the transport properties of the electron gas anisotropic. The same Hall tensor appears in the expression for the heat flux vector of the electrons, as shown in equation (2.13). The electron energy balance follows directly from the electron energy equation in table I by using the definitions in equations (2.20) and (2.24)

$$\frac{|\vec{j}|^2}{\sigma} - 3kn_e m_e (T_e - T) \sum_j \frac{v_j}{m_j} - \dot{R} = 0 \quad (2.29)$$

In this equation the first term indicates the energy gained by the electrons due to the internal Joule dissipation. The second term describes the energy lost in elastic collisions of electrons and heavy particles. The radiation loss \dot{R} can be calculated for a one-dimensional geometry of a plasma slab with thickness d_s . Following Takeshita and Grossmann [Tal], who take into account the transition of 134 cesium lines, \dot{R} can be expressed as

$$\dot{R} = \frac{n_a C}{\sqrt{d_s}} \left\{ 3.06_{10}^{-14} \exp\left(\frac{-1.64_{10}^4}{T_e}\right) + 9.32_{10}^{-12} \exp\left(\frac{-3.79_{10}^4}{T_e}\right) \right\} \quad (2.30)$$

With this the equations necessary to describe the ideal behaviour of the electron gas have been completed. However, some additional loss mechanisms have to be introduced in order to describe the behaviour in a realistic sense.

Relaxation length

Since the equations in this section have been reduced to algebraic

form, they would describe that n_e , T_e and \vec{j} instantaneously reach their final value as soon as the medium enters the magnetic field. It will appear from the experimental results in section 4.2 that this is not a realistic description of the actual phenomena. A certain relaxation length is needed over which the electron gas grows gradually to its final non-equilibrium state. Blom [B11] has shown that this process cannot be described correctly in a quasi-one-dimensional approximation, but that at least a two-dimensional solution has to be obtained.

Moreover it has been understood lately that the relaxation phenomenon is closely connected with the formation of streamers. This process has been studied extensively by Flinsenberg [F11] and a first theoretical model to describe the experimental results has been developed. Since this is not the primary goal of the present work, the relaxation length will be derived from the measurements in section 5.2.

Ionization instabilities

When the Hall parameter β exceeds a certain critical value, the electron gas becomes unstable, which means that fluctuations in the local values of the electron density and temperature, and consequently also the conductivity σ , appear in both time and space [Sol, Mes1]. Since this phenomenon is essentially connected with the two-temperature plasma situation in a closed cycle MHD generator, in which the electron gas is to a large extent decoupled from the heavy particles, the electron gas fluctuations are not directly coupled to gasdynamic turbulence. The result of the electron gas fluctuations is that the overall value of the conductivity, which can be measured at the outside of the plasma, is less than the local microscopic value obtained from equation (2.24). The critical value of the Hall parameter for an argon-caesium plasma can be approximated according to the quasi-linear theory [Sol] by a constant value of 1.5. Above this value the effective value of the Hall parameter equals roughly the critical value [Sol]

$$\beta_{\text{eff}} = \beta_{\text{crit}} \quad (2.31)$$

and the effective value of the conductivity decreases according to the relation

$$\sigma_{\text{eff}} = \sigma \frac{\beta_{\text{crit}}}{\beta} \quad (2.32)$$

To take into account the effect of ionization instabilities, the values of σ and β are replaced by the effective values in Ohm's law and in the electron energy balance. It will appear in section 5.1, however, that the calculated currents per generator segment are consistently larger than the measured values, which is probably caused by the presence of streamers.

Voltage drop

When the distribution of electric potential is measured between an electrode pair by means of potential probes flush with the inside of the insulator wall a reversal of the slope is measured close to the electrodes. In other words, if a straight line would be drawn through the potential points measured in the central region, a larger potential difference between electrodes would result than is actually measured. This is taken into account by introducing the total voltage drop ΔV which is the sum of the voltage drops at the anode and at the cathode. Referring to figure 5 it is clear that the electric field E_y is now related to the potential drop over the external resistance by means of the expression

$$E_y h - \Delta V = I_{e1} R_L \quad (2.33)$$

The exact way in which the voltage drop is taken into account will be worked out further in section 5.1 where also the influence of boundary layers and streamers on the electrical behaviour will be described. A physical explanation of the appearance of the voltage drop is the fact that the temperature profile in the electrode wall boundary layer is coupled with a profile in conductivity σ . A simple model for the voltage drop will be presented in section

2.9. Since the effects of streamers and arc spots can not be taken into account in this model, however, it is preferred to perform the calculations with the measured value for the total voltage drop.

Segmentation losses

Houben [Ho2] has shown from a two-dimensional, stationary solution of the electron gas equations in table I, coupled with the Maxwell equations (2.2) and (2.3) that the current in the center of the channel flows at a certain angle, determined by the Hall parameter, with the direction $\vec{u} \times \vec{B}$. This implies that the current path is increased, so that another correction factor has to be applied to the effective conductivity [B11]. The solution found by Houben is distinctly different, however, from a situation where streamers are present, as can be seen from a comparison with the results of Hara [Ha1]. Hara obtained a two-dimensional, time-dependent solution of the electron gas equations. In his results current constrictions or streamers are seen, which move with the gas velocity and which are approximately parallel to the $\vec{u} \times \vec{B}$ direction in the center of the channel. Since the goal of the present work is to describe a realistic situation, where the presence of streamers should be taken into account at least in an average sense, the results of Hara lead to the conclusion that segmentation losses are not important under these conditions.

2.3 The core flow equations

It has been mentioned in section 2.2.2 that the quasi-one-dimensional description is not satisfactory when the boundary layers occupy a significant part of the channel cross-section. As long as the boundary layers can be clearly distinguished from the core flow, where the gradients in directions perpendicular to the walls can be neglected, the core flow and boundary layer description is adequate. In this approach the core flow is described in the quasi-one-dimensional approximation. Since the gradients in the transverse directions are negligible in the core, the viscous and heat transfer effects disappear from the equations (2.21) to (2.23). These equations will be written down in the form,

which is actually used in the calculations. The equations can be expressed in terms of two derivatives in the x-direction, which can be chosen more or less arbitrarily. For the calculations in this thesis u and p are chosen as the independent variables. In order to work out the derivative of the stagnation enthalpy H in equation (2.23), the definition (2.18) is used and equation (2.21) plus the ideal gas law (2.19), which can also be written as

$$p = \rho RT \quad (2.34)$$

In this way the derivative of the temperature T can be eliminated from the equations, and after some straightforward algebra the following expressions are obtained

$$\frac{du_\infty}{dx} = \frac{u_\infty}{1 - M_\infty^2} \left\{ \frac{\vec{E}_\infty \cdot \vec{j}_\infty}{\rho_\infty u_\infty C_p T_\infty} - \frac{j_{y_\infty} B_z}{p_\infty} - \frac{1}{A_{\text{eff}}} \frac{dA_{\text{eff}}}{dx} \right\} \quad (2.35)$$

$$\frac{dp_\infty}{dx} = j_{y_\infty} B_z - \rho_\infty u_\infty \frac{du_\infty}{dx} \quad (2.36)$$

The derivative of the cross section A_{eff} , which appears in equation (2.35), has to be calculated from the geometrical cross section, corrected for the presence of the boundary layers. This derivative of A_{eff} gives the coupling between the core flow and the boundary layers; it may be considered as a known quantity for the core flow and it will be discussed in section 2.5. Only the derivatives of u_∞ and p_∞ are required to describe the core flow, since all remaining quantities can be calculated from algebraic relations such as equations (2.18), (2.34) and the continuity equation (2.21), which can be integrated to

$$\dot{m} = \rho_\infty u_\infty A_{\text{eff}} = \text{constant} \quad (2.37)$$

Of course the components of the electric current density \vec{j} and the electric field \vec{E} , which appear in the equations (2.35) and (2.36) have to be calculated from the equations for the electron gas presented in section 2.2.3.

2.4 The integral boundary layer equations

In this section the integral equations for the turbulent MHD boundary layer are derived by integrating the global equations from the wall to the middle of the duct. This is performed here in the symmetry plane of the channel since this makes the derivation somewhat more elegant and compact. It can be shown that this does not restrict the validity of the resulting equations to the symmetry plane.

2.4.1 The momentum integral equation

The starting point for the derivation of the integral boundary layer equations is the set of three-dimensional global equations. The momentum integral equation is obtained from writing down equation (2.15) in the middle of the channel ($z=0$) and integrating over y from $-h/2$ to 0 , if the bottom electrode wall is considered. Since symmetry arguments show that the z -derivative and the velocity component w are zero in the plane $z=0$ equation (2.15) simplifies to

$$\rho u \frac{\partial u}{\partial x} + \rho v \frac{\partial u}{\partial y} = - \frac{\partial p}{\partial x} + j_y B_z + \frac{\partial \tau_{xy}}{\partial y} \quad (2.38)$$

Since p is assumed to be constant over the cross section, which is a reasonable assumption for a segmented Faraday generator if there are no oblique shocks and if the boundary layers are not too thick, $\frac{\partial p}{\partial x}$ can be eliminated by means of the core-momentum equation (2.36). In order to take into account the fact that the distance between the insulator walls is not constant, the continuity equation (2.14) is written in the form

$$\frac{\partial}{\partial x} (\rho u) + \frac{\partial}{\partial y} (\rho v) + \rho u D_e = 0 \quad (2.39)$$

where the parameter D_e is worked out later. From (2.39) it follows that

$$\rho v = - \int_{-h/2}^y \left\{ \frac{\partial}{\partial x} (\rho u) + \rho u D_e \right\} d\xi \quad (2.40)$$

Substituting this into equation (2.38) the result is

$$\rho u \frac{\partial u}{\partial x} - \frac{\partial u}{\partial y} \int_{-h/2}^y \left\{ \frac{\partial}{\partial x} (\rho u) + \rho u D_e \right\} d\xi = \rho_\infty u_\infty \frac{du_\infty}{dx} + (j_y - j_{y_\infty}) B_z + \frac{\partial \tau_{xy}}{\partial y} \quad (2.41)$$

Now performing the integration over y from $-h/2$ to 0 , the second term in the left-hand side can be integrated by parts, which gives the relation

$$\begin{aligned} & -h/2 \int \left\{ \rho u \frac{\partial u}{\partial x} - (u_\infty - u) \left[\frac{\partial}{\partial x} (\rho u) + \rho u D_e \right] \right\} dy = \\ & -h/2 \int \left\{ \rho_\infty u_\infty \frac{du_\infty}{dx} + (j_y - j_{y_\infty}) B_z + \frac{\partial \tau_{xy}}{\partial y} \right\} dy \end{aligned} \quad (2.42)$$

Rearranging the terms and integrating the last term in the right-hand side, the result is obtained

$$\begin{aligned} & \rho_\infty u_\infty^2 \frac{d}{dx} \left[\int_{-h/2}^0 \left(1 - \frac{u}{u_\infty} \right) dy \right] + \left[\frac{d}{dx} (\rho_\infty u_\infty^2) + \rho_\infty u_\infty^2 D_e \right] \int_{-h/2}^0 \frac{\rho u}{\rho_\infty u_\infty} \left(1 - \frac{u}{u_\infty} \right) dy \\ & + \rho_\infty u_\infty \frac{du_\infty}{dx} \int_{-h/2}^0 \left(1 - \frac{\rho u}{\rho_\infty u_\infty} \right) dy = j_{y_\infty} B_z \int_{-h/2}^0 \left(1 - \frac{j_y}{j_{y_\infty}} \right) dy + \tau_{xy,w} \end{aligned} \quad (2.43)$$

Introducing the following definitions

$$\begin{aligned} \delta_{1,e} &= \int_{-h/2}^0 \left(1 - \frac{\rho u}{\rho_\infty u_\infty} \right) dy \quad ; \quad \delta_{2,e} = \int_{-h/2}^0 \frac{\rho u}{\rho_\infty u_\infty} \left(1 - \frac{u}{u_\infty} \right) dy \\ \delta_{j,e} &= \int_{-h/2}^0 \left(1 - \frac{j_y}{j_{y_\infty}} \right) dy \quad ; \quad C_f = \frac{\tau_{xy,w}}{\frac{1}{2} \rho_\infty u_\infty^2} \end{aligned} \quad (2.44)$$

equation (2.43) can be written as

$$\frac{d\delta_{2,q}}{dx} + \delta_{2,q} \left\{ \frac{d \ln \rho_\infty}{dx} + \frac{d \ln u_\infty}{dx} \left(2 + \frac{\delta_{1,q}}{\delta_{2,q}} \right) + D_q \right\} = \frac{C_f}{2} + \frac{j_{y_\infty} B_z}{\rho_\infty u_\infty^2} \delta_{j,q} \quad (2.45)$$

This is the momentum integral equation in a general form, which is

valid both for the electrode wall ($q=e$) and for the insulator wall ($q=i$). This equation can be found in simplified form in many articles and handbooks on boundary layers (e.g. [Sc1], [Wh1]).

Now returning to the parameter D_e , a comparison of equations (2.14) and (2.39) shows that D_e is defined as

$$D_e = \frac{1}{\rho u} \frac{\partial}{\partial z} (\rho W) \approx \frac{1}{u} \frac{\partial W}{\partial z} \quad (2.46)$$

D_e has to take into account the spreading of the boundary layer when the distance between the side-walls changes. Krause [Kr1] has shown that when the flow follows the divergence of the side-walls, then D_e equals the logarithmic derivative of the side-wall width. Hence

$$D_e = \frac{1}{b} \frac{db}{dx}, \quad D_i = \frac{1}{h} \frac{dh}{dx} \quad (2.47)$$

2.4.2 The kinetic energy integral equation

The starting point for the derivation of the kinetic energy integral equation is formula (2.38), which is multiplied by u before the integration over y from $-h/2$ to 0 is performed (for the bottom electrode wall). Again, just as in section 2.4.1, ρv in the second term in the left-hand side of the equation is eliminated by means of equation (2.40) and is worked out through integration by parts. The expression corresponding to equation (2.42) then takes the form

$$\begin{aligned} & -h/2 \int_0^0 \left\{ \rho u^2 \frac{\partial u}{\partial x} - \left(\frac{u_\infty^2 - u^2}{2} \right) \left[\frac{\partial}{\partial x} (\rho u) + \rho u D_e \right] \right\} dy = \\ & -h/2 \int_0^0 \left\{ \rho_\infty u_\infty \frac{du_\infty}{dx} + u(j_y - j_{y\infty}) B_z + u \frac{\partial \tau_{xy}}{\partial y} \right\} dy \end{aligned} \quad (2.48)$$

The last term in the right-hand side is also integrated by parts and some rearranging of the terms is necessary. Then introducing the definitions

$$\begin{aligned} \delta_{3,e} &= -h/2 \int_0^0 \frac{\rho u}{\rho_\infty u_\infty} \left(1 - \frac{u^2}{u_\infty^2}\right) dy ; \quad \delta_{4,e} = -h/2 \int_0^0 \frac{\rho u}{\rho_\infty u_\infty} \left(1 - \frac{\rho}{\rho_\infty}\right) dy \\ \delta_{ju,e} &= -h/2 \int_0^0 \frac{u}{u_\infty} \left(1 - \frac{jy}{jy_\infty}\right) dy ; \quad C_D = \frac{1}{\rho_\infty u_\infty^3} \int_{-h/2}^0 \tau_{xy} \frac{\partial u}{\partial y} dy \end{aligned} \quad (2.49)$$

equation (2.48) can be written as

$$\frac{d\delta_{3,q}}{dx} + \delta_{3,q} \left\{ \frac{d \ln \rho_\infty}{dx} + \frac{d \ln u_\infty}{dx} \left(3 - 2 \frac{\delta_{4,q}}{\delta_{3,q}}\right) + D_q \right\} = 2C_D + \frac{2j_{y_\infty} B_z}{\rho_\infty u_\infty^2} \delta_{ju,q} \quad (2.50)$$

This is again written in a general form, which is valid both for the electrode wall (q=e) and for the insulator wall (q=i). The dimensionless dissipation integral C_D denotes the energy per unit volume and time, which is transformed into heat by the turbulent shear stresses.

2.4.3 The stagnation-enthalpy integral equation

This integral equation is derived from formula (2.16), written down in the plane $z=0$, so that symmetry arguments show that it simplifies to the form

$$\rho u \frac{\partial H}{\partial x} + \rho v \frac{\partial H}{\partial y} = E_y j_y - \frac{\partial q_y}{\partial y} + \frac{\partial}{\partial y} (u \tau_{xy}) \quad (2.51)$$

Since a segmented Faraday generator is considered and since the segmentation losses are neglected in a situation, where the electric current is carried by streamers, the approximation $|E_x j_x| \ll |E_y j_y|$ has been used. The same approximation is used in writing down the corresponding core flow equation, which follows from equation (2.23). Since heat transfer vanishes in the core, this relation reduces to

$$\rho_\infty u_\infty \frac{dH_\infty}{dx} = E_{y_\infty} j_{y_\infty} \quad (2.52)$$

For the derivation of the integral equation, (2.52) is subtracted from (2.51) after which the integration over y from $-h/2$ to 0 is

performed (for the bottom electrode wall). Just like in section 2.4.1, ρv in the second term on the left-hand side of equation (2.51) is eliminated by means of equation (2.40) and is worked out through integration by parts. The expression corresponding to equation (2.42) then takes the form

$$\begin{aligned}
 & -h/2 \int_0^0 \left\{ \rho u \frac{\partial H}{\partial x} - (H_\infty - H) \left[\frac{\partial}{\partial x} (\rho u) + \rho u D_e \right] \right\} dy = \\
 & -h/2 \int_0^0 \left\{ \rho_\infty u_\infty \frac{dH_\infty}{dx} + (E_y j_y - E_{y\infty} j_{y\infty}) - \frac{\partial q_y}{\partial y} + \frac{\partial}{\partial y} (u \tau_{xy}) \right\} dy
 \end{aligned} \tag{2.53}$$

The last two terms in the right-hand side of this relation can be integrated directly, showing that the last term vanishes. After some rearranging, and introducing the definitions

$$\begin{aligned}
 \delta_{H,e} &= -h/2 \int_0^0 \frac{\rho u}{\rho_\infty u_\infty} \left(1 - \frac{H - H_w}{H_\infty - H_w} \right) dy ; \quad \delta_{Ej,e} = -h/2 \int_0^0 \left(1 - \frac{E_y j_y}{E_{y\infty} j_{y\infty}} \right) dy \\
 St &= \frac{q_w}{\rho_\infty u_\infty (H_\infty - H_w)}
 \end{aligned} \tag{2.54}$$

equation (2.53) can be written in the form

$$\begin{aligned}
 & \frac{d\delta_{H,q}}{dx} + \delta_{H,q} \left\{ \frac{d \ln \rho_\infty}{dx} + \frac{d \ln u_\infty}{dx} + \frac{H_\infty}{H_\infty - H_w} \frac{d \ln H_\infty}{dx} \left(1 + \frac{\delta_{1,q}}{\delta_{H,q}} \right) \right. \\
 & \left. - \frac{H_w}{H_\infty - H_w} \frac{d \ln H_w}{dx} + D_q \right\} = St + \frac{E_{y\infty} j_{y\infty}}{\rho_\infty u_\infty (H_\infty - H_w)} \delta_{Ej,q}
 \end{aligned} \tag{2.55}$$

This is again written in a general form, which is valid both for the electrode wall ($q=e$) and for the insulator wall ($q=i$).

2.4.4 The equations for a non-MHD boundary layer

For a simple case of a non-MHD turbulent boundary layer in a channel the velocity profile and the stagnation enthalpy profile are determined by two parameters N and δ (or δ') according to the relations

$$\frac{u}{u_\infty} = \xi^{1/N} ; \quad \frac{H - H_w}{H_\infty - H_w} = \frac{u}{u_\infty} \tag{2.56}$$

Here the compressibility transformation

$$dy' = \frac{\rho}{\rho_\infty} dy \quad ; \quad d\xi = \frac{dy'}{\delta'} \quad ; \quad \delta' = \int_0^\delta \frac{\rho}{\rho_\infty} dy \quad (2.57)$$

has been used and the parameter N changes due to the presence of a pressure gradient. Appendix A shows that the parameter N can be calculated if δ_2 and δ_3 are known so that a non-MHD turbulent boundary layer can be calculated by solving, simultaneously with the core flow equations (2.35) and (2.36), the differential equations for δ_2 (2.45) and for δ_3 (2.50). In the literature quite often an empirical equation is used instead of equation (2.50). As an example of such an equation the empirical equation of Garner [Gal] may be mentioned

$$\left(\frac{u_\infty \delta_2}{\nu_t}\right)^{1/6} \delta_2 \frac{d\bar{H}_{12}}{dx} = -e^{5(\bar{H}_{12} - 1.4)} \left\{ \left(\frac{u_\infty \delta_2}{\nu_t}\right)^{1/6} \frac{\delta_2}{u_\infty} \frac{du_\infty}{dx} + 0.0135(\bar{H}_{12} - 1.4) \right\} \quad (2.58)$$

Here the incompressible shapefactor \bar{H}_{12} is the ratio of the incompressible displacement thickness $\bar{\delta}_1$ and the incompressible momentum thickness $\bar{\delta}_2$. It can easily be shown from appendix A that

$$\bar{H}_{12} = 1 + \frac{2}{N} \quad (2.59)$$

so that the profiles are known once \bar{H}_{12} is determined. In papers by Teno [Tel] and Masee [Mal] equation (2.58) has also been used in describing the flow through an MHD generator, but in that case there are no MHD effects directly influencing the boundary layer. The results of a calculation with equation (2.58) will be discussed in section 3.2.

2.4.5 The equations for the MHD boundary layer along the insulator wall

For the insulator wall boundary layer one of the Maxwell equations namely (2.3) $\nabla \times \vec{E} = 0$ implies $E_y = E_{y_\infty}$. Since there is a profile of the

x component of the velocity, the field $E_y^* = uB - E_y$ that is the source of the electric current density, varies considerably when coming close to the wall and even reverses its sign. Thus j_y varies in similar fashion in the region close to the insulator wall. This implies that all MHD terms in the right-hand sides of the equations (2.45), (2.50) and (2.55) are important for the insulator wall boundary layer as can be seen from the definitions of $\delta_{j,i}$ and $\delta_{ju,i}$. From equation (2.54) and $E = E_{y\infty}$ it follows that

$$\delta_{Ej,i} = -b/2 \int_0^1 \left(1 - \frac{E_y j_y}{E_{y\infty} j_{y\infty}}\right) dz = \delta_{j,i} \quad (2.60)$$

$\delta_{j,i}$ and $\delta_{ju,i}$ must be determined from numerical integration. The approximation needed in this case will be discussed in section 2.9.

2.4.6 The equations for the MHD boundary layer along the electrode wall

For the electrode wall boundary layer the Maxwell equation (2.2) $\nabla \cdot \vec{j} = 0$ leads to $\delta j_y / \delta y = 0$ or $j_y = j_{y\infty}$, which is exact if the segmentation ratio is infinitely fine. For coarse segmentation and close to the edges of the electrodes two-dimensional effects are important and the relation is no longer true. However, even for coarse segmentation $j_y = j_{y\infty}$ is a reasonable approximation if an average of j_y is taken over a length scale comparable to the length of a segment (electrode + insulator). The equations (2.44) and (2.49) show that $\delta_{j,e}$ and $\delta_{ju,e}$ vanish since $j_y = j_{y\infty}$, so that there are no MHD terms in the differential equations for $\delta_{2,e}$ (2.45) and for $\delta_{3,e}$ (2.50). For $\delta_{Ej,e}$ defined in equation (2.54) the consequence of $j_y = j_{y\infty}$ is

$$\delta_{Ej,e} = -h/2 \int_0^1 \left(1 - \frac{E_y}{E_{y\infty}}\right) dy = \frac{\Delta V}{2E_{y\infty}} \quad (2.61)$$

where ΔV is the sum of the voltage drops across the cathode and the anode boundary layer. In the calculations in section 3.3 the measurements of ΔV have been approximated by a constant value (independent of x). It is also possible to determine the voltage

drop from a theoretical model, which is worked out in section 2.9.

2.5 The coupling of the core flow and the boundary layer

It has been mentioned in section 2.3 that the derivative of the cross section A_{eff} , which appears in the core flow equation (2.35), gives the coupling between the core flow and the boundary layer. The cross section A_{eff} is the geometrical cross section corrected for the boundary layer thicknesses. Since A_{eff} appears also in the integrated form of the continuity equation

$$\dot{m} = \rho_{\infty} u_{\infty} A_{\text{eff}} = \text{constant} \quad (2.37)$$

the displacement thicknesses have to be used in calculating A_{eff} . Thus

$$A_{\text{eff}} = (b - 2\delta_{1,i})(h - 2\delta_{1,e}) \quad (2.62)$$

Appendix A shows that for the simplest case of a non-MHD turbulent boundary layer with velocity and stagnation enthalpy profile according to equation (2.56), $\delta_1 (= \delta_{1,i} = \delta_{1,e})$ can be expressed as

$$\frac{\delta_1}{\delta^*} = \left\{ \frac{T_w}{T_{\infty}} + \frac{M_{\infty}^2}{3} \left(\frac{N}{N+2} \right) \right\} \left(\frac{1}{N+1} \right) \quad (2.63)$$

This expression shows that if the derivative of A_{eff} would be calculated from direct differentiation, it would result in derivatives of M_{∞} , T_{∞} and N . The derivatives of M_{∞} and T_{∞} can in principle be expressed in terms of derivatives of u_{∞} and p_{∞} . Appendix A shows that for the simplest case of a non-MHD turbulent boundary layer

$$N = \frac{3\delta_3 - 4\delta_2}{2\delta_2 - \delta_3} \quad (2.64)$$

so that the derivative of N can be expressed in terms of the derivatives of δ_2 and δ_3 . Due to the products in equation (2.63) this becomes already complicated even in the simplest case for which equations (2.63) and (2.64) are valid. Since the

complications for MHD boundary layers are much larger, an iterative approach of the coupling of core flow and boundary layer is preferred. Over an integration interval the derivatives of $\delta_{1,e}$ and $\delta_{1,i}$ are kept constant; the first estimate for each is the derivative from the previous integration interval. After integration a better estimate is found from the algebraic expressions for $\delta_{1,e}$ and $\delta_{1,i}$ discussed in appendix A and the integration is repeated. This yields a very simple iterative scheme that appears to give accurate results after a few iterations. Therefore the differential equations, which are actually integrated simultaneously for the general case of MHD boundary layers, include the derivatives of u_∞ (2.35), p (2.36), $\delta_{2,e}$ and $\delta_{2,i}$ (2.45), $\delta_{3,e}$ and $\delta_{3,i}$ (2.50) and $\delta_{H,e}$ and $\delta_{H,i}$ (2.55).

2.6 Velocity and enthalpy profiles in MHD and in non-MHD boundary layers; a review of the literature

In this section the choice of the velocity and enthalpy profiles used in the calculations for this thesis will be motivated. A review is presented of the profiles used in describing non-MHD boundary layers. It will be shown that MHD boundary layers differ in some characteristic ways from non-MHD boundary layers. This suggests that expressions for the profiles should be used, which allow for the special phenomena of MHD boundary layers.

2.6.1 The profile for non-MHD incompressible boundary layers

In this thesis only turbulent boundary layers are considered since this is the normal situation in MHD generators. In turbulent boundary layers three distinct layers have to be distinguished with different physical properties, which are caused by the different relative importance of the viscous and the turbulent shear stresses. In the inner layer closest to the wall the viscous shear dominates since the turbulent motions are damped when coming close to the wall. In the outer layer, which verges upon the core flow, the turbulent shear dominates since the velocity gradient has become small. In the overlap layer both types of shear are

important. The three layers can also be recognized in the expression for the velocity profile which is based upon the experimental work of Clauser [Cl1] and Coles [Co1] and which can be written as

$$\frac{u}{v^*} = \frac{1}{\kappa'} \ln \left(1 + \frac{yv^*}{v_t} \right) + B' + \frac{\tilde{\pi}}{\kappa'^2} [1 - \cos(\frac{\pi y}{\delta})] - \frac{1}{\kappa'} \ln \left(1 + 0.3 \frac{k^* v^*}{v_t} \right) - (3.39 \frac{yv^*}{v_t} + B') e^{-0.37 yv^*/v_t} \quad (2.65)$$

where $\kappa'=0.4$ and $B'=5.5$.

The first two terms in the right-hand side represent the overlap layer. The third term in the right-hand side represents the outer layer and is often called the law of the wake or the velocity defect law. The fourth term in the right-hand side is taken from the book by White [Wh1] and takes into account the effect of a rough wall with roughness height k^* . In equation (2.65) the definition

$$v^* = \sqrt{\frac{\tau_w}{\rho_w}} = u_\infty \sqrt{\frac{\rho_\infty C_f}{2\rho_w}} \quad (2.66)$$

has been used. There is some spreading in the values of the numerical constants for κ' and B' as quoted in different papers due to scatter in the experimental data. The constants in the last term in the right-hand side of equation (2.65) have been chosen by Kuhn and Nielsen [Ku1] such that if the limit of the expression is taken for very small values of yv^*/v_t , the so called law of the wall for the inner layer results in the form

$$\frac{u}{v^*} = \frac{yv^*}{v_t} \quad (2.67)$$

In order to obtain this limit the unit in the logarithmic term in equation (2.65) has also been added. $\tilde{\pi}$ is called the wake parameter and is directly related to the pressure gradient, which can be written in the dimensionless form

$$\beta' = \frac{\delta_1}{\tau_w} \frac{dp}{dx} \quad (2.68)$$

The parameter β' is called Clauser's equilibrium parameter because Clauser has shown that a boundary layer with variable pressure gradient but constant β' is in turbulent equilibrium in the sense that all the gross properties of that boundary layer can be scaled with a single parameter, which is related to δ_1 . White [Wh1] has shown that for boundary layers which are in equilibrium in the sense that $\beta' = \text{constant}$, there exists an empirical correlation of the form

$$\tilde{\pi} \approx 0.8(\beta' + 0.5)^{0.75} \quad (2.69)$$

The profile according to equation (2.65) is shown in figure 6 for different values of $\tilde{\pi}$; the three different layers are easily recognized in this figure. The profile in equation (2.65) has been thoroughly discussed during the famous Stanford Conference [Stal]. It has been widely accepted for describing incompressible turbulent boundary layer behaviour by means of the integral approach.

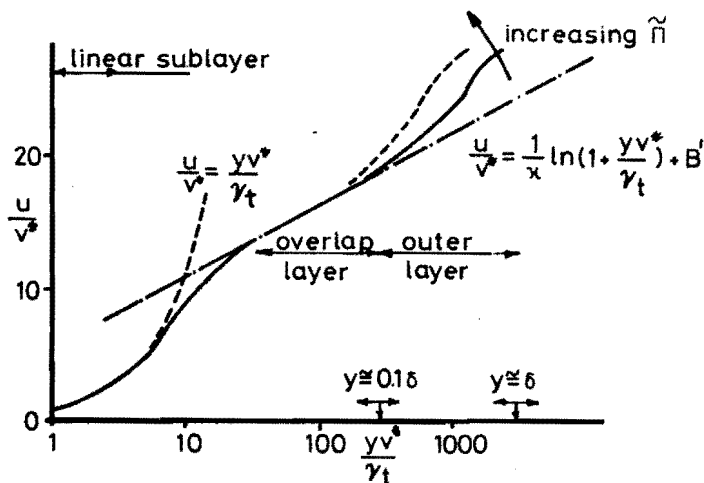


Fig. 6 Velocity profile of non-MHD incompressible boundary layer under adverse pressure gradient.

2.6.2 The profiles for non-MHD compressible boundary layers

First the generalization of the profile for non-MHD incompressible boundary layers due to van Driest [Dr1] will be discussed. Van Driest neglected the viscous inner layer, which is in general a good approximation, and modified Prandtl's mixing length theory [Pr1] to account for variable density. Prandtl's mixing length theory relates the turbulent shear stress τ_t to the velocity gradient by means of the relation

$$\tau_t = \rho \bar{l}^2 \left(\frac{du}{dy} \right)^2 \quad (2.70)$$

Here \bar{l} is the so called mixing length, which depends strongly upon the distance y from the wall. The relation between \bar{l} and y is different for the three layers mentioned in section 2.6.1. Von Kármán [Kal] showed that the relation between \bar{l} and y in the overlap layer is

$$\bar{l} = \kappa' y \quad \text{with} \quad \kappa' = 0.4 \quad (2.71)$$

To relate density to velocity van Driest adopted the Crocco-Busemann approximation [Cr1, Bu1]. This relation follows from the fact that the global momentum equation (2.15) and the global energy equation (2.16) can be written in a similar form for non-MHD flows. Expressing the heat flux in terms of stagnation enthalpy and introducing the turbulent Prandtl number defined by

$$\text{Pr}_t = \frac{\mu_t C_p}{\kappa_t} \quad (2.72)$$

equation (2.16) can be written in the form

$$\begin{aligned} \rho u \frac{\partial H}{\partial x} + \rho v \frac{\partial H}{\partial y} + \rho w \frac{\partial H}{\partial z} &= \frac{\partial}{\partial y} \left(\frac{\mu_t}{\text{Pr}_t} \frac{\partial H}{\partial y} \right) + \frac{\partial}{\partial z} \left(\frac{\mu_t}{\text{Pr}_t} \frac{\partial H}{\partial z} \right) \\ &+ \frac{\partial}{\partial y} \left[\left(1 - \frac{1}{\text{Pr}_t} \right) \mu_t u \frac{\partial u}{\partial y} \right] + \frac{\partial}{\partial z} \left[\left(1 - \frac{1}{\text{Pr}_t} \right) \mu_t u \frac{\partial u}{\partial z} \right] + \vec{j} \cdot \vec{E} \end{aligned} \quad (2.73)$$

The equations (2.15) and (2.73) are identical in form for non-MHD flows if the pressure gradient is zero and if the Prandtl number

equals unity. This fact can be exploited to obtain the relation (see Schlichting [Sc1]):

$$\frac{\rho_w}{\rho} = \frac{T}{T_w} = 1 + \left(\frac{T_{aw}}{T_w} - 1\right) \frac{u}{u_\infty} - \frac{\gamma-1}{2} M_\infty^2 \frac{T_\infty}{T_w} \left(\frac{u}{u_\infty}\right)^2 = 1 + b \frac{u}{u_\infty} - a^2 \left(\frac{u}{u_\infty}\right)^2 \quad (2.74)$$

Substituting (2.71) in (2.70) the relation is obtained

$$\frac{du}{dy} = \frac{1}{\kappa r} \sqrt{\frac{\tau_t}{\rho}} \frac{1}{y} \quad (2.75)$$

For incompressible flow ($\rho=\text{constant}$) Prandtl [Pr1] originally made the assumption that $\tau_t \approx \tau_w = \text{constant}$ (which is accurate only if the axial pressure gradient is zero) so that (2.75) can be integrated directly, leading to the first two terms in the right-hand side of equation (2.65). For compressible flow (2.74) must be substituted in (2.75), leading to the relation

$$\frac{d\left(\frac{u}{u_\infty}\right)}{\left[1 + b \frac{u}{u_\infty} - a^2 \left(\frac{u}{u_\infty}\right)^2\right]^{\frac{1}{2}}} = \frac{1}{u_\infty} \frac{1}{\kappa r} \sqrt{\frac{\tau_w}{\rho_w}} \frac{dy}{y} \quad (2.76)$$

in which the variables have already been separated. This can also be integrated directly and taking care that the incompressible relation results if $a=b=0$ van Driest obtained

$$\frac{u_{\text{eff}}}{v^*} = \frac{1}{\kappa r} \ln\left(\frac{y v^*}{v_t}\right) + B' = 2.5 \ln\left(\frac{y v^*}{v_t}\right) + 5.5 \quad (2.77)$$

Hére u_{eff} which has later been called the van Driest effective velocity, is defined by

$$u_{\text{eff}} = \frac{u_\infty}{a} \left\{ \sin^{-1} \left(\frac{2a^2 \frac{u}{u_\infty} - b}{\sqrt{b^2 + 4a^2}} \right) + \sin^{-1} \left(\frac{b}{\sqrt{b^2 + 4a^2}} \right) \right\} \quad (2.78)$$

Maise and McDonald [Mail] showed that experimental data on flat plates with compressibility and heat transfer effects correlate reasonably with the equations (2.77) and (2.78). For adiabatic

walls $b=0$ and the effective velocity reduces to

$$u_{\text{eff}} = \frac{u_{\infty}}{a} \sin^{-1} \left(\frac{au}{u_{\infty}} \right) \quad (2.79)$$

Alber and Coats [A11] used equations (2.77) and (2.79) to calculate adiabatic, compressible boundary layers by means of the integral approach. Since it has been assumed in the derivation of u_{eff} that the pressure gradient is zero, Alber and Coats added the law of the wake (third term in the right-hand side of equation 2.65) for the general case with a non-zero pressure gradient. Gerhart [Ger1] used a similar approach but since he was interested also in the possibility of reverse flow he added the unity in the logarithmic term and an exponential term similar to the last term in the right-hand side of equation (2.65). In this case about the complete equation (2.65) with u replaced by u_{eff} is used in an integral approach boundary layer calculation. To the author's knowledge no boundary layer calculations have been performed up to now with the complete expression (2.78), except in the original work of van Driest [Dr1]. It was used there to derive skin friction and heat transfer coefficients for a flat plate.

It has been mentioned above that Prandtl's original assumption $\tau_t \approx \tau_w$ is only valid if the axial pressure gradient is zero. Instead of equations (2.70) and (2.71) White and Christoph [Wh2] use for a situation with non-zero pressure gradient

$$\tau_t = \tau_w + \left(\frac{dp_{\infty}}{dx} \right) y = \rho \kappa^2 y^2 \left(\frac{du}{dy} \right)^2 \quad (2.80)$$

They also use the Crocco-Busemann relation (2.74) but v^* is used instead of u_{∞} for making the terms dimensionless. Equation (2.74) then becomes

$$\frac{\rho_w}{\rho} = 1 + \beta^* \frac{u}{v^*} - \gamma^* \left(\frac{u}{v^*} \right)^2 \quad (2.81)$$

where $\beta^* = q_w v_w / T_w \kappa v^*$ is a heat transfer parameter and $\gamma^* = r v^{*2} / 2 C_p T_w$ is a compressibility parameter. The equation corresponding to equation (2.76) can then be written as

$$\frac{d\left(\frac{u}{v^*}\right)}{\left[1 + \beta^* \frac{u}{v^*} - \gamma^* \left(\frac{u}{v^*}\right)^2\right]^{\frac{1}{2}}} = \frac{(1 + \alpha^* \frac{yv^*}{v_w})^{\frac{1}{2}}}{\kappa' \left(\frac{yv^*}{v_w}\right)} d\left(\frac{yv^*}{v_w}\right) \quad (2.82)$$

where $\alpha^* = v_w (dp_\infty/dx) / \tau_w v^*$ is the pressure gradient parameter. Again this can be integrated directly and, taking care that the incompressible relation results if α^* , β^* and γ^* are zero, White and Christoph obtain the relation

$$\frac{u}{v^*} \left(\frac{yv^*}{v_w}, \alpha^*, \beta^*, \gamma^* \right) = \frac{1}{2\gamma^*} \left(\beta^* + Q \sin \left\{ \phi + \frac{\sqrt{\gamma^*}}{\kappa'} [2(S-S_0) + \ln \left(\frac{S-1}{S+1} \frac{S_0+1}{S_0-1} \right)] \right\} \right) \quad (2.83)$$

with

$$\begin{aligned} \phi &= \sin^{-1}(-\beta^*/Q) \quad ; \quad Q = \sqrt{\beta^{*2} + 4\gamma^*} \\ S &= \sqrt{1 + \alpha^* \frac{yv^*}{v_w}} \quad ; \quad S_0 = \sqrt{1 + 0.1108\alpha^*} \end{aligned} \quad (2.84)$$

The approach of White and Christoph, leading to the complicated generalized law for the overlap layer in equation (2.83), is the most promising recent theoretical development in the area of profiles for non-MHD compressible, turbulent boundary layers.

2.6.3 The profiles for boundary layers in MHD generators

As stated earlier section 2.6 should lead to the choice of the velocity and enthalpy profiles to be used in calculating the turbulent boundary layers in MHD generators. It is clear from the previous section that a generalization of equation (2.78) or (2.83) to MHD conditions will lead to complicated expressions. In addition boundary layers in MHD generators experience special effects which are absent in non-MHD boundary layers. This will be illustrated in the present section leading to the choice of profiles, which are much simpler than those encountered in previous sections but which seem well suited to describe the behaviour under MHD conditions.

The special behaviour of the boundary layers in an MHD generator can be understood from considering the modifications of the integral equations due to the MHD effects. It has been discussed in section 2.4.6 that MHD effects are present only in the enthalpy integral equation if the electrode wall boundary layer is considered. This implies that the electrode wall velocity profile is similar to a non-MHD turbulent profile, which has been verified experimentally by Olin [O11]. In the enthalpy integral equation for the electrode wall boundary layer the MHD effect gives rise to an additional term, which is proportional to $j_y \Delta V$ and which denotes the electric power dissipated in the boundary layer resistance. The boundary layer resistance arises from the presence of a temperature profile in the boundary layer, which is coupled to a profile in electrical conductivity. This implies that the Joule dissipation j^2/σ_{eff} will be larger in the electrode wall boundary layer than in the core flow. The consequence of this is that it can lead to an overshoot in the temperature profile, which is distinctly different from the situation in a non-MHD turbulent boundary layer. Gertz et al. [Ge1] have derived an expression for the total enthalpy profile for a subsonic open cycle MHD generator, which allows for the possibility of an overshoot. The same profile will be used here to describe the electrode wall boundary layer in a supersonic closed cycle MHD generator, which implies that the following assumptions have been made (compare [Ge1])

- a. the enthalpy profile can be expressed as a universal function of u only but depends on the overshoot parameter $\Delta Q/Q_0$, which is the ratio of the excess heat flux to the wall due to the Joule dissipation in the boundary layer ΔQ with respect to the heat flux without MHD effect Q_0 .
- b. the increase in heat flux ΔQ is proportional to the increase in total enthalpy at the transition point between the laminar sublayer and the overlap layer.
- c. the increase in heat flux ΔQ is also proportional to the change in total enthalpy thickness $\delta_{H,e}$.

These are the assumptions which have to be made and they seem sufficiently realistic also for the situation studied here. Using

the Crocco-Busemann relation (2.74) for the non-MHD case Gertz et al. derived from the assumptions (a) to (c) the following expression

$$\frac{H - H_w}{H_\infty - H_w} = (1 - \alpha_e + \alpha_e U) \left\{ 1 + \frac{\Delta Q}{Q_0} \left(\frac{1-U}{1-U_T} \right) \left(1 + \frac{U-U_T}{1-U_T} \right) \right\} \quad (2.85)$$

Here U is the axial velocity component u made dimensionless with the core velocity u_∞ and U_T is the dimensionless velocity at the laminar-turbulent transition point

$$U_T = \frac{u_T}{u_\infty} = 11.8 \sqrt{\frac{\rho_\infty C_f}{\rho_w Z}} \quad (2.86)$$

The Reynolds analogy parameter $\alpha_e = 2St_e / C_{f,e}$ takes into account the effect of wall roughness on the heat transfer; its calculation will be described in section 2.8. The velocity profile for the electrode wall boundary layer is similar to that of a non-MHD turbulent boundary layer. Following Gertz et al. [Gel] the simple expression

$$\frac{u}{u_\infty} = \xi^{1/N_e} \quad (2.87)$$

is used where the parameter N_e is a variable, which changes its value according to the pressure gradient which the flow has experienced. Comparing the expressions for δ_2 and δ_H for a non-MHD situation in appendix A the relation following from assumption (c) can be understood

$$\frac{\Delta Q}{Q_0} = t \left(\alpha_e - \frac{\delta_{H,e}}{\delta_{2,e}} \right) \quad (2.88)$$

Here the parameter t can be calculated by substituting the enthalpy profile (2.85) into the definition of the total enthalpy thickness (2.54), after which the integral can be worked out analytically.

It has been discussed in section 2.4.5 that there are additional terms due to MHD effects in all three insulator wall boundary layer equations. Since the MHD term both in the momentum and in the enthalpy integral equation is proportional to $\delta_{j,i}$, however, the

main effect for the insulator wall boundary layer results from the profile in j_y . As mentioned already in section 2.4.5, j_y varies considerably in the insulator wall boundary layer and even reverses its sign. Since the retarding Lorentz force in the insulator wall boundary layer is in general smaller than in the core flow, an overshoot in the velocity profile can develop. This is the main difference with the situation in a non-MHD turbulent boundary layer, since Gertz et al. claim that two-dimensional calculations show that the enthalpy profile remains essentially unperturbed even under strong MHD interaction. In that case the enthalpy profile can be accurately represented by a power law, which following Gertz et al. is written as

$$\frac{H - H_w}{H_\infty - H_w} = 1 - \alpha_i + \alpha_i \xi^{1/7} \quad (2.89)$$

In the derivation of the velocity profile for the insulator wall boundary layer Gertz et al. use a similar approach as that of White and Christoph [Wh2] discussed in section 2.6.2. When the Lorentz force is important Prandtl's original assumption that $\tau_t \cong \tau_w \cong$ constant has to be modified and instead of equation (2.80) Gertz et al. use the relation

$$\tau_t = \tau_w - j_y B z = \rho \kappa^{1/2} z^2 \left(\frac{du}{dz} \right)^2 \quad (2.90)$$

It follows from section 2.6.2. that this expression can be integrated directly to obtain the velocity profile. Gertz et al. [Ge1] claim that this profile can be approximated reasonably by the expression

$$\frac{u}{u_\infty} = (1 + R_i) \xi^{1/7} - R_i \xi^{1.08} \quad (2.91)$$

which will be also used here. It is worthwhile to note that the boundary layer profiles in this section are determined in general by two parameters. Equation (2.65) shows that these parameters are δ and $\bar{\Pi}$ for non-MHD boundary layers. Equations (2.57), (2.89) and (2.91) show that R_i and δ_i^* determine the insulator wall boundary layer, whereas equations (2.85) and (2.87) show that, due to the

possibility of an overshoot in the enthalpy profile, the electrode wall boundary layer needs three parameters, namely N_e , δ'_e and $\Delta Q/Q_0$.

2.7 Relations for a normal shock wave interacting with the boundary layer

A normal shock wave is introduced at (or slightly upstream of) a location in the MHD generator where the calculation with the core flow and boundary layer model would indicate boundary layer separation (if it appears). This is realistic because boundary layer separation leads to an abrupt reduction in effective cross-section A_{eff} , which in supersonic flow induces shock waves. In reality a pattern of oblique shock waves will usually arise yielding two-dimensional phenomena which are very complicated to describe. Since it is the aim of the present work to develop a fast computer code for engineering purposes, the one-dimensional approximation has been introduced and consistent with this approximation the shock wave pattern is simplified to one normal shock. It will be clear, however, from this discussion that the usual normal shock relations, which assume a constant cross-sectional area, can not be used in the situation of a normal shock wave induced by boundary layer separation.

Therefore new relations have to be constructed to describe a normal shock wave in a situation, where the values of A_{eff} upstream and downstream of the shock are different. To do this the principles in AVCO Everett's MHD4 computer code [MHD4] will be followed and extended. In the AVCO code the following relations, connecting flow variables upstream (subscript x) and downstream of the normal shock (subscript y), are used

Conservation of mass

$$(\rho_{\infty} u_{\infty} A_{eff})_x = (\rho_{\infty} u_{\infty} A_{eff})_y \quad (2.92)$$

Conservation of average energy

$$\langle H \rangle_x = \langle H \rangle_y \quad (2.93)$$

Normal shock ratio of average stagnation pressures

$$\frac{\langle p_s \rangle_y}{\langle p_s \rangle_x} = \left[\frac{\frac{\gamma+1}{2} M_{\infty x}^2}{1 + \frac{\gamma-1}{2} M_{\infty x}^2} \right]^{\frac{\gamma}{\gamma-1}} \left[\frac{2\gamma}{\gamma+1} M_{\infty x}^2 - \frac{\gamma-1}{\gamma+1} \right]^{\frac{-1}{\gamma-1}} \quad (2.94)$$

These relations allow a change in the value of A_{eff} and thus of $\delta_{1,e}$ and $\delta_{1,i}$, in passing through the shock, which is the essential difference with the usual normal shock relations. The average values of the stagnation enthalpy and the stagnation pressure, which appear in the above relations, denote an average over the channel cross-section and thus depend on the boundary layer thicknesses. In [MHD4] these averages are calculated according to the principle of an imaginary, non-isentropic compression of the flow, where the boundary layer thicknesses are updated in each small compression step. This approach is necessary in the AVCO code, since it considers open cycle MHD conditions, where the medium has a ratio of specific heats depending upon the temperature. Since the ratio of specific heats γ is constant for a cesium seeded argon plasma, as considered in this thesis, the calculation of averages upstream of the shock is less complicated. Downstream of the shock the expansion always has to take place in small steps, since the values of $\delta_{1,e}$ and $\delta_{1,i}$ are not known beforehand. The calculation of the average stagnation pressure and enthalpy can be worked out exactly by using the enthalpy and velocity profile. Here this calculation is simplified considerably by approximating the flow situation by means of a core region with uniform velocity u_{∞} and boundary regions along the walls with thicknesses $\delta_{1,e}$ and $\delta_{1,i}$, where the velocity is assumed to be zero (consistent with the definitions of $\delta_{1,e}$ and $\delta_{1,i}$). In the quasi-one-dimensional approximation the static pressure is assumed to be uniform over the cross-section, so that the stagnation pressure in the boundary regions equals the static pressure. The averaging then yields

$$\langle p_s \rangle = p_{s\infty} - 2 \left(\frac{\delta_{1,e}}{h} + \frac{\delta_{1,i}}{b} \right) (p_{s\infty} - p) \quad (2.95)$$

For the calculation of the average stagnation enthalpy the same approximation is used. The equations (2.85) and (2.89) show that in the boundary regions of thickness $\delta_{1,e}$ and $\delta_{1,i}$ the relation $H \approx H_w$ holds, where it has been assumed that α_e and α_i have values close to one. Averaging then results in

$$\langle H \rangle = H_\infty - 2 \left(\frac{\delta_{1,e}}{h} + \frac{\delta_{1,i}}{b} \right) (H_\infty - H_w) \quad (2.96)$$

Admittedly the approximations in the expressions (2.95) and (2.96) are rather crude, but they simplify the algebra, needed to calculate the conditions downstream of the shock, considerably.

The equations (2.92) to (2.96) are sufficient to calculate the conditions downstream of the normal shock, if the boundary layer parameters N_e , δ_e' , $\Delta Q/Q_0$, R_i and δ_i' are assumed to be constant in passing through the shock. This corresponds with the approach in [MHD4]. Numerical experiments have been performed with this procedure to check the behaviour of the normal shock under various conditions. It has been discovered in this way that it is possible to improve the description of the normal shock by adding the following relation

Normal shock ratio of core Mach numbers

$$M_{\infty y}^2 = \left(M_{\infty x}^2 + \frac{2}{\gamma-1} \right) \left(\frac{2\gamma}{\gamma-1} M_{\infty x}^2 - 1 \right)^{-1} \quad (2.97)$$

The reason that this relation can also be satisfied in the approach described here, may be due to the relatively simple set of equations for closed cycle MHD conditions.

It should be noted that it is inconvenient to assume all boundary layer parameters to be constant in passing the normal shock, when a non-MHD boundary layer model is used, which includes the correlation equation (2.58). In general boundary layer separation will occur, when the incompressible shape factor \bar{H}_{12} is approximately two [Sal]. When \bar{H}_{12} equals two and is constant in passing the shock, the exponential term in equation (2.58), the argument of which is proportional to $(\bar{H}_{12}-1.4)$, will give numerical problems downstream of the shock. Therefore, when equation (2.58)

is used in a non-MHD boundary layer model, this problem can be avoided by making the additional, though arbitrary assumption that $\bar{H}_{12,y} = 0.8\bar{H}_{12,x}$.

2.8 Relations for the skin friction and heat transfer coefficients and for the dissipation integral

It will be clear that the relations used for the parameters mentioned in the section heading and appearing in the calculations are important inputs into the integral boundary layer equations, so that a review of what is available in the literature will be useful. The literature on correlation functions for St and C_D is very limited, and the discussion therefore short. Since C_f can not only be determined from an empirical correlation, but may also be derived from a realistic velocity profile, there will be a coupling with the discussion in section 2.6.

Skin friction coefficient C_f

The most widely used empirical correlation for the skin friction coefficient has been constructed by Ludwig and Tillmann [Lul] and can be written as

$$\bar{C}_f = 0.246 \operatorname{Re}_{\delta_2}^{-0.268} \exp(-1.561 \bar{H}_{12}) \quad (2.98)$$

This expression for \bar{C}_f in terms of $\bar{\delta}_2$ and \bar{H}_{12} is valid for an incompressible flow along a smooth wall with pressure gradient. For a derivation of a comparable expression from a realistic velocity profile only the first three terms in the right-hand side of equation(2.65) are considered

$$\frac{u}{v^*} = \frac{1}{\kappa} \ln\left(\frac{yv^*}{v}\right) + B' + \frac{\tilde{\pi}}{\kappa} \left[1 - \cos\left(\frac{\pi y}{\delta}\right)\right] \quad (2.65)$$

where the unit in the logarithmic term has been omitted. Expressions for $\bar{\delta}_1$ and $\bar{\delta}_2$ can be obtained from this relation through direct integration and may be written as [Whl]

$$\frac{\bar{\delta}_1}{\delta} = \frac{1 + \tilde{\pi}}{\kappa' \lambda}$$

$$\frac{\bar{\delta}_2}{\delta} = \frac{1 + \tilde{\pi}}{\kappa' \lambda} - \frac{2 + 3.179\tilde{\pi} + 1.5\tilde{\pi}^2}{\kappa'^2 \lambda^2} \quad (2.99)$$

$$\text{where } \lambda = \sqrt{\frac{2}{C_f}} \quad (2.100)$$

It is clear from these relations that dividing $\bar{\delta}_1$ by $\bar{\delta}_2$ yields an expression for \bar{H}_{12} as a function of λ and $\tilde{\pi}$. Coles [Col] has pointed out that substituting $y=\delta$ in the velocity profile will give an additional relation, from which an expression for \bar{C}_f can be obtained. Since $u=u_\infty$ at $y=\delta$ this substitution in equation (2.65) leads to

$$\frac{u_\infty}{v^*} = \lambda = \frac{1}{\kappa'} \ln\left(\frac{v^* \delta}{\nu}\right) + B' + \frac{2\tilde{\pi}}{\kappa'} = \frac{1}{\kappa'} \ln\left(\frac{Re_\delta}{\lambda}\right) + B' + \frac{2\tilde{\pi}}{\kappa'} \quad (2.101)$$

In this way a relation has been obtained for λ or \bar{C}_f as a function of Re_δ and $\tilde{\pi}$. White [Wh1] has shown that the parameter $\tilde{\pi}$ can be eliminated between equation (2.101) and the relation for \bar{H}_{12} obtained from $\bar{\delta}_1$ and $\bar{\delta}_2$ in (2.99). This relation can then also be written in terms of Re_{δ_2} instead of Re_δ . Using the numerical values $\kappa'=0.4$ and $B'=5.5$ the result is [Wh1]

$$C_f = \frac{0.288e^{-1.37\bar{H}_{12}}}{(\log Re_{\delta_2})^{1.753+0.283\bar{H}_{12}}} \quad (2.102)$$

The similarity of this expression with the Ludwig Tillmann relation is clear but White claims that the accuracy of equation (2.102) is $\pm 3\%$ whereas this is only $\pm 10\%$ for the Ludwig Tillmann relation (2.98). Up to this point expressions for the skin friction coefficient have been discussed which are valid only for an incompressible flow along a smooth wall. The influence of compressibility has been taken into account by Reshotko and Tucker [Re1] with an empirical approach. This relation can be written as

$$C_f = 0.246 \operatorname{Re}_{\delta_2}^{-0.268} \exp(-1.561 \bar{H}_{12}) \left(\frac{T_\infty}{T_w}\right)^{1.268} \quad (2.103)$$

The compressibility correction may also be determined from the velocity profile which has been generalized by van Driest to the relation (2.78). Then the skin friction coefficient can be written as [Dr1]

$$C_f = \frac{1}{F_S} \bar{C}_f(\operatorname{Re}_x F_{Rx})$$

$$\text{where } F_S = \frac{\frac{T_{aw}}{T_\infty} - 1}{\left[\sin^{-1}\left(\frac{2a^2 - b}{\sqrt{b^2 + 4a^2}}\right) + \sin^{-1}\left(\frac{b}{\sqrt{b^2 + 4a^2}}\right) \right]^2}$$

$$\text{and } F_{Rx} = \frac{v_\infty}{v_w} \frac{1}{F_S} \quad (2.104)$$

This form has been suggested by Spalding and Chi [Spal] as an expression for C_f in a compressible flow along a smooth flat plate. The influence of wall roughness and pressure gradient is taken into account by Spalding and Chi with an empirical correction of the following form

$$C_f = \frac{2}{F_S \left\{ \frac{1}{\kappa^*} \log(F_\delta \operatorname{Re}_{\delta_2}) + B' - \frac{\Delta u_1}{v^*} + \frac{\Delta u_2}{v^*} \right\}^2} \quad (2.105)$$

Here Δu_1 takes into account the influence of wall roughness and Δu_2 the influence of pressure gradient. Spalding and Chi present simple algebraic expressions for Δu_1 and Δu_2 and tables for F_S and F_δ in terms of M and T_w/T_∞ so that the calculation of C_f is rather easy. The approach of White and Christoph [Wh2] described in section 2.6.2 can also yield an expression for C_f . White [Wh1] claims that this approach gives an expression for C_f which is identical with equation (2.104) for a flow along a flat plate. In the general case the White and Christoph approach gives an expression for C_f where the correction for the effect of a pressure gradient is derived from theoretical arguments. This approach can apparently be

formulated in such a general sense that White and Christoph [Wh2] claim that besides the effects of pressure gradient, heat transfer and compressibility also the effects of wall roughness, wall transpiration and wall curvature on C_f can be taken into account. The method is, however, so complicated that no further details will be given here. As a final remark in the discussion of expressions for the skin friction factor which can be derived from a relation for the velocity profile, it must be stated that the profiles discussed in section 2.6.3 are too simple for this purpose. A completely different expression for the skin friction coefficient in a compressible flow with pressure gradient along a smooth wall has been put forward by Walz [Wal] in the form

$$C_f = 2 \frac{a'}{b'} \operatorname{Re}_{\delta_2}^{-0.268}$$

$$a' = 0.0394 \left(\frac{\delta_3}{\delta_2} - 1.515 \right)^{0.7}$$

$$b' = 1 + 0.88 \frac{\gamma-1}{2} M_\infty^2 \left(\frac{\delta_3}{\delta_2} - \theta \right) \left(2 - \frac{\delta_3}{\delta_2} \right)$$

$$\theta = \frac{T_{aw} - T_w}{T_{aw} - T_\infty} \quad (2.106)$$

A generally accepted criterion for separation in a turbulent compressible flow is that $\delta_3/\delta_2=1.515$ which is the reason that C_f is designed to vanish at this point. This is an attractive feature of this expression but it may also be too much of an arbitrary assumption. Apart from the fact that the basis of this expression is found in a large number of empirical relations, a drawback is that its accuracy has not been tested in experiments. A further drawback is that Walz does not indicate how the effect of wall roughness can be taken into account.

It is useful to round off this short review of the literature by looking at the available information about the influence of MHD effects on the skin friction coefficient. There is very little information available in the literature on this effect but Rosa

[Rol] states that C_f can be approximated for turbulent MHD flow by the expression

$$C_f = 0.064 \left(\frac{\sigma B^2 x}{\rho_\infty u_\infty \text{Re}_x} \right)^{1/5} \quad (2.107)$$

In this relation a simple flat plate expression for C_f can be recognized, which is corrected by the MHD interaction parameter $N^* = \sigma B^2 x / \rho_\infty u_\infty$. This interaction parameter can reach values up to 4 for conditions of large scale MHD generators. To the author's knowledge no expression for C_f is available in which the combined influences of pressure gradient, compressibility and MHD effects are taken into account.

Since the only relation for the dissipation integral C_D found in the literature is valid for a smooth wall, it is preferred to use in this thesis also a smooth wall expression for C_f . In that case a roughness factor R_f can be introduced as a multiplication factor for both C_f and C_D so that the correction is equal for the two parameters. Because of the simplicity of the calculation of C_f the expressions of Reshotko and Tucker (2.103) and of Walz (2.106) are preferred over those of Spalding and Chi (2.104). In this thesis the calculations will be performed with the relation of Reshotko and Tucker, since it is not certain that the expression of Walz will yield a greater accuracy.

Heat transfer coefficient

A recent review of experimental data on skin friction and heat transfer in compressible turbulent boundary layers along rough walls has been presented by Seidman [Sel]. The theory of heat transfer goes back to earlier work of Owen and Thomson [Owl], who used a modified Reynolds analogy to relate C_{fr} to the Stanton number St . The calculation of the Reynolds analogy parameter $\alpha = 2St/C_{fr}$ then follows from empirical relations in terms of the friction velocity v^* already defined in (2.66) and the Stanton number for the laminar sublayer St^* in the form

In these relations k^* is the roughness height of the wall so that wall roughness is the main effect which makes α unequal to one.

Dissipation integral C_D

All information which can be found in the literature on the dissipation integral goes back to the book by Walz [Wal]. In this approach C_{Ds} is calculated from the following empirical relation

$$C_{Ds} = \gamma_t \frac{\delta_2}{\bar{\delta}_2} \text{Re}_{\delta_2}^{-n^*}$$

where

$$\gamma_t = 0.00481 + 0.0822 \left(\frac{\bar{\delta}_3}{\bar{\delta}_2} - 1.5 \right)^{4.81}$$

$$n^* = 0.2317 \frac{\bar{\delta}_3}{\bar{\delta}_2} - 0.2644 - 0.87_{10} 5 \left\{ 2 - \frac{\bar{\delta}_3}{\bar{\delta}_2} \right\}^{20} \quad (2.109)$$

These relations for the dissipation integral are only valid for a smooth wall, as indicated by the subscript s. The effect of wall roughness is taken into account by multiplying C_{Ds} with the roughness factor R_f .

Roughness factor R_f

The roughness factor is defined in terms of Schlichting's [Sch] friction coefficients for a smooth flat plate C_{fs}^* and for a rough flat plate C_{fr}^* . For a large flat plate equation (2.45) reduces to

$$\frac{d\delta_2}{dx} = \frac{C_f}{2}$$

and thus

$$\delta_2 = \int_0^x \frac{C_f}{2} dx \quad (2.110)$$

Given the momentum thickness at a certain location, the expressions

for C_{fs}^* and C_{fr}^* can be integrated to x until the given δ_2 is reached

$$\delta_2 = \int_0^{x_s} \frac{C_{fs}^*}{2} dx = \int_0^{x_r} \frac{C_{fr}^*}{2} dx \quad (2.111)$$

The roughness factor is then defined as

$$R_f = \frac{C_{fr}^*(x_r)}{C_{fs}^*(x_s)} \quad (2.112)$$

Influence of overshoot profiles

It has been discussed in section 2.6.3 that the MHD effects can lead to an overshoot in the enthalpy profile at the electrode wall and an overshoot in the velocity profile at the insulator wall. These effects will influence the values of C_f and St but they have not yet been taken into account. Since the heat flux to the electrode wall is proportional to $Q_0 + \Delta Q$ the Stanton number can be approximated by

$$St_e = St_0 \left(1 + \frac{\Delta Q}{Q_0}\right) \quad (2.113)$$

Considering the effect of the overshoot in the velocity profile at the insulator wall it may be noted that the transport properties are mainly determined by the laminar sublayer. In that case the second term in equation (2.91) can be neglected with respect to the first, which implies that the transport properties are approximated by the values in non-MHD flows at a bulk velocity $(1+R_i)u_\infty$.

Introducing this correction only as a final multiplication factor and looking back at the definitions of C_f , C_D and St the correction for velocity overshoot at the insulator wall can then be written as (see also [Gel])

$$\begin{aligned} C_{f,i} &= C_{f0} (1 + R_i)^2 \\ St_i &= St_0 (1 + R_i) \\ C_{D,i} &= C_{D0} (1 + R_i)^3 \end{aligned} \quad (2.114)$$

In the equations (2.113) and (2.114) the subscript 0 indicates the classical situation without overshoot profiles, for which C_f , St and C_D are calculated as described above.

2.9 The calculation of the voltage drop and the current density displacement thickness

In order to derive a theoretical expression for the voltage drop due to the flow boundary layer the starting point will be Ohm's law. In terms of the components along the x and y directions equation (2.26) can be written as

$$-j_y = \sigma(uB - E_y) - \beta j_x \quad (2.115)$$

$$j_x = \sigma E_x - \beta j_y \quad (2.116)$$

Eliminating j_x in equation (2.115) by means of equation (2.116) gives the relation

$$-\left(\frac{1 + \beta^2}{\sigma}\right)j_y = uB - E_y - \beta E_x \quad (2.117)$$

This relation is sufficient to calculate the voltage drop of one boundary layer, which can be defined as (compare figure 5)

$$\frac{\Delta V}{2} = \int_{-h/2}^0 (E_{y\infty} - E_y) dy \quad (2.118)$$

Equation (2.117) can be used both in the core and in the boundary layer so that substitution into equation (2.118) leads to

$$\frac{\Delta V}{2} = \left\{ u_{\infty} B - \beta_{\infty} E_x + \left(\frac{1 + \beta_{\infty}^2}{\sigma_{\infty}}\right)j_y \right\} \delta - \int_{-h/2}^{-h/2 + \delta} \left\{ uB - \beta E_x + \left(\frac{1 + \beta^2}{\sigma}\right)j_y \right\} dy$$

$$\begin{aligned} \text{or } \frac{\Delta V}{Z} = & u_{\infty} B \int_{-h/2}^0 \left(1 - \frac{u}{u_{\infty}}\right) dy - \beta_{\infty} E_x \int_{-h/2}^0 \left(1 - \frac{\beta}{\beta_{\infty}}\right) dy \\ & + \left(\frac{1 + \beta_{\infty}^2}{\sigma_{\infty}}\right) j_y \int_{-h/2}^0 \left\{1 - \left(\frac{1 + \beta_{\infty}^2}{1 + \beta_{\infty}}\right) \frac{\sigma_{\infty}}{\sigma}\right\} dy \end{aligned} \quad (2.119)$$

To obtain this expression the fact has been used that j_y and E_x are constant through the boundary layer which is a consequence of the equations (2.2) and (2.3). The relation (2.119) can be simplified further by noting that we have to use the effective values for β and σ and that β_{eff} is constant. Then equation (2.119) simplifies to

$$\frac{\Delta V}{Z} = u_{\infty} B \int_{-h/2}^0 \left(1 - \frac{u}{u_{\infty}}\right) dy + \frac{1 + \beta_{\text{eff}}^2}{\sigma_{\text{eff}\infty}} j_y \int_{-h/2}^0 \left(1 - \frac{\sigma_{\text{eff}\infty}}{\sigma_{\text{eff}}}\right) dy \quad (2.120)$$

This relation is identical with the one presented by Rosa [Ro2]. As soon as the velocity and enthalpy profile are known the first integral can be calculated. For the calculation of the second integral the Saha equations and the energy balance for the electrons, equation (2.29), are also needed. When used in the computer program, the integrals are calculated numerically. The results show that the contribution of the second integral in (2.120) can be neglected with respect to the first. This is because the electron temperature T_e and therefore the electrical conductivity σ_{eff} are approximately constant and independent of the shape of the profile of the gas temperature since j_y is constant in the calculation.

It has been mentioned already in section 2.1 that the voltage drop connected with the phenomena in the Debye sheath along the wall will not be included in this thesis. The physical background of this phenomenon is completely different from the one considered here. It is very complicated to describe since it requires the solution of the equations of the electron gas in the form of differential equations. The problem has been solved by Koester [Ko1] and Dolson [Dol1] but the results are not presented in such a form

that they could be easily incorporated here. Therefore if equation (2.120) is used in the calculations a multiplication factor will be introduced under the assumption that the ratio $(R_{BL} + R_S)/R_{BL}$ is a constant (see figure 5). This multiplication factor may be adjusted such that the theoretical and experimental values of ΔV will be equal in the middle of the generator channel.

For the calculation of the current density displacement thickness at the insulator wall which is defined as

$$\delta_{j,i} = -b/2 \int_0^0 \left(1 - \frac{j_y}{j_{y\infty}}\right) dz \quad (2.121)$$

one must take into account that $E_y^* = uB - E_y$ varies strongly through the boundary layer and can even reverse its sign. An exact calculation of $\delta_{j,i}$ could be performed by relating j_y and E_y^* through a solution of the Saha equations, Ohm's law and the energy balance for the electron gas. Although this is a set of algebraic equations its solution is rather complicated and since the integral (2.121) must be calculated numerically it takes relatively much computer time. In order to obtain some insight the relation between j_y and E_y^* has been calculated for the conditions at the inlet of the generator in the Eindhoven University of Technology blow-down experiment and is shown in figure 7. It is clear from this figure that the curve can be reasonably approximated in the region of interest by the drawn straight line which follows the relation (at a seed ratio of 10^{-3})

$$|j_y| = A^* |E_y^*|^6 \quad (2.122)$$

where A^* is a constant. This relation will be used in the numerical determination of the integral (2.121) which leads to a considerable simplification of the calculation. It should be noted that the relations (2.31) and (2.32) for σ_{eff} and β_{eff} , with $\beta_{crit} = 1.5$, have been used in calculating the curve in figure 7.

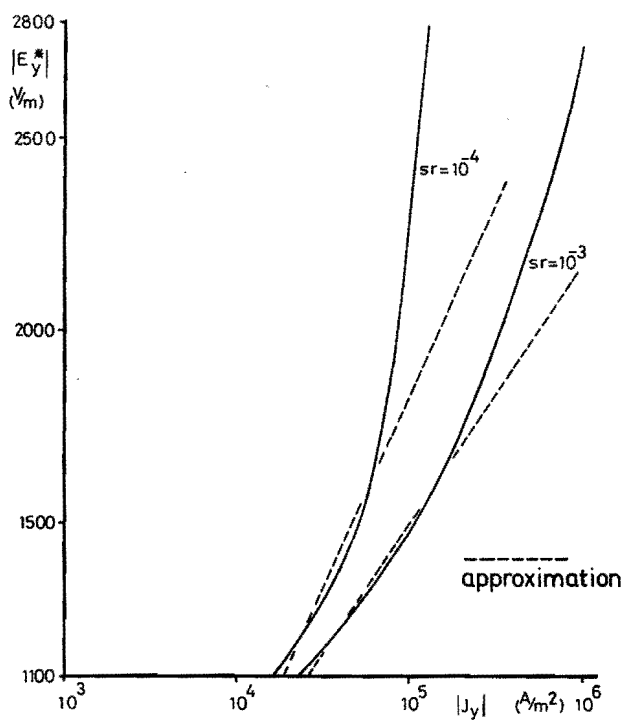


Fig. 7 Relation between the absolute values of the current density j_y and the total electric field E_y^* at two values of the seed ratio.

3 Results of numerical calculations

In this chapter the main results of the three models with different levels of accuracy, as described in chapter 2, will be presented and discussed. It will be shown that the most complete model is needed to describe the flow in an MHD generator under strong interaction conditions. The results have been calculated for the standard conditions of the Eindhoven University of Technology (EUT) blow-down experiment namely a magnetic induction of 5.3 T, a seed ratio of 0.1% (volume ratio), inlet stagnation temperature of 2000 K and inlet stagnation pressure of 7 bar. A constant total voltage drop has been used in the calculations which equals in general 150 V unless explicitly stated otherwise. This value should be seen as a first approximation to the experimental values obtained in measurement series 2 (the different measurement series are defined in chapter 4). Each of the 32 electrode pairs of the segmented Faraday generator is loaded with the same external resistance.

The calculations have been performed for the geometrical dimensions of the hot flow train of the EUT blow-down experiment. This hot flow train consists of a nozzle, an MHD generator, a supersonic and a subsonic diffuser (see figure 29). The MHD generator diverges from $0.05 \times 0.154 \text{ m}^2$ to $0.18 \times 0.154 \text{ m}^2$ over a length of 0.8 m. The electrode walls are parallel and the Mach number at the inlet of the generator is 1.7. Downstream of the generator follows a supersonic diffuser with a constant cross-section of $0.18 \times 0.154 \text{ m}^2$ and a length of 2.225 m. The purpose of the supersonic diffuser is to provoke a gradual decrease of the Mach number by means of a system of oblique shocks which interfere with each other and which reflect from the walls. The result of this process is that the loss in stagnation pressure over the normal shock, in which the transition to subsonic flow takes place, will be reduced. The last element of the hot flow train is the subsonic diffuser which diverges from $0.18 \times 0.154 \text{ m}^2$ to $0.256 \times 0.23 \text{ m}^2$ over a length of 0.97 m. It is intended that the normal shock will occur in the subsonic diffuser; the position of the normal shock is then stabilized due to the divergence of the walls.

3.1 Quasi-one-dimensional MHD flow model

In this section results will be presented from solving the equations (2.21) to (2.23) together with the electron gas equations presented in section 2.2.3 (including ionization instabilities and voltage drop). The equations (2.22) and (2.23) show that the influence of the boundary layers are averaged out over the circumference of the cross-section. The results in this section are taken from Krause [Krl] who used the following expressions for the shear stress and the heat loss at the walls

$$\tau_{xy,w} = C_f \frac{1}{2} \rho_\infty u_\infty^2$$

with

$$C_f = 0.058 Re_x^{-0.2}$$

$$Re_x = \frac{\rho u(x + il)}{\eta}$$

$$\eta = 1.218 \times 10^{-6} (T - 102)^{0.554} \quad (3.1)$$

and

$$q_{y,w} = \alpha_x (T_{aw} - T_w)$$

with

$$\alpha_x = \frac{\lambda Nu_x}{x + il}$$

$$Nu_x = 0.0236 Re_x^{0.8}$$

$$\lambda = \frac{15}{4} Rn \quad (3.2)$$

In these expressions il is the length of the channel in front of the generator section. The expressions above are valid for a smooth flat plate; in order to take wall roughness into account C_f is multiplied by a factor 2. The results of the calculations with this model are presented in figures 8 and 9. They show the variation of Mach number and static pressure as a function of the coordinate x along the hot flow train. The figures show that the external load resistance R_L and therefore the MHD interaction have a strong influence on the shape of the curves. For instance, when the MHD

interaction increases (decreasing R_L) the normal shock moves upstream in the subsonic diffuser and the shock strength decreases.

In the calculations the location of the shock is determined in such a way that the exit pressure equals 1 bar so that the flow can exhaust into the atmosphere. At a certain value of the MHD interaction ($R_L = 9 \Omega$) the special situation arises that the flow is supersonic until $x \approx 3$ m and the Mach number just reaches the value 1 at the end of the supersonic diffuser (choking). In this situation the normal shock is still located in the subsonic diffuser but it is clear that this will no longer be the case when the MHD interaction is increased further. The calculations show that the requirement that the exit pressure equals 1 bar can no longer be fulfilled when R_L is smaller than 9Ω and when the normal shock is located in the MHD generator. In this situation the shock location is adjusted in such a way that choking ($M=1$) still occurs at the end of the supersonic diffuser. The flow behaviour for such a situation is illustrated by the curve for $R_L = 4 \Omega$ in the figures 8 and 9. These figures show that according to this model the length of the supersonic diffuser forms the limitation upon the enthalpy extraction. This will be clear by realizing that with a shorter supersonic diffuser the choking condition ($M=1$) at the end of this diffuser would be reached at a higher value of the MHD interaction.

3.2 The model of MHD core flow and non-MHD boundary layers

In this section results will be presented from solving the equations (2.35) to (2.37) together with the electron gas equations presented in section 2.2.3. The boundary layer is described by the momentum integral equation (2.45) without the MHD term and the correlation equation of Garner (2.58). In this description the boundary layers along the electrode wall and along the insulator wall are assumed to be identical. The results in this section are taken from Massee [Ma1] who used the same expression for the friction coefficient C_f as in equation (3.1). This investigation represented a first attempt to describe the gasdynamic processes in

the hot flow train of the EUT blow-down experiment in a more realistic way. Surely, a more realistic expression for C_f could have been used which would take into account the influences of wall roughness and of boundary layer shape factor as described in section 2.8.

The most important results of the calculations with this model are presented in the figures 10 to 15 for various values of the MHD interaction. Figures 10 and 11 show the variation of Mach number and static pressure through the hot flow train which may be compared directly with the figures 8 and 9. The corresponding figures look very similar but the presence of the normal shock in the MHD generator at $R_L=4 \Omega$ is now caused by boundary layer separation as can be seen from figure 12. It should be noted that both models predict a normal shock in the MHD generator at $R_L=4 \Omega$. This coincidence is due to the values used for the friction coefficient C_f in the calculations.

If the C_f values are doubled throughout the entire hot flow train the present model indicates boundary layer separation in the supersonic diffuser at $x=2.82$ m for $R_L=6 \Omega$ where \bar{H}_{12} reaches a value of 1.61. This implies an upstream displacement of the shock from $x=3.22$ to $x=2.82$ m. It may be expected, however, that the shock will not stay in the constant area supersonic diffuser but will move upstream to the generator outlet by influencing the boundary layer upstream of its earlier position. Under these circumstances the shock will reach the MHD generator already at $R_L=6 \Omega$ according to the present model.

As mentioned before the location where boundary layer separation occurs can be read from figure 12 where the incompressible shape factor \bar{H}_{12} is plotted as a function of distance in the hot flow train. The usual criterion for boundary layer separation found in the literature is $\bar{H}_{12} \geq 2$ (see for instance Sandborn and Kline [Sa1]). Because of the large positive gradient of \bar{H}_{12} at $x=0.65$ m for $R_L=4 \Omega$ the value $\bar{H}_{12}=2$ will be reached in a short distance from $x=0.65$ m. The jump in the value of \bar{H}_{12} when passing through a normal shock has been introduced arbitrarily in order to avoid numerical problems with Garner's equation (2.58) as has been discussed already in section 2.7.

Figure 13 shows the electric current per electrode pair I_{e1} in the MHD generator at load resistances of 4, 6 and 8 Ω . The fact that I_{e1} increases when R_L decreases as shown in figure 13 is a behaviour which is typical of all electric generators. The fact that I_{e1} decreases approximately a factor two when passing through the normal shock at $R_L=4 \Omega$ can be explained from the corresponding change in velocity. The curve for $R_L=4 \Omega$ in figure 13 indicates that the presence of the normal shock wave in the generator limits the enthalpy extraction. In other words the present model leads to the conclusion that the divergence of the MHD generator is the limiting factor to the enthalpy extraction because it leads to boundary layer separation and therefore to a shock wave in the MHD generator. The calculations, however, also indicate that this limitation can be circumvented by an increase of the stagnation pressure. At 4 Ω loading and a stagnation pressure of 9 bar \bar{H}_{12} is limited to a value 1.62 and the shock wave is located in the subsonic diffuser.

Another way to avoid this limitation is to increase the divergence of the MHD generator but calculations to determine the feasibility of this solution have not been performed.

Figures 14 and 15 show the boundary layer thicknesses δ_1 and δ_2 as a function of distance in the hot flow train under different loading conditions. It is seen that δ_1 decreases and δ_2 increases when passing through the normal shock wave. It is desirable to check this result, which is a consequence of the normal shock model described in section 2.7, with experimental work. Up to now, however, no experimental results on the behaviour of δ_1 and δ_2 when passing through a normal shock are available.

Figure 15 shows that apart from the effect of the shock wave, δ_2 increases with increasing MHD interaction as was expected beforehand. The major disadvantage of the simple description of the boundary layer in the present model follows from figure 14. Here it appears that δ_1 decreases with increasing MHD interaction which completely disagrees with the expectations developed from physical reasoning and insight. This may be explained from the fact that there is no MHD effect included in the boundary layer equations. In the present model δ_1 is determined mainly by the core properties M_∞ .

and T_∞ according to equations (A2) and (A3) of appendix A. Since the Reynolds analogy parameter α equals one in this model the expression for δ_1 can be written as

$$\delta_1 = \left[\left(\frac{T_w}{T_\infty} \right) + \frac{M_\infty^2}{3} \left(\frac{N}{N+2} \right) \right] \left(\frac{\delta_1'}{N+1} \right) \quad (3.3)$$

The behaviour shown in figure 14 for instance at $x=3.03$ m can be explained by noting that M_∞ is a factor 2.1 larger and T_∞ is a factor 1.9 smaller (mainly due to the large value of M_∞) for the situation at $R_L=10^4 \Omega$ compared to that at $R_L=6 \Omega$.

The drawback of the present model illustrated by figure 14 leads to the conclusion that MHD effects have to be taken into account in the boundary layer equations in order to obtain a realistic description of the gasdynamical behaviour of an MHD generator at strong interaction.

3.3 The model of MHD core flow and MHD boundary layers

In this model the core flow description is identical to that in section 3.2 but the boundary layers are described by the momentum integral equation (2.45), the kinetic energy integral equation (2.50) and the stagnation-enthalpy integral equation (2.55). For the friction coefficient C_f the empirical relation of Reshotko and Tucker according to equation (2.103) has been used. The relations for the dissipation integral, the heat transfer coefficient and for the roughness factor have been described in section 2.8. The most important results are presented in the figures 16 to 25 which are taken from Masee [Ma2]. The value of 150 V used for the total voltage drop ΔV in the figures 16 to 23 corresponds, in first approximation, with the values obtained in measurement series 2 of the EUT blow-down experiment. The figures 16 and 17 show the Mach number and the static pressure respectively as a function of the coordinate x along the flow direction. These figures have been included only for the sake of completeness since they are very similar to the corresponding figures in section 3.2. Just as in section 3.2 boundary layer separation is predicted to occur inside the generator at $R_L=4 \Omega$ (compare figure 21) which will lead to a shock wave. The displacement thickness at the electrode wall $\delta_{1,e}$

as a function of the coordinate x is shown in figure 18. It is seen here that $\delta_{1,e}$ increases when the MHD interaction increases (R_L decreases) which corresponds with expectations from physical reasoning. This phenomenon is therefore described correctly with the present model which thus avoids the main disadvantage of the simple model described in section 3.2.

The large and sudden drop in $\delta_{1,e}$ when the flow enters the supersonic diffuser is caused by the fact that the temperature overshoot parameter $\Delta Q/Q_0$ drops to zero at this location. This is a consequence of the behaviour of the electric current density which instantaneously goes to zero in a quasi-one-dimensional description as soon as the flow leaves the generator. In reality the three effects mentioned will be smeared out due to two-dimensional effects.

Since it is not necessary to calculate the stagnation enthalpy thickness $\delta_{H,e}$ outside the generator, figure 19 shows $\delta_{H,e}$ as a function of distance in the generator only. The fact that $\delta_{H,e}$ assumes negative values inside the MHD generator is due to the excess Joule dissipation in the boundary layer which is expressed by the parameter $\Delta Q/Q_0$ shown in figure 20. The additional Joule dissipation leads to an overshoot in the stagnation enthalpy profile (compare equation 2.85) which implies a negative value for $\delta_{H,e}$. Figures 19 and 20 both illustrate that this effect increases with increasing MHD interaction.

It has been mentioned already that the incompressible shape factor $\bar{H}_{12,e}$ indicates how close the electrode wall boundary layer is to separation. The variation of $\bar{H}_{12,e}$ with the coordinate x along the hot flow train is shown in figure 21. Because of the large positive gradient of $\bar{H}_{12,e}$ at $x=0.375$ m for $R_L=4 \Omega$ the separation criterion $\bar{H}_{12,e}=2$ will be reached in a short distance.

Figures 22 and 23 show two boundary layer thicknesses for the insulator wall namely $\delta_{1,i}$ and $\delta_{j,i}$ along the flow train and the generator respectively. The displacement thickness $\delta_{1,i}$ shows a behaviour contrary to $\delta_{1,e}$ namely $\delta_{1,i}$ decreases with increasing MHD interaction. This is caused by the decreasing Lorentz force when coming close to the insulator wall as discussed in section 2.1 which leads to the possibility of an overshoot of the velocity profile. The overshoot makes $\delta_{1,i}$ smaller and the effect increases

with growing MHD interaction. In the supersonic diffuser $\delta_{1,i}$ increases much faster than $\delta_{1,e}$ so that $\delta_{1,i}$ and $\delta_{1,e}$ are approximately equal at the end of this diffuser. The fact that $\delta_{j,i}$ increases as the MHD interaction decreases as shown in figure 23 can be explained from the fact that the eddy currents in the cross-sectional plane increase with increasing R_L (compare [Le1]). In order to investigate the sensitivity of the results to the value used for the voltage drop in the calculations, the figures 24 and 25 show $\delta_{1,e}$ and $\delta_{H,e}$ respectively at three values of ΔV . It is seen that the influence is rather large and since the MHD interaction increases as the voltage drop decreases, the effect is also that numerical difficulties are encountered at smaller values of x . The tendencies in the figures 24 and 25 can be explained almost completely through the influence of the parameter $\Delta Q/Q_0$ on $\delta_{1,e}$ and $\delta_{H,e}$. This will be clear since the parameter ΔQ is proportional to the additional Joule dissipation in the boundary layer which can be written as $j_y \Delta V$. The sensitivity of the results on the value of ΔV as shown in the figures 24 and 25 leads to the conclusion that an approximation of the actual ΔV profile by a constant value, as was done in the calculations presented in this section, can not lead in general to accurate results. Therefore the measured profile of the voltage drop will be used in the confrontation of theory and experiment in section 5.

It should be mentioned that the factor limiting the electric power produced by the generator is again the phenomenon of boundary layer separation at strong MHD interaction, just as in section 3.2. Therefore the present model also supports the conclusion that more electric power can be generated when the divergence of the MHD generator or when the inlet stagnation pressure is increased. No calculations have been performed for an MHD generator with a larger divergence. The influence of an increase in stagnation pressure has been verified by additional calculations. The results show that the boundary layer separation in the generator at $R_L=4 \Omega$ and $\Delta V=150 \text{ V}$ can be avoided when the stagnation pressure is increased from 7 to 10 bar. The maximum electrical power output of the generator can be increased in this way from 815 kW (at 7 bar, $R_L=6 \Omega$, corresponding with $\eta_{ent}=17.3\%$) to 1098 kW (at 10 bar, $R_L=4 \Omega$, corresponding with $\eta_{ent}=16.3\%$) according to the present model.

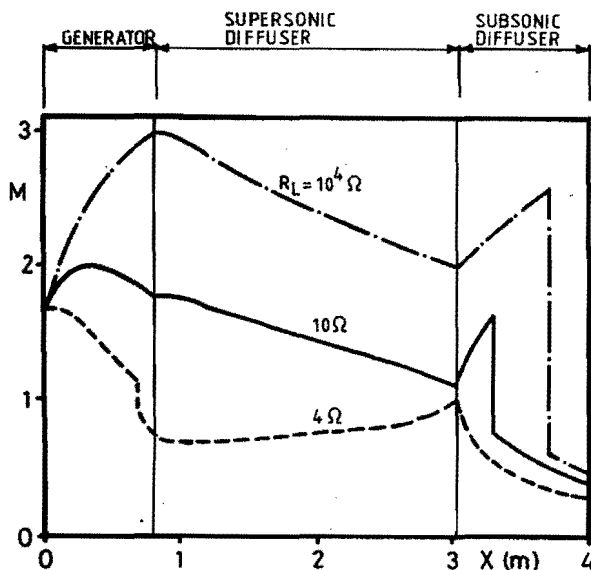


Fig. 8 Calculated Mach number distribution in the flow train; model 3.1.

Note that the flow chokes ($M = 1$ is reached) at $x = 3.03$ m and $R_L = 4 \Omega$.

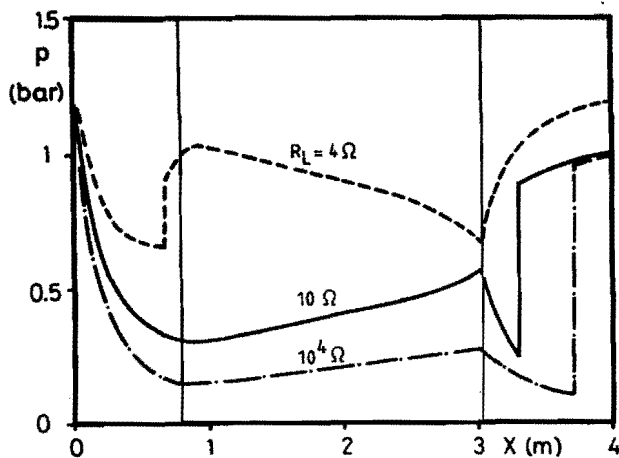


Fig. 9 Calculated static pressure distribution in the flow train; model 3.1.

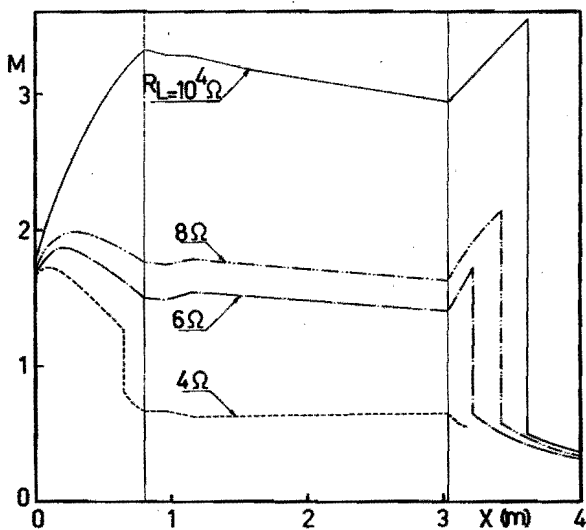


Fig. 10 Calculated Mach number M as a function of x in the flow train; model 3.2.

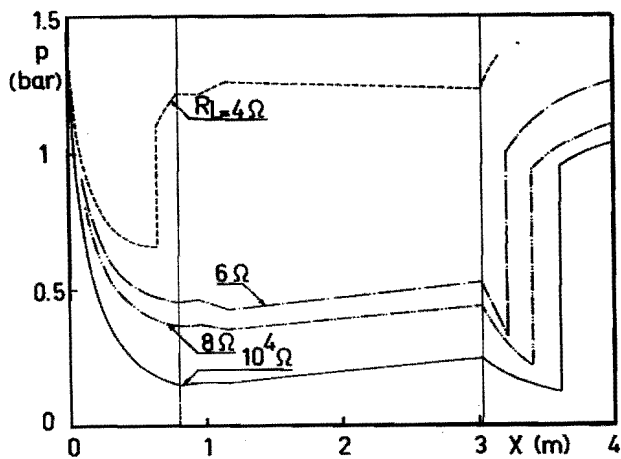


Fig. 11 Calculated static pressure distribution in the flow train; model 3.2.

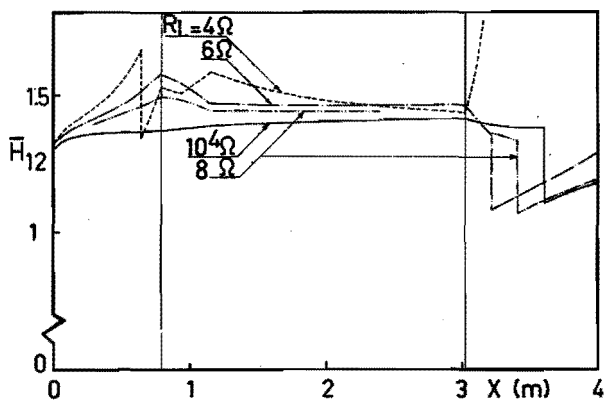


Fig. 12 Calculated incompressible shape factor \bar{H}_{12} as a function of x in the flow train; model 3.2.

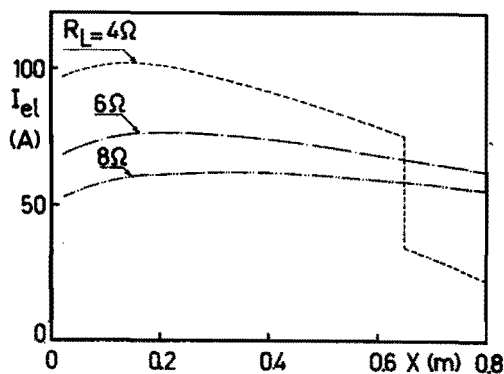


Fig. 13 Calculated current per electrode pair I_{el} as a function of x in the generator; model 3.2.

Note that the sudden change at $x = 0.65$ m is due to a normal shock wave.

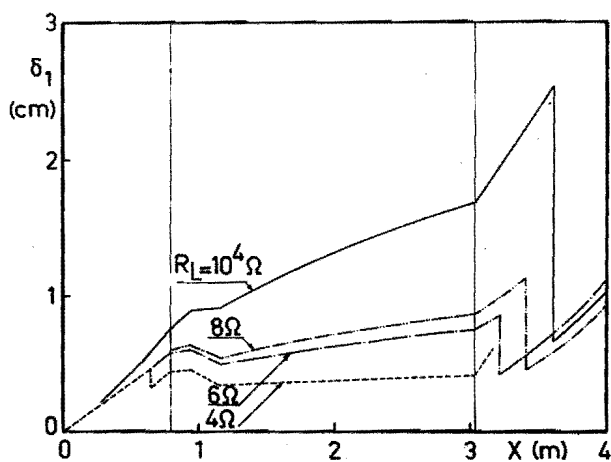


Fig. 14 Calculated displacement thickness δ_1 as a function of x in the flow train; model 3.2.

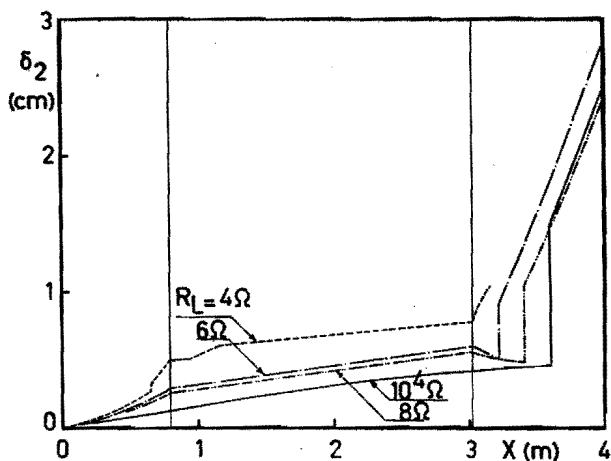


Fig. 15 Calculated momentum thickness δ_2 as a function of x in the flow train; model 3.2.

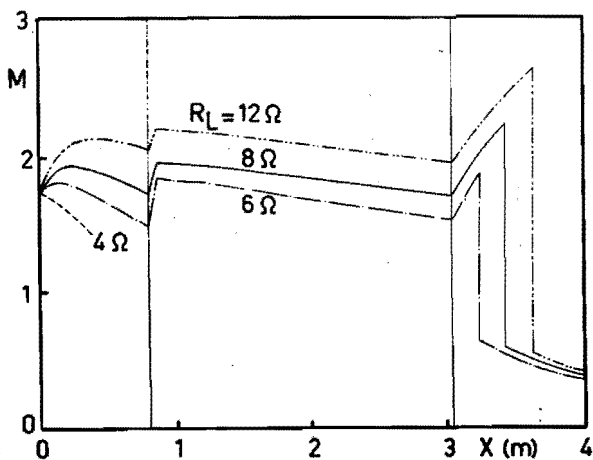


Fig. 16 Calculated Mach number distribution in the flow train at a value of the voltage drop of 150 V; model 3.3.

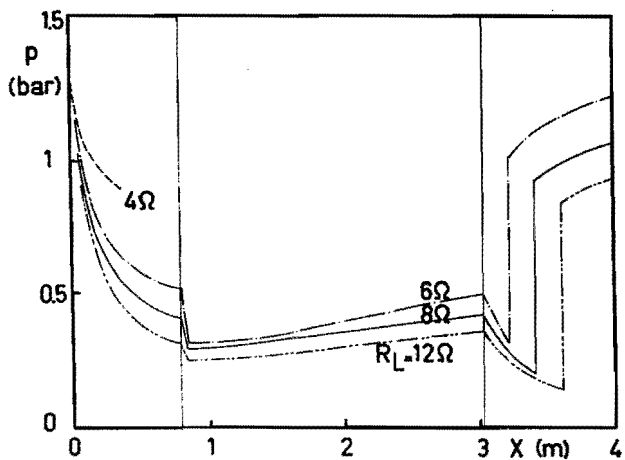


Fig. 17 Calculated static pressure distribution in the flow train at a value of the voltage drop of 150 V; model 3.3.

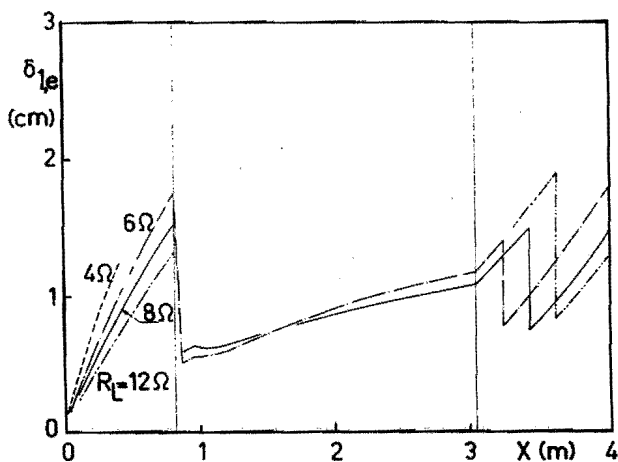


Fig. 18 Calculated displacement thickness at the electrode wall $\delta_{1,e}$ as a function of x in the flow train at a value of the voltage drop of 150 V; model 3.3.

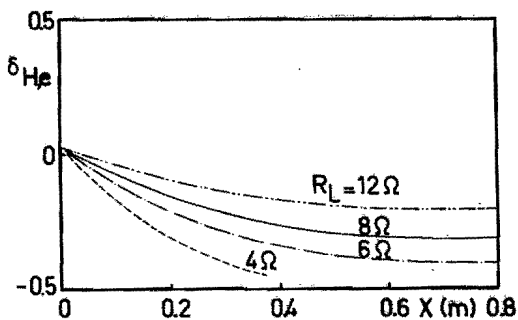


Fig. 19 Calculated enthalpy thickness at the electrode wall $\delta_{H,e}$ as a function of x in the generator at a value of the voltage drop of 150 V; model 3.3.

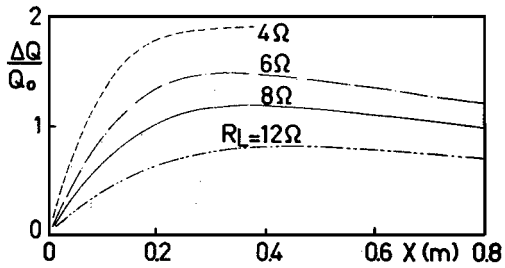


Fig. 20 Calculated distribution of the temperature overshoot parameter $\Delta Q/Q_0$ in the generator at a value of the voltage drop of 150 V; model 3.3.

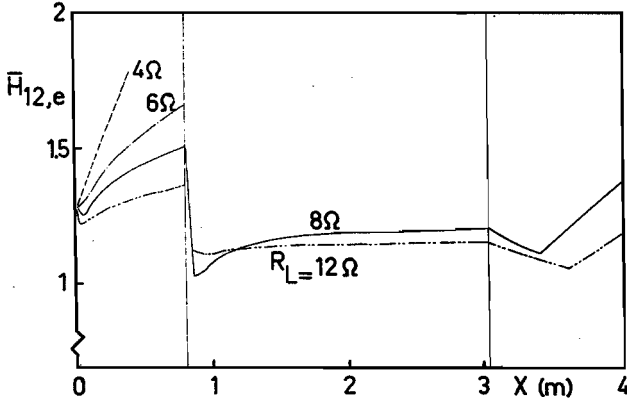


Fig. 21 Calculated incompressible shape factor at the electrode wall $\bar{H}_{12,e}$ as a function of x in the flow train at a value of the voltage drop of 150 V.; model 3.3.

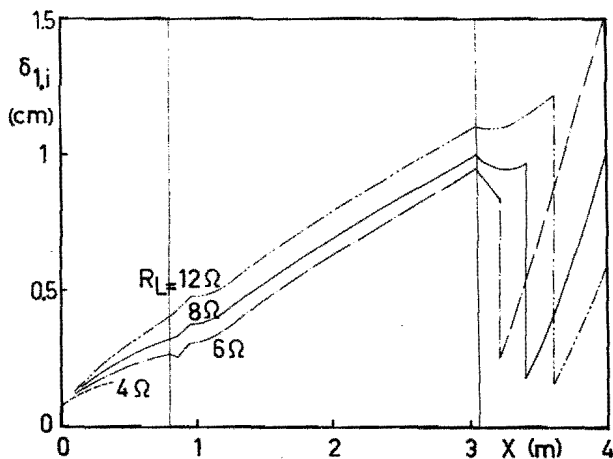


Fig. 22 Calculated displacement thickness at the insulator wall $\delta_{1,i}$ as a function of x in the flow train at a value of the voltage drop of 150 V; model 3.3.

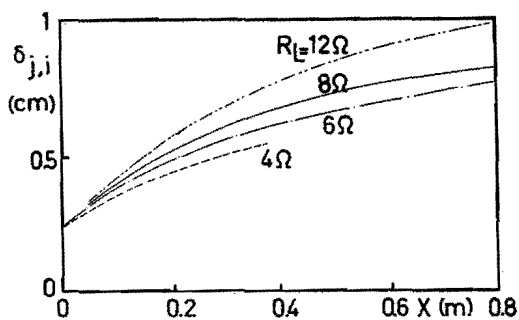


Fig. 23 Calculated current density displacement thickness at the insulator wall $\delta_{j,i}$ as a function of x in the generator at a value of the voltage drop of 150 V; model 3.3.

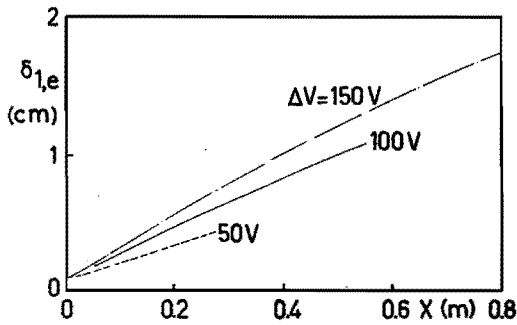


Fig. 24 Calculated displacement thickness at the electrode wall $\delta_{1,e}$ as a function of x in the generator at a value of the load resistance of 6Ω ; model 3.3.

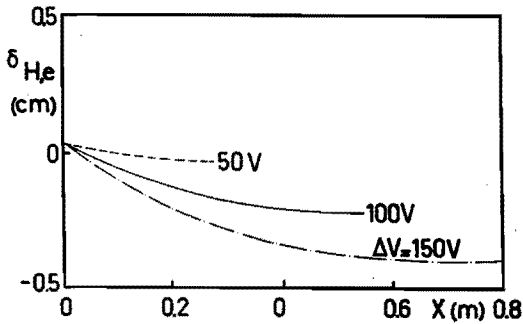


Fig. 25 Calculated enthalpy thickness at the electrode wall $\delta_{H,e}$ as a function of x in the generator at a value of the load resistance of 6Ω ; model 3.3.

4. Experimental results

4.1 Description of the experimental set up

The blow-down experiment at the Eindhoven University of Technology (EUT) has been set up with the goal to extend the test time from the EUT shock-tunnel experiment and to study the effect of a realistic heat source. The third difference with the shock-tunnel experiment is that the maximum magnetic field has been increased from 3.5 to 5.3 T in the blow-down experiment. Finally, the medium is exhausted into the atmosphere in the blow-down experiment so that a diffuser is needed downstream of the generator. In the shock-tunnel experiment the medium is exhausted into a vacuum tank. The blow-down experiment at the EUT will be described with the help of the line diagram shown in figure 26. The heat source is a ceramic brick regenerative heat exchanger fired by propane and air. The heat is stored in the bed of alumina cored bricks which is designed for an argon temperature of 2000 K at a mass flow of 5 kg/s (corresponding to a thermal input of 5 MWt) during 60 seconds. The heat exchanger is usually operated at a pressure of 7 bar but if needed the pressure can be increased to 10 bar (the mass flow and thermal input are then increased to 7 kg/s and 7 MWt respectively). Even at the pressure of 10 bar flotation of the bed will not be a problem. It was already demonstrated before by Cook [Cool] that this type of heat exchanger can deliver a hot noble gas with low molecular impurity levels. A closed cycle MHD experiment with this type of heat source has not been in operation, however, before the experiment at the EUT was started up. After the desired temperature profile in the alumina bed has been reached the vessel is evacuated by a vacuum pump protected by a cooler. The long term storage of argon is done in liquid form. Gaseous argon for one blow-down run is contained in a 4 m³ sphere at a pressure of 100 bar. A pressure control valve supplies the argon flow at the desired stagnation pressure to the heat source. The hot argon leaves the heat exchanger through a high temperature gate valve with an inner diameter of 10 inch and enters the cesium module.

In this module an aerosol of cesium droplets is injected by means of an ultrasonic atomizer. The injection system has been designed in such a way that the produced droplets are small enough to evaporate completely during the time needed to reach the entrance of the MHD generator. Moreover a homogeneous mixing must be provided by the injection system; the nominal seed ratio is 0.1% (volume ratio). The cesium module has been constructed with a molybdenum inner lining backed by saffil. A water cooled stainless steel nozzle limits the mass flow rate to the desired value of 5 kg/s at a stagnation pressure of 7 bar or 7 kg/s at 10 bar. The generator duct diverges from $0.05 \times 0.154 \text{ m}^2$ to $0.18 \times 0.154 \text{ m}^2$ over a length of 0.8 m. The Mach number is 1.7 at the inlet of the generator. The electrode walls are parallel and contain 32 pairs of protruding semi-cylindrical electrodes. The construction materials used for the inner walls and for the electrodes in the different generator channels are summarized in table II. Up to now the channel has always been used in the heat sink mode.

The argon cesium plasma flows from the generator through a stainless steel water-cooled supersonic and subsonic diffuser and exhausts into the scrubber tank and stack. In order to prevent a shorting of the generated Hall potential, which can increase to about 1500 V, the supersonic and subsonic diffuser, scrubber tank and stack are electrically insulated from ground.

The cryogenic magnet, cooled by liquid nitrogen, gives a maximum magnetic field of 5.3 T. The spatial homogeneity of the field in the relevant volume is $\pm 5\%$ and the variation with time around the maximum value is less than $\pm 5\%$ during a period of 11 s. During a 60 s excitation the temperature of the coils would rise from 77 to 170 K. This may partly explain the variation of the magnetic field with time which is shown in figure 27 together with the timing sequence of the stagnation pressure and the cesium injection. The argon flow, magnet current and the injection of cesium is automatically adjusted by means of a programmable logical controller. It should be noted that the timing sequence is analogous for all runs although small changes between runs have occurred. The data-acquisition system measures 208 channels during the heating phase of the heat exchanger, sampling each channel

every 10 seconds. During an experimental blow-down run the same number of channels is sampled at a repetition frequency of 4 Hz for each channel.

The electron temperature and density and the dust loading of the plasma are measured by means of optical diagnostics. The amount and type of the molecular impurities are determined by means of a mass spectrometer. The voltage distribution between anode and cathode is measured at two or three axial locations in the generator by a series of 5 potential probes, flush with the inside of the insulator wall. The static pressures are measured at four or five axial locations in the generator and at five or six locations in the diffusers. These locations have been collected in table III. Most of the pressure measurements have a slow time response but in the last series of experiments the pressure has been measured with a response up to 1 kHz at three locations by means of Kistler piezo resistive pressure transducers.

Part of the spectroscopic data, and in the last series of runs one of the high frequency pressure measurements, is recorded on magnetic tape with an analog bandwidth of 500 kHz (14 input channels). For the remaining spectroscopic data a multi-channel wave-form digitizer is used which is connected by means of a CAMAC interface to the computer. The remaining high frequency pressure measurements are recorded during 8 seconds by means of data loggers and then written to the disc memory of the computer during 2 seconds (during this time no data are taken in by the data loggers). The analog bandwidth of the data loggers equals 500 Hz. Figure 28 shows a lay out drawing of the facility in the lab. For completeness figure 29 shows the hot flow train and details of the first three electrodes in the generator channels of the different measurement series. Finally the construction of the pressure taps in the generator for the static pressure measurements, is drawn in figure 30.

4.2 Electrical behaviour of the generator

The most important parameters of all runs have been collected in table IV. For all measurement series the experiments had to be

terminated because of mechanical damage of the generator channel. Table IV shows that the maximum electric power generated up to now is 360 kW (run 303) which corresponds to an enthalpy extraction of 7%.

The electrical behaviour of the different runs will now be discussed first by means of table IV and figure 31. The latter shows the power output as a function of time for the most important runs. Run 201 served as a calibration run for the diagnostics under the influence of the magnetic induction. Therefore no cesium was injected. In run 202 the two anode cables of electrode pairs 16 and 30 were accidentally interchanged. As a consequence a reversed Hall voltage was observed between electrode pairs 16 and 24 but for the first time electric power was generated in the experiment. In run 203 the cesium injection system was unfortunately not connected electrically and no electric power was generated. Runs 204 and 205 thus gave the most interesting results of measurement series 2 and therefore the curves of the power output of these runs have been included in figure 31. The figure shows that there are large fluctuations in power output during these runs which may be attributed to the low level of cesium seeding. Apart from the fluctuations the curve of the power output for run 204 shows a strong similarity with the variation of the magnetic induction (compare figure 27). This could be expected beforehand from the principles of the operation of an MHD generator. A more precise comparison between theory and experiment on this aspect will be presented in chapter 5.

The observed relation between power output and magnetic induction is clearly not valid for the conditions of run 205. Here the power output is reduced by roughly a factor two from $t=37$ s to $t=42$ s as shown by figure 31. (This is confirmed by the high frequency resolved measurement of the light emission from the generator channel). $t=37$ s is the time when the magnetic induction reaches its maximum in this run. This behaviour may be attributed to gasdynamic phenomena leading to a shock wave in the generator as predicted by all three models in section 3. For a definite proof further experiments are required, particularly high frequency pressure measurements at strong MHD interaction under conditions

where Hall shorting is avoided.

In run 301 open circuit voltages have been measured. In this situation the medium in the generator is a recombining plasma with a limited number of free electrons and therefore a high internal resistance. Under these circumstances the resistive coupling of the electrodes to ground through the deionized and demineralized water cooling system plays an important role. Therefore the electrical results of run 301 are difficult to interpret and will not be discussed further. During the runs 302 and 303 the first four electrode pairs were short-circuited in order to produce some pre-ionization. The cesium seeding reached at least the design value of 0.1% during these runs (see table IV). These two facts are considered to explain the disappearance of the fluctuations in the power output of these runs as shown in figure 31. It should be noted that the pre-ionization did not decrease the relaxation length (compare figure 32) but it is expected to have contributed to a smooth creation of streamers in the inlet region of the generator. The magnet has been switched off during run 303 at $t=47$ s because of a Hall shorting to ground that occurred in the wiring. The latter fact may also explain the dip in the curve for the power output at about $t=33$ s.

During runs 401 and 402 almost no electric power was generated because of the large contamination with water vapor (see table IV). The latter was caused by a water leakage in the generator channel during shake down tests with the preheat loop. The water accumulated in the boron nitride of the generator walls. Drying the hot flow train with air of 393 K during 150 hours was apparently insufficient to remove the moisture. Because of the very poor performance during the runs 401 and 402 no power output curves have been included in figure 31.

During the runs 501 and 502 the loading of the generator was equal to the value in the runs 204 and 303 in order to compare with earlier results and to determine the influence of pre-ionization which was not used again. The power output was, however, on a much lower level than in the runs 204 and 303 and again showed large fluctuations during both runs as shown in figure 31 for run 502. The explanation for the low power level may be found in the

improper operation of the cesium injection system, caused by partial plugging of one of the main gas lines. This leads in general to much larger droplets. The resulting effect is a reduced amount of cesium in the vapor phase (the number mentioned in table IV is the total amount of liquid cesium which has been injected). Another effect of the larger droplets may have been the formation of cesium layers on the generator walls which can lead to partial shorting of the Hall field.

Further large contact resistances of the electrodes have been observed during the runs 501 and 502 which were caused by oxidation of the molybdenum and amounted to about 20 ohm. After disassembly of the generator after run 502 it was observed that the small number of streamers that had been present, had burned away the oxides over parts of the electrodes. This is apparently the explanation of the small increase in power output from run 501 to 502. It may therefore be expected that the oxides mainly impeded a continuous creation of streamers in the inlet region of the generator.

In the following the discussion will mainly concentrate on the phenomena during run 302 since this run did not experience any special difficulties. In connection with the fact that high frequency pressure measurements succeeded for the first time during measurement series 5, results from run 502 will be discussed also when it seems appropriate.

The behaviour of the electrode currents during run 302 are shown in figure 32. The curves in figure 32^a show the current per electrode pair as a function of distance in the generator and with time as a parameter. Curve 1 at $t=34$ s shows that the relaxation length is very large at a moment when the power production has just started. The relaxation length decreases when the magnetic induction increases. Curve 3 at $t=39.25$ s shows the situation at maximum electric power output. It is interesting to observe when going from $t=35$ to $t=39.25$ s that the currents increase substantially in most parts of the generator but do not vary much for x larger than 0.6 m. This is also apparent from the other curves in figure 32 which show typical electrode currents at a fixed location as a function

of time. Comparing the curve for the current at electrode pair 20 with the shape of the magnetic induction in figure 27 it is clear that there is a strong coupling as expected. Figure 32 shows that this is no longer true for electrode pairs which are located far downstream in the generator. The current at electrode pair 32 even shows a local minimum at a time of about 50 s and then starts increasing in a period of time when the magnetic induction decreases. An explanation of the behaviour of the electrode currents shown in figure 32 can be found in a partial shorting of the Hall voltage for instance through hot boundary layers for values of x beyond 0.5 m. This suggestion can, however, only be verified in special experiments since there is no reliable theoretical model available that can predict the Hall field. As mentioned before it appears from figure 32^a that the pre-ionization in run 302, which is shown as the very large current peak at electrode pair 4, does not lead to the vanishing of relaxation phenomena.

The Hall potential as a function of x for run 302 is shown in figure 33^a. The remaining curves in figure 33 show the Hall potential difference for parts of the generator as a function of time. The figures 33^c and 33^d show a behaviour of V_8V_{16} and $V_{16}V_{24}$ which has a strong similarity with the variation in time of the magnetic induction. Figure 33^e shows a similar saturation of $V_{24}V_{32}$ as observed in the behaviour of the electrode currents downstream of electrode pair 20. The fact that V_1V_8 shows a time behaviour which is different from that of the Hall potential difference over other parts of the generator may be related to relaxation phenomena in the first part of the generator. Another special feature in the behaviour of V_1V_8 is found in the shape of the curves in figure 33^a. At $t=33$ s the electrical power generation has just started (compare figure 31) and at $t=39.25$ s the maximum power output has been reached. These curves clearly show that at t larger than 36 s all parts of the generator behave in a similar way as far as the Hall potential is concerned. At $t=33$ s, however, when the power output amounts to only 8.5 kW the major part of the total Hall potential is built up over the first quarter of the generator and

the Hall field is even reversed in the last quarter of the generator.

The situation at $t=33$ s in figure 33^a shows apparently the usual behaviour when the power output has just started up. This is confirmed by figure 34^a where curve 1 also denotes a situation just after the beginning of power output during run 502. Here the special behaviour is even more pronounced because the Hall field is reversed in the entire downstream half of the generator. The behaviour in the figures 33^a and 34^a just before or shortly after the power output has started up can be explained from the fact that the medium in the generator is then largely a recombining plasma with a high internal resistance. The reversal of the Hall field in that case can be explained through the influence of the resistive coupling of the electrodes to ground which still plays an important role in these conditions.

Curve 3 in figure 34^a corresponds with the situation where the maximum total Hall potential is built up. Its shape is similar to that of curve 3 in figure 33^a but the total Hall potential for run 502 is only about 60% of the value for run 302. The other curves in figure 34 show the Hall potential difference for parts of the generator as a function of time during run 502. The time behaviour of $V_1 V_8$ for the runs 502 and 302 is more or less similar. A comparison of the figures 34 and 31 (run 502) shows that the time behaviour of $V_{16} V_{24}$ and $V_{24} V_{32}$ has a strong similarity with the curve of the power output. The curve is, however, superposed on a peculiar time behaviour which causes negative values. Figure 34^c shows that the curve of $V_8 V_{16}$ is exceptional and has little resemblance with the time behaviour of the power output. It should be stressed that the strange time behaviour shown in the figures 34^b to 34^e has appeared for the first time during measurement series 5. Even with the large fluctuations in electrical properties during run 204 the time behaviour of $V_8 V_{16}$, $V_{16} V_{24}$ and $V_{24} V_{32}$ has a strong coupling with the variation of the magnetic induction as a function of time. It is therefore expected that the exceptional behaviour of the Hall potential during run 502 has been caused by the large contact resistances of the electrodes or possibly by cesium layers on the generator walls which partially shorted the Hall fields.

4.3 Gasdynamical behaviour of the hot flow train

The discussion of the gasdynamical results starts with figure 35. It shows the strong coupling between electrical and gasdynamical behaviour on a low frequency scale for the runs 302 and 502. Figure 35^a shows the connection between power output and magnetic induction as a function of time during run 302. Figure 35^b shows that the power output is also strongly related with the number of streamers, which is measured optically by means of two particle recombination radiation in the middle of the generator (see [F12]). As mentioned before the complicated filamentary structure in which the electric current flows in closed cycle MHD generators has been called streamer. These structures have been studied by means of optical diagnostics in the EUT blow-down experiment by Flinsenbergh [F11]. He has also constructed a model to describe the development of streamers in the generator. This model shows that in general the number of streamers at the 17th electrode pair presented in the figures 35^b and 35^e is proportional to the electric current at the same electrode pair. Finally figure 35^c shows that the static pressure in the downstream part of the generator is also strongly coupled with the number of streamers and with the power output. The figures 35^d to 35^f show similar relations for run 502. The power output during run 502 does not follow the shape of the magnetic induction curve but there is again a strong coupling between power output, number of streamers and static pressure in the downstream part of the generator. The difference in static pressure before and after power production in run 502 is caused by the loss of the last boron nitride plate in the side-wall which is located very close to the pressure measuring tap.

Figure 36 shows several pressures at various locations in the hot flow train as a function of time during run 502. The pressure p_{g1} is a static pressure which is measured about 25 cm upstream of the nozzle throat. The Mach number at this location equals about 0.15 so that p_{g1} is approximately equal to the stagnation pressure. The curves for the other static pressures in the hot flow train

presented in figure 36 all show the starting up of the supersonic flow when p_{g1} increases and an increase from their low gasdynamic values when the MHD interaction begins (compare figure 31). The location of the pressure taps in the hot flow train has been collected in table III. The curves for p_{g3} and p_{g5} show that the MHD effect on the static pressures in the generator increases with increasing values of the coordinate x . The curves for p_{g3} , p_{g5} , p_{d3} and p_{d7} in figure 36 show that the generator channel and the supersonic diffuser are protected between runs with an argon atmosphere at a pressure of about 1.1 bar.

The pressure p_{d9} is measured immediately downstream of the ball valve in the diverging subsonic diffuser. The fact that the perturbation in p_{d9} due to the MHD interaction does not resemble the curve of the power output in figure 31 may be attributed to the divergence of the channel at the measurement location.

The variation of static pressure with the coordinate x is shown in figure 37. The situation in the MHD generator under gasdynamical conditions (before the MHD interaction has started up) is shown in figure 37^a for the channels of the different measurement series. This figure shows a rather large difference between the various pressure profiles which can be explained from constructional details. Figure 37^a shows only a difference in static pressures between the channels of measurement series 2 and 3 at the first measuring location ($x=3.8$ cm situated in the second electrode). Considering figure 29 this discrepancy may be attributed to the different way of connecting the end of the supersonic nozzle contour to the inlet of the generator at the first electrode pair. In measurement series 2 the expansion wave originating from the step at $x=0$ is expected to influence the pressure measurement in the second electrode, thus leading to the smaller value shown in figure 37^a.

Figure 30^a shows the construction of the pressure measurement in the generator channel of series 2 and 3 through holes in the electrodes. Huijgen [Hul] has estimated the measuring error which results if the hole is not perfectly situated in the center of the electrode. Although this error may put a limit upon this way of

determining static pressures, the measurement of static pressures through the electrodes is far more reliable than the method used in measurement series 4 and 5. Figure 30^b shows the construction of the pressure measurements in the side-wall of the generator channel of series 4 and 5. Here the pressure transducer is connected to the static pressure inside the generator channel by means of a small tube passing through the layered wall. Since gaps have to exist between the layers and between the alumina tube and the boron nitride plate to allow for different thermal expansions, small flows through the gaps behind the inner wall will give some short-circuiting effect on the pressure measurement. As a consequence the pressure measurement in the series 4 channel systematically yields values which are too high as shown in figure 37^a. (It has been checked that the slightly different electrode shape in series 4 and 5 shown in figure 29 has only a marginal influence on the static pressure profile).

The static pressure measurements in a gasdynamical situation for the series 5 channel (which is in principle identical to the series 4 channel) are indicated as points in figure 37^a. These points show that it is difficult to reproduce earlier results when the pressure is measured through the side-wall. For constructional reasons the alumina tube passing through the wall (see figure 30^b) has not been present at the locations where a high frequency piezo resistive pressure transducer has been installed in measurement series 4 and 5. As a consequence a large measuring error will result at these locations which is shown clearly by the points of series 5 for p_{g3} ($x=28.8$ cm) and p_{g5} ($x=79.4$ cm), since the other points of series 5 are rather close to the line of measurement series 3.

The variation of static pressure with the coordinate x through the complete hot flow train is shown in the figures 37^b and 37^c for the runs 302 and 502 respectively. The pressure profiles for the two runs are qualitatively comparable. Especially the strong increase of the static pressure in the downstream part of the generator when the MHD interaction is present is noticeable. This pressure increase moves further upstream in the generator as the MHD interaction increases. It is clear that electrical power extraction is not the only explanation of this phenomenon since it is already

present at low power levels (compare figure 37^c). The presence of Hall currents through the hot electrode wall boundary layer in the downstream part of the generator is expected to contribute also to the strong increase of static pressure in this part of the generator. Concentrating now upon the profile of static pressure in the constant area supersonic diffuser a special phenomenon can be observed as shown for instance by the curve for $t=44$ s in figure 37^c. According to a one-dimensional model a decreasing pressure in a slowly converging channel (since the boundary layer thicknesses will in general increase) implies subsonic flow. Similarly a pressure increase in a slightly convergent channel indicates supersonic flow. From these statements it is clear that the pressure profile observed between $x=1.45$ m and 3.04 m can not be explained by a simple one-dimensional model. The explanation of the observed pressure variation at $t=44$ s in run 502 appears to be the presence of a system of oblique shocks in the supersonic diffuser. These shocks reflect from the walls and interfere with each other. A similar pressure profile in the supersonic diffuser was observed during run 205.

Some results of the fast response measurement of the pressure p_{d5} (in the supersonic diffuser at $x=144.5$ cm), which has been stored on a tape recorder, are shown in figure 38. The variation of p_{d5} during the time that the flow is supersonic, is shown in figure 38^a. This picture shows that fluctuations are absent when there is no MHD interaction. During the time that electric power is generated the amplitude of the pressure fluctuations is very large and is coupled to fluctuations in power output (as will be shown later). The picture in figure 38^a can be compared very well with the curves in figure 36. It shows that the amplitudes of the high frequency variations are distinctly larger than those in the low frequency curve. In figure 38^b the same pressure fluctuation is shown with an improved time resolution for a time period around the maximum in figure 38^a. A determination of the frequency spectrum of the pressure fluctuations by means of correlation techniques has shown that the largest amplitudes are found in the frequency range below 100 Hz. The characteristic time of the pressure fluctuations

is therefore one order of magnitude larger than the transit time of the flow through the generator which is of the order of 1 ms. The strong coupling between electrical and flow phenomena is also observed in the high frequency regime as shown clearly in figure 38^c. Here the lower oscilloscope trace shows the passing of three separate streamers as determined from the two particle recombination radiation signal measured in the middle of the MHD generator. The upper trace shows the response of the pressure p_{d5} to the passing of the streamers as two pressure bumps. The fact that the pressure p_{d5} reacts to an apparently small change in electric power may be attributed to a shifting of the system of oblique shocks in the supersonic diffuser. It is observed in figure 38^c that a certain time lag exists between the two signals corresponding to the time required by the flow to cover the distance between the measuring locations. Further the upper trace gives some indication of the time response of the piezo resistive pressure transducer which appears to be of the order of 2 ms. The strong coupling between electrical and flow phenomena can also be determined in a quantitative way by means of correlation techniques (see for instance Hellebrekers [Hel]). This appears from the figures 38^d and 38^e where the cross correlation between the pressure p_{d5} and the current through electrode pair 17 is shown. The value of the cross correlation coefficient for the large peak is equal to 0.43. Figure 38^e shows the cross correlation picture with an enlarged horizontal scale of 1 ms per division. From the latter picture the time lag between the signals of I_{17} and p_{d5} can be determined more accurately. The time lag for the large peak appears to be equal to 2.5 ms but this is in general much larger than the time required by the flow to cover the distance between the two measuring locations. This is caused by the response time of the pressure transducer which has been estimated above to be of the order of 2 ms. Because of this response time no conclusions can be drawn from phenomena with a time shift less than 2 ms (such as the smaller of the extreme values in figure 38^e at a time shift of about 0.7 ms). The determination of the correlation curve in the figures 38^d and 38^e has taken a real time of about 10 s starting at

$t=41$ s in run 502 so that it is an average over a range of electrical conditions.

Information on the behaviour of voltage drops as a function of time is shown in figure 39 for the electrode pairs 19 and 29 during run 302. The curve of the total voltage drop at electrode pair 19 shows a strong similarity with the shape of the magnetic induction and with the curve of the current at electrode pair 20 as a function of time (compare figure 32^b). The total voltage drop at electrode pair 29 seems also to have some relation with the behaviour of the current at electrode pair 28 (figure 32^d). Figure 39 shows that the anode and cathode voltage drop at electrode pair 19 do not differ much over the time period of electrical power production. The results at electrode pair 29, however, show a distinct and permanent asymmetry in the distribution of the voltage drop over the anode and cathode wall. A possible explanation of this phenomenon can be a partial shorting of the Hall field through the hot boundary layer at values of x larger than 50 cm.

The presence of Hall currents in the boundary layers leads to additional Joule dissipation and also to a vertical component of the Lorentz force. The latter effect results in an asymmetry and implies that the boundary layer thickness is larger at the cathode than at the anode wall. This also leads to the phenomenon that boundary layer separation occurs earlier at the cathode than at the anode wall. This kind of reasoning is also seen in early papers on open cycle MHD generators (see for instance Doss [Do2]). A more detailed analysis in a recent paper by Demetriades [De2], however, shows that the vertical component of the Lorentz force may create secondary flow cells and thus may lead to three-dimensional flow phenomena. The analysis shows that these three-dimensional effects lead to a reversed asymmetry between anode and cathode wall. (The analysis has been set up for open cycle conditions only).

Demetriades shows that the anode wall will experience separation earlier than the cathode wall due to the three-dimensional flow patterns. According to this analysis the voltage drop will then also be larger at the anode than at the cathode wall.

The asymmetrical distribution of voltage drops over anode and

cathode wall shown in figure 39 for electrode pair 29 is thus in agreement with the analysis of Demetriades. It is not clear if this fact indicates that three-dimensional flow phenomena have been important also in the experiments with the EUT blow-down facility up to now.

During measurement series 5 the voltage drop has been determined at three different axial locations. The results for run 502 have not been included here since they seem unreliable. This can be explained from the fact that measurement series 5 has been troubled by contact resistances of the electrodes and probably by cesium layers at the walls as has been mentioned before.

Table II Survey of construction materials for the generator channels tested in the different measurement series.

Series	channel design	material of inner wall	electrode material
2	EUT	boron nitride	stainless steel
3	EUT	silicon nitride	stainless steel
4	GE	boron nitride	molybdenum
5	GE	boron nitride	molybdenum

Table III Position of pressure taps in the hot flow train during the different measurement series (see figure 29 for the dimensions of the generator and the diffusers).

Indication of pressure tap	Location x (mm)		
	Series 2 and 3	Series 4	Series 5
p _{g1}	-340	-340	-340
p _{g2}	38	38	38
p _{g3}	213	288	288
p _{g4}	388	563	563
p _{g5}	563	794	794
p _{g6}	738	-	-
p _{d3}	934	934	934
p _{d5}	1445	1445	1445
p _{d7}	2365	2365	2365
p _{d8}	-	-	3038
p _{d9}	3100	3100	3100
p _{d11}	3931	3931	3931

Measurement series	Run	T _s (K)	p _s (bar)	mass flow (kg/s)	B _{max} (T)	R _L (ohm)	Cs (%)	P _{th} (kW)	P _e max (kW)	η _{ent} (%)	H ₂ O (ppm)	N ₂ (ppm)
2 (spring 1981)	201	1900	7.3	5.1	5.2	-	-	5030	-	-	-	-
	202	1900	7.2	5.0	5.2	6	0.05	4930	190	3.9	-	-
	203	1910	7.1	4.9	5.1	6	-	4860	-	-	40	1200
	204	1870	7.2	5.0	5.3	6	0.04	4850	270	5.6	60	25
	205	1910	7.2	5.0	5.3	4	0.05	4960	286	5.8	60	60
3 (fall 1981)	301	1900	7.4	5.1	5.25	-	0.09	5030	-	-	-	-
	302	1910	7.4	5.2	4.7	9	0.10	5155	230	4.5	50	80
	303	1900	7.4	5.1	5.1	6	0.14	5030	362	7.1	50	200
4 (summer 1982)	401*	1910	7.1	4.9	4.9	6	0.13	4860	.8	-	> 3500	> 2000
	402*	1910	7.0	4.9	5.0	6	0.15	4800	.7	-	> 3500	-
5 (spring 1983)	501	1890	7.4	5.1	5.0	6	0.12	5010	20	0.4	<100	200
	502	1960	7.4	5.0	5.2	6	0.12	5120	56	1.1	<100	200
* Runs carried out under the agreement between the United States of America and the Netherlands in the field of Magnetohydrodynamic Electrical Power Generation.												

Table IV Typical data for the various runs.

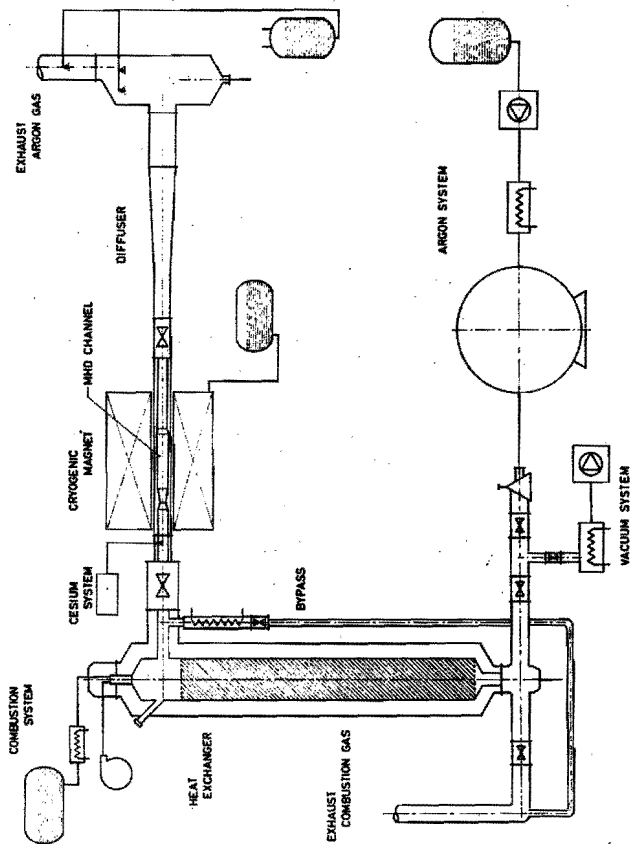


Fig. 26 Line diagram of the EIT blow-down facility.

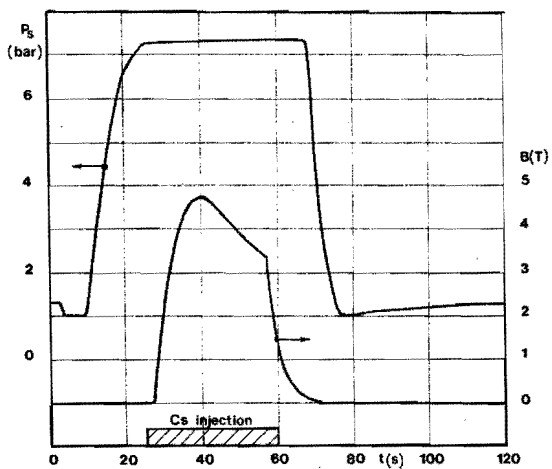


Fig. 27 Timing sequence for stagnation pressure p_s , magnetic induction B and cesium injection during run 502.

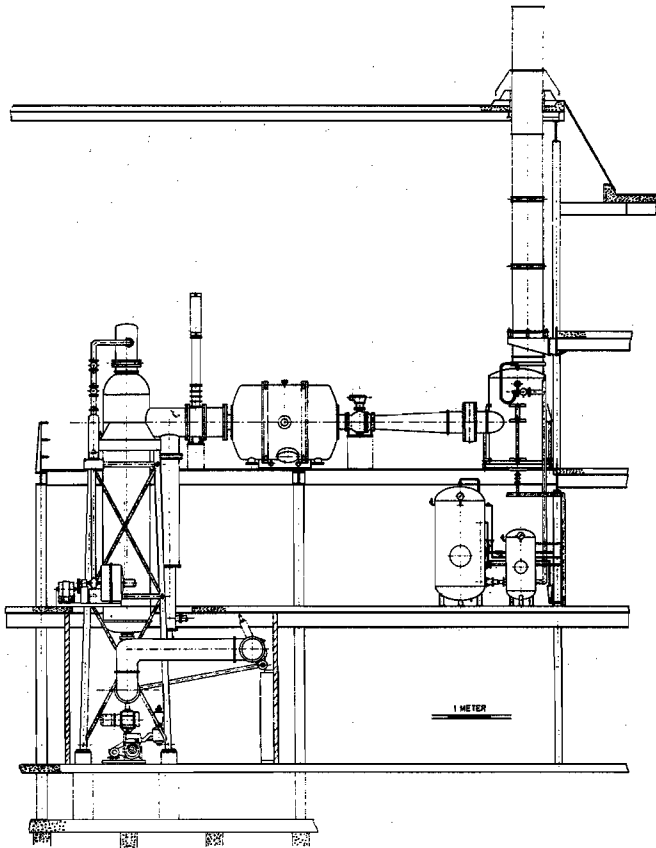


Fig. 28 Layout drawing of the EUT blow-down facility

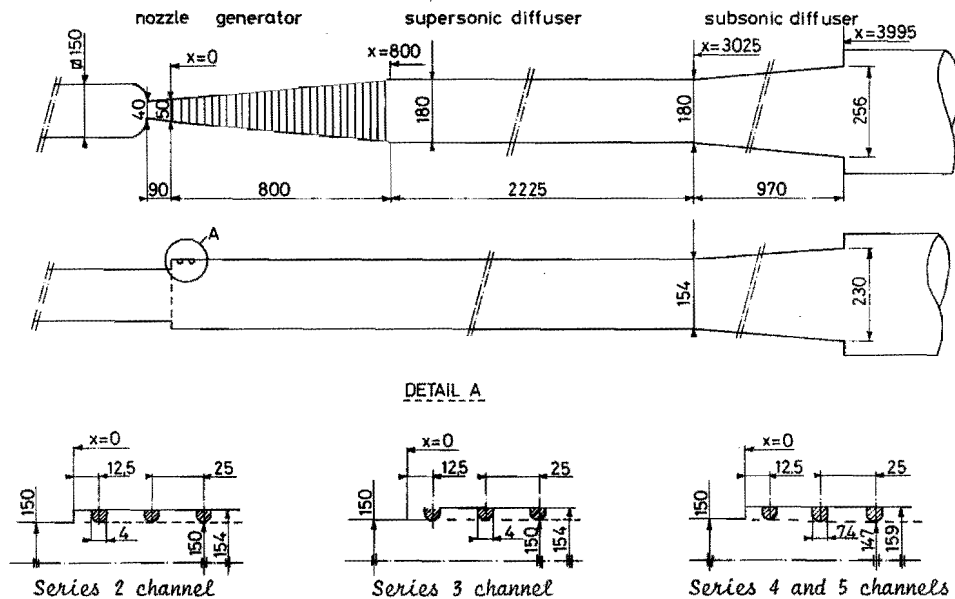


Fig. 29 Hot flow train and constructional details of the electrode wall at the generator inlet of channels of different measurement series.
Note that the dimensions are given in mm.

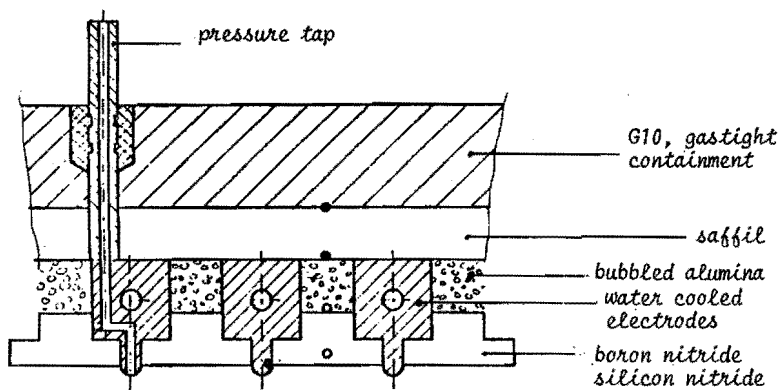


Fig. 30^a Construction of pressure taps in the upper wall of generator channels of measurement series 2 and 3.

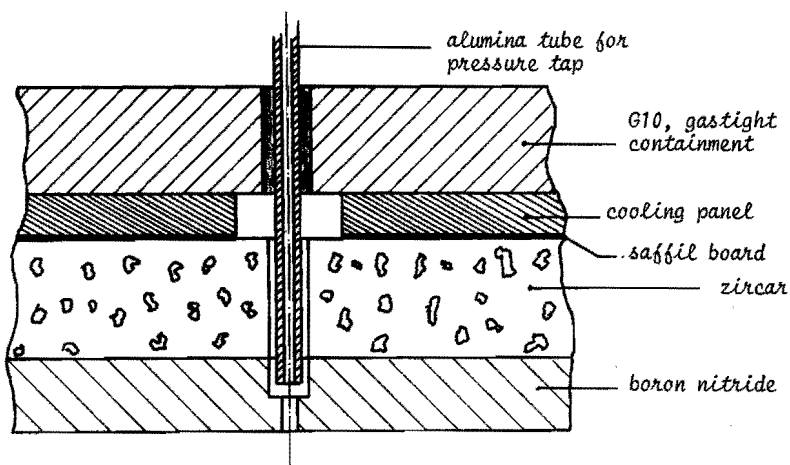
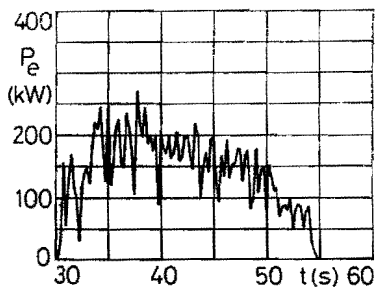
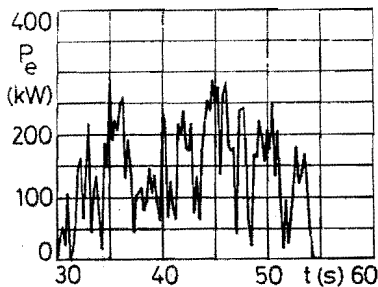


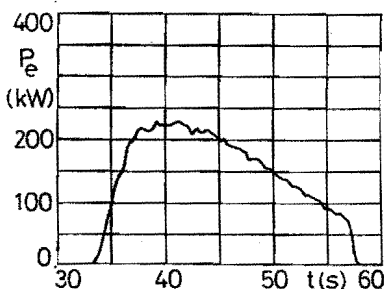
Fig. 30^b Construction of pressure taps in the side-wall of generator channels of measurement series 4 and 5.



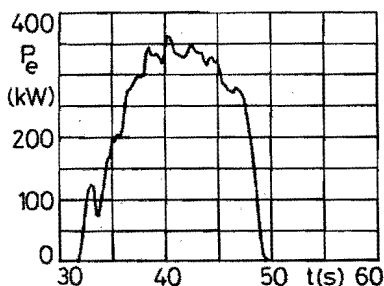
a) run 204, $R_L = 6 \Omega$



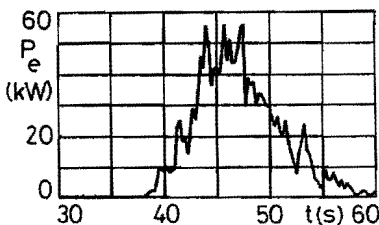
b) run 205, $R_L = 4 \Omega$



c) run 302, $R_L = 9 \Omega$

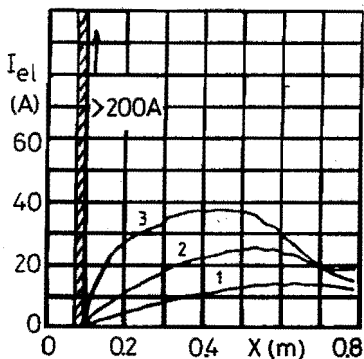


d) run 303, $R_L = 6 \Omega$



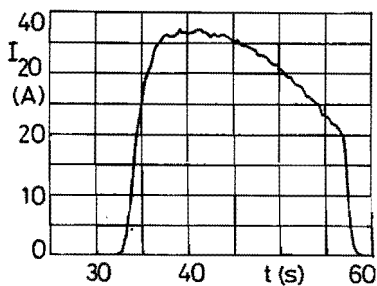
e) run 502, $R_L = 6 \Omega$

Fig. 31 Electrical power output P_e as a function of time for the most important runs. (Note the different vertical scale for run 502 and small changes in the timing sequence for the different runs).

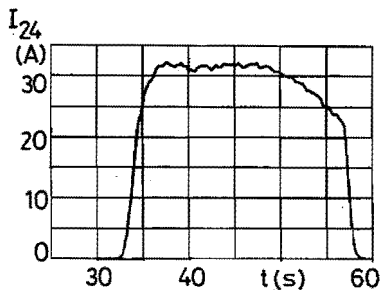


a) Current per electrode pair as a function of distance in the generator.

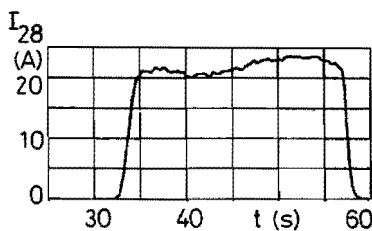
- | | | |
|---|-----------------------|--------------------------|
| 1 | $t = 34 \text{ s}$ | , $P_e = 29 \text{ kW}$ |
| 2 | $t = 35 \text{ s}$ | , $P_e = 97 \text{ kW}$ |
| 3 | $t = 39.25 \text{ s}$ | , $P_e = 229 \text{ kW}$ |



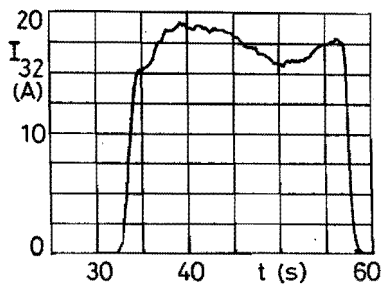
b) Current at electrode pair 20



c) Current at electrode pair 24

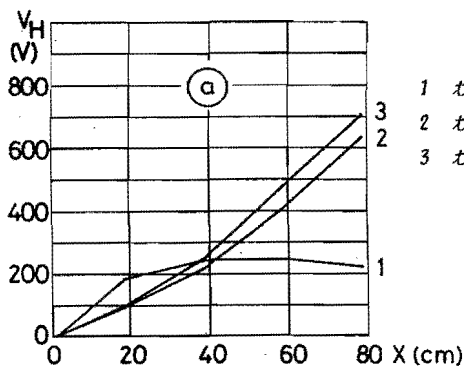


d) Current at electrode pair 28.



e) Current at electrode pair 32.

Fig. 32 Current per electrode pair as a function of distance in the generator (a) and at fixed locations as a function of time (b to e). Run 302.



- 1 $t = 33 \text{ s}$
- 2 $t = 36.5 \text{ s}$
- 3 $t = 39.25 \text{ s}$

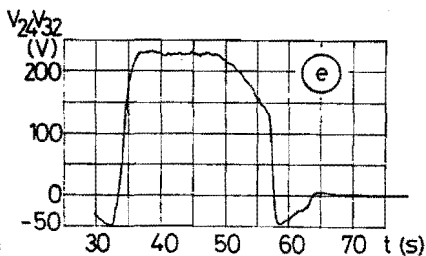
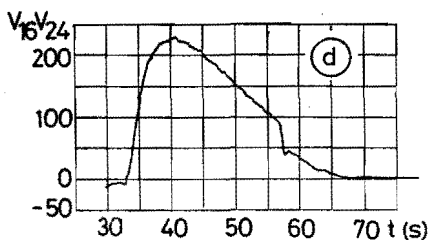
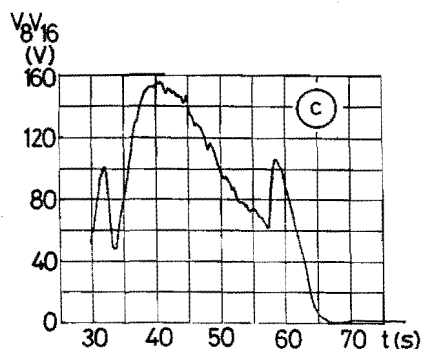
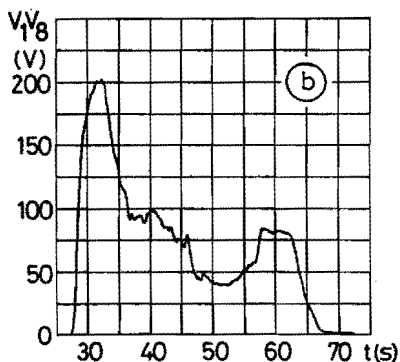


Fig. 33 Local Hall potential V_H as a function of distance in the generator (a) and Hall potential difference for parts of the generator as a function of time (b to e). $V_k V_l$ denotes the potential difference between electrodes k and l . Run 302.

Note that electric power is generated from 33 to 57 s.

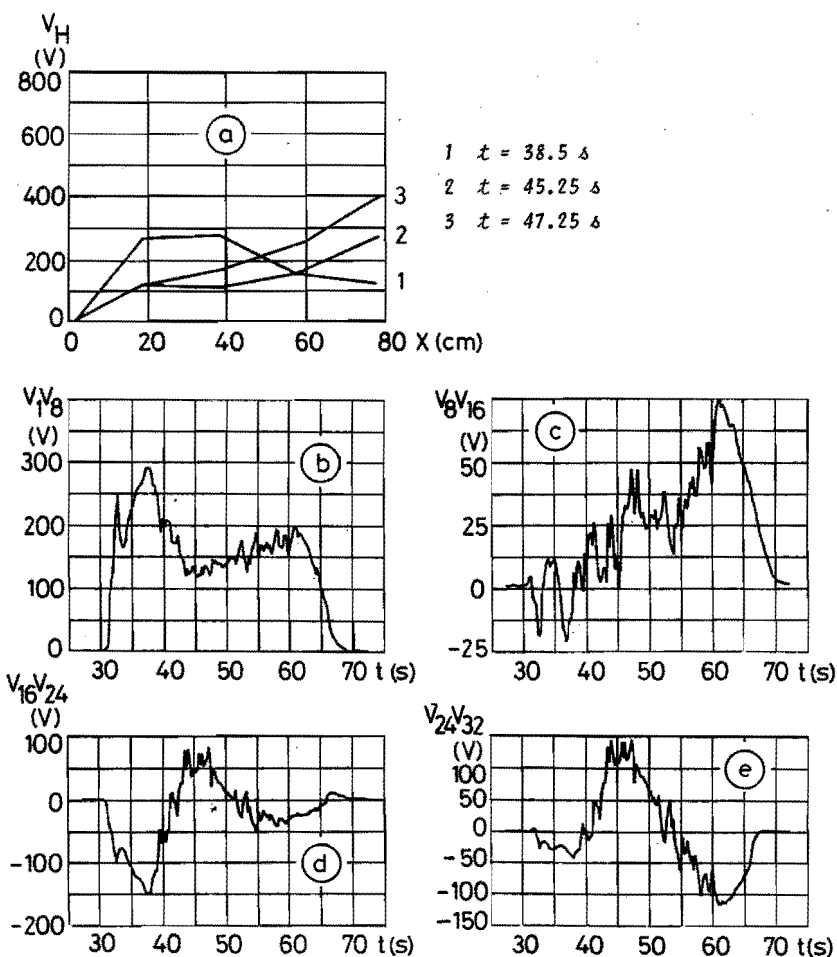


Fig. 34 Local Hall potential V_H as a function of distance in the generator (a) and Hall potential difference for parts of the generator as a function of time (b to e). V_{kl} denotes the potential difference between electrodes k and l . Run 502.
Note that electric power is generated from 38 to 61 s.

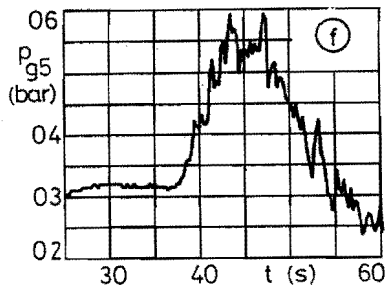
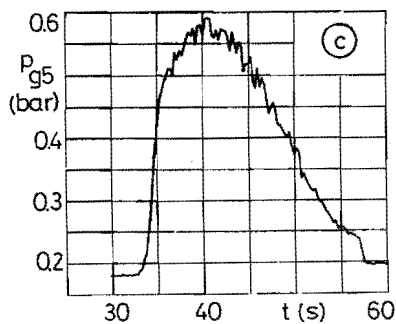
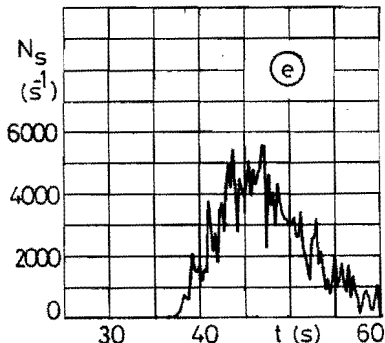
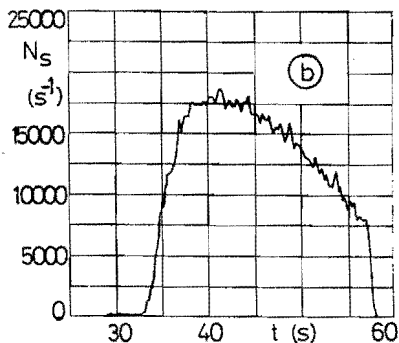
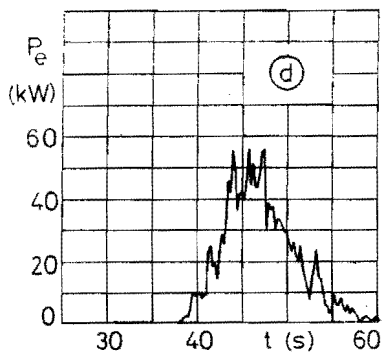
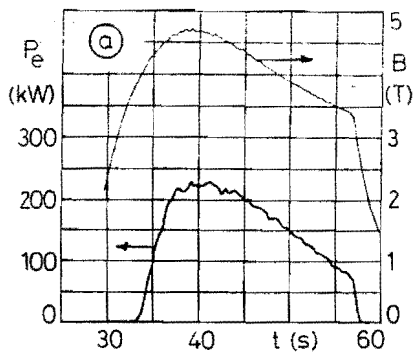


Fig. 35 Power output P_e and magnetic induction B (a), number of streamers N_s at the 17th electrode pair (b) and pressure p_{g5} (c) for run 302; power output P_e (d), number of streamers N_s (e) and pressure p_{g5} (f) for run 502; all parameters as a function of time.

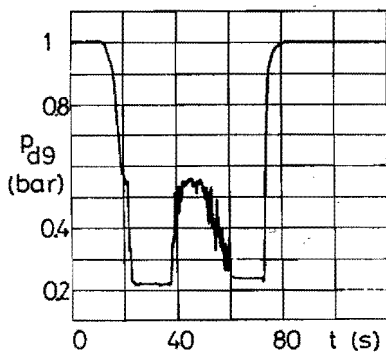
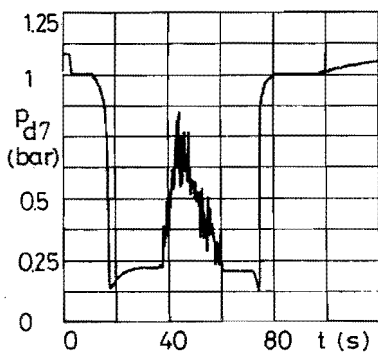
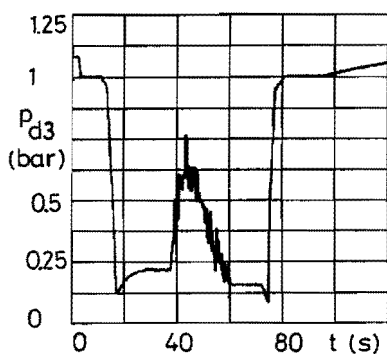
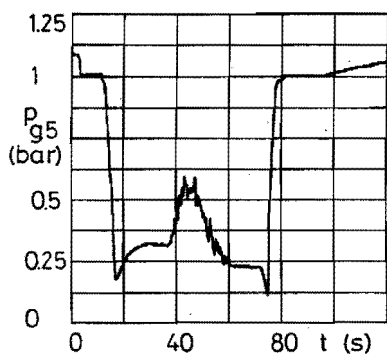
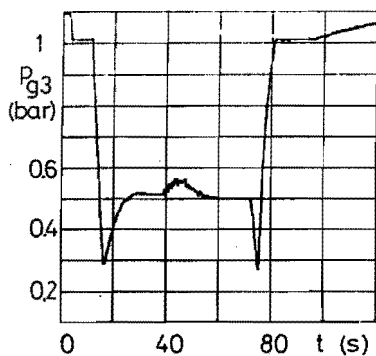
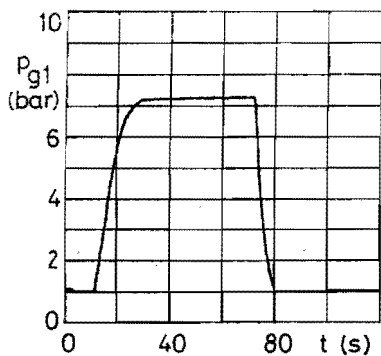
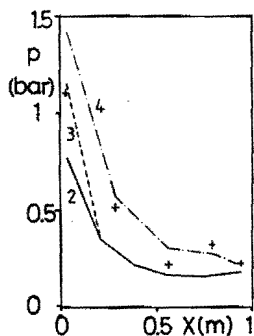
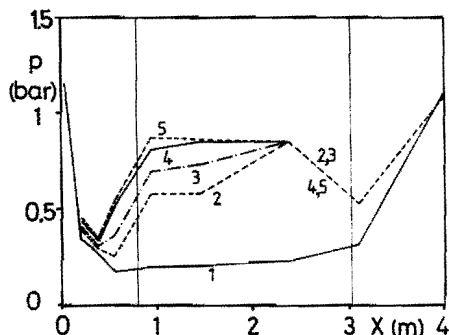


Fig. 36 Static pressure measured at different locations in the hot flow train as a function of time; run 502.

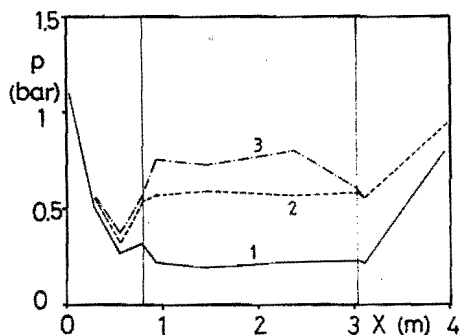


a) Static pressure under gasdynamic conditions for different measurement series (as indicated by the number; + denotes series 5).



b) Static pressure for run 302.

- 1 $t = 30 \text{ s}$, $P_e = 0$
- 2 $t = 55 \text{ s}$, $P_e = 91 \text{ kW}$
- 3 $t = 50 \text{ s}$, $P_e = 150 \text{ kW}$
- 4 $t = 45 \text{ s}$, $P_e = 200 \text{ kW}$
- 5 $t = 39.25 \text{ s}$, $P_e = 229 \text{ kW}$



c) Static pressure for run 502.

- 1 $t = 30 \text{ s}$, $P_e = 0$
- 2 $t = 42.5 \text{ s}$, $P_e = 23 \text{ kW}$
- 3 $t = 44 \text{ s}$, $P_e = 55 \text{ kW}$

Fig. 37 Static pressure as a function of distance; (a) in the generator under gasdynamic conditions, (b) and (c) through the hot flow train at different values of the MHD interaction.

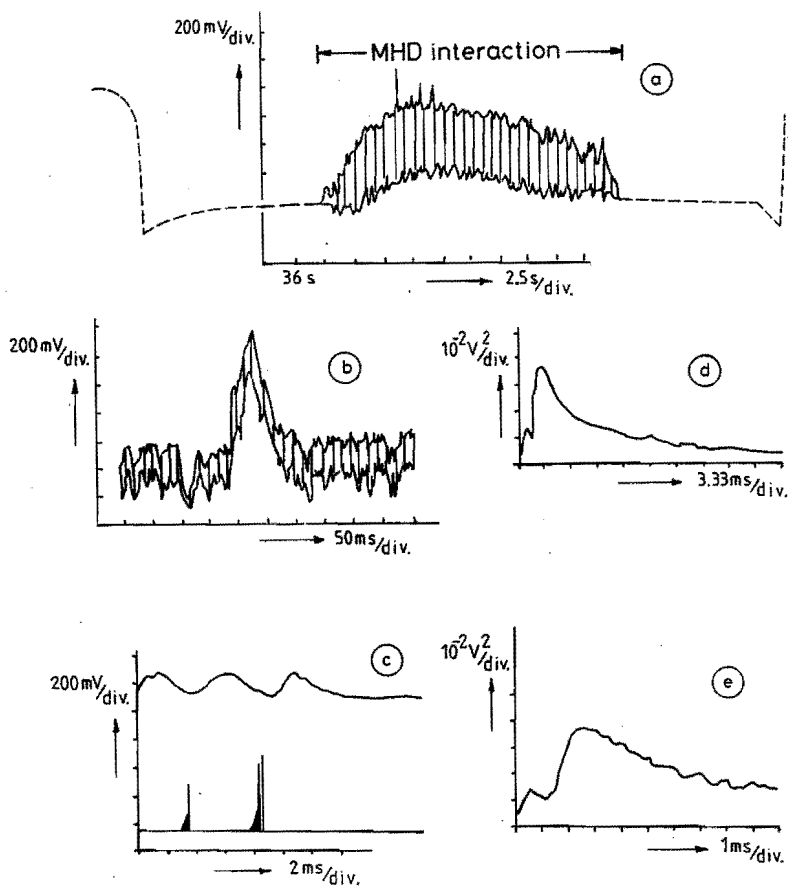
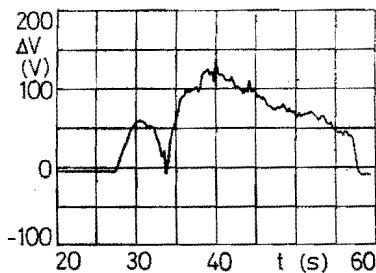
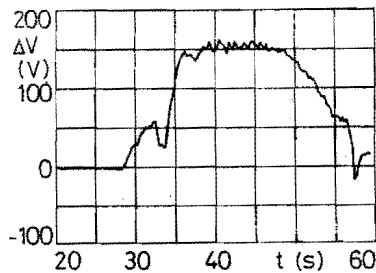


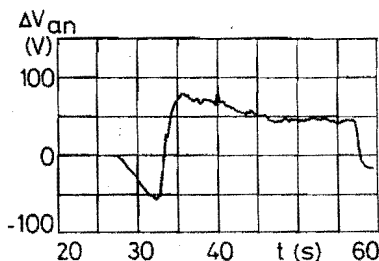
Fig. 38 Results of high frequency measurements of pressure p_{d5} during run 502; (a) variation from about 17 to 75 s, (b) around about $t = 44$ s, (c) upper trace pressure p_{d5} lower trace recombination radiation in the middle of the generator showing streamers, (d) and (e) cross correlation between p_{d5} and the current through the 17th electrode pair.



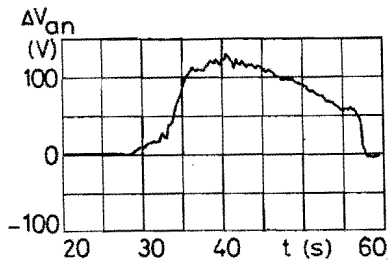
a) Total voltage drop at electrode pair 19.



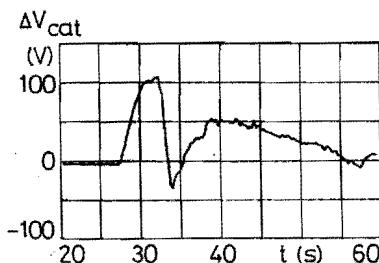
d) Total voltage drop at electrode pair 29.



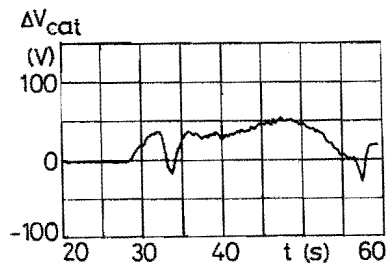
b) Anode voltage drop at electrode pair 19.



e) Anode voltage drop at electrode pair 29.



c) Cathode voltage drop at electrode pair 19.



f) Cathode voltage drop at electrode pair 29.

Fig. 39 Voltage drops as a function of time during run 302. Note that the electric power is generated from about 33 to 57 s.

5.1 A review of the numerical model which will be verified

A comparison of the results presented in section 3.3 with those of chapter 4 shows that the numerical model predicts a maximum enthalpy extraction (at an inlet stagnation pressure of 7 bar) which is a factor 2.4 larger than the value realized up to now in the experiment. There are three effects which contribute to this discrepancy between theory and experiment. The first effect is the influence of Hall shorting which always appears to be present in the experiments with the blow-down facility up to now. This effect is not taken into account in the model since the theory has been set up for properly functioning MHD generators. The second effect is the influence of the complicated filamentary discharge structures (streamers) observed in the experiment which is not described by the theoretical model for the electron gas presented in section 2.2.3. The third effect is the phenomenon of current relaxation in the inlet region of the MHD generator which has not yet been taken into account in the calculations.

All three effects lead to a reduction in electrical power output. The magnitude of the contribution of each effect separately to the reduction in power output will be estimated at the end of section 5.2. Of the three mentioned effects Hall shorting can in principle be avoided but the presence of streamers and the current relaxation phenomenon are inherent properties of the medium in closed cycle MHD generators.

In the following the model will therefore be generalized in such a way that the influence of the presence of streamers (and of the current relaxation) on the electrical behaviour of the generator can be taken into account in an average sense. This can be done by introducing an appropriate accommodation coefficient, the value of which will be determined from the measured total power output. It will appear that the disadvantage of this approach is that both the presence of the streamers and the Hall shorting influence the value of the accommodation coefficient.

Therefore new experiments are needed, in which Hall shorting is avoided, for a thorough confrontation between theory and experiment. These future experiments are also essential for a good confrontation of theory and experiment with regard to the gasdynamical behaviour. It will namely become clear from the discussion in section 5.3 that Hall shorting has also a large influence on the static pressure profile through the MHD generator. In the following the generalization of the model for the electron gas will be described. For a clear survey the differential equations describing the model of MHD core flow and MHD boundary layers will be presented also.

The equations describing the average electrical behaviour including streamers

The principle goal of the modification of the equations for the electron gas is to introduce an accommodation coefficient in such a way that the average electrical behaviour in the presence of streamers is properly described. This can be done by using the accommodation coefficient as a reduction factor for the critical Hall parameter. In this way the effective conductivity following from equation (2.32) is reduced and the influence of streamers can thus be taken into account. The disadvantage of this approach is that the Saha equations (2.6) and (2.7), Ohm's law (2.26) and equation (2.29) describing the electron energy balance have to be solved to determine the electric current density. An equivalent approach that leads to a highly simplified procedure for the calculation of the electric current density is to introduce the accommodation coefficient in the relation

$$|j_y| = A^* |E_y^*|^6 \quad (2.122)$$

This expression has been introduced in section 2.9 as an approximation to the relation between j_y and E_y^* obtained from the complete set of equations describing the electron gas. The accuracy of the approximation, which can be judged from figure 7, is reasonable in the range of interest for j_y . The relation (2.122)

is valid for the core flow when using the approximation (as discussed before) that the x-component of the current density can be neglected. This approximation follows from the results of the two-dimensional, time-dependent calculations of Hara [Hal] which show that the inclination of the streamers with respect to the y-direction can be neglected in the core flow.

A relation which is more convenient for the calculations can now be derived by combining equation (2.122) with Ohm's law. Again using that $j_x=0$ the two components of equation (2.26) for the core flow can be written in the form (compare with figure 2 for the definition of the coordinate system)

$$\sigma_{app} E_x - \beta_{app} j_y = 0 \quad (5.1)$$

$$j_y = -\sigma_{app} E_y^* = -\sigma_{app} (uB_z - E_y) \quad (5.2)$$

In these relations the subscript "app" for apparent has been introduced to denote a situation in the presence of streamers. Elimination of E_y^* from the equations (2.122) and (5.2) leads to

$$|j_y| = \sigma_{app} \left(\frac{|j_y|}{A^*} \right)^{1/6}$$

or

$$\sigma_{app} = A^{*1/6} |j_y|^{5/6} = B^* |j_y|^{0.833} \quad (5.3)$$

This is the essential relation with which the average electrical behaviour including streamers will be described. The coefficient B^* will not be deduced theoretically but will be adjusted in section 5.2 in such a way that it corresponds with one of the experimental results obtained with the blow-down experiment. Thereupon σ_{app} will be accepted as the apparent electrical conductivity in which the influence of the presence of streamers (and the reduction due to the influence of Hall shorting) has been taken into account.

The expression (5.3) for σ_{app} will now be used to describe the electrical behaviour in one segment of a Faraday generator with pitch s , height h and width b (see figure 2). In order to account

for the influence of boundary layers and of the voltage drop an equivalent resistance network is used which is drawn in figure 40.

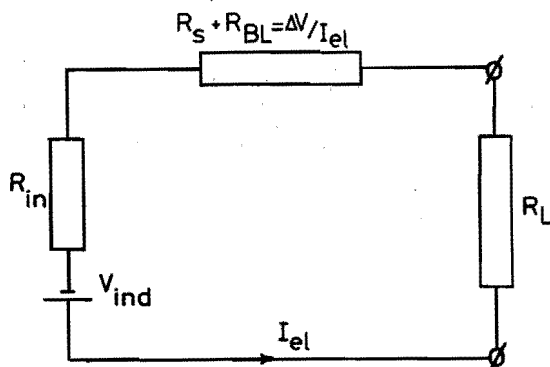


Fig. 40 Equivalent resistance network.

Applying the second law of Kirchhoff in the network yields the relation

$$uB_z(h - 2\bar{\delta}_{1,e}) - I_{el}R_{in} - \Delta V - I_{el}R_L = 0 \quad (5.4)$$

The first term in this relation denotes the induced potential difference V_{ind} , which has been corrected for the presence of the velocity profile (for simplicity the difference between $\delta_{1,e}$ and $\bar{\delta}_{1,e}$ has been neglected in the calculations). The external current from the segment can be written as

$$I_{el} = -j_y s(b - 2\delta_{j,i}) \quad (5.5)$$

In this relation the geometrical width b has been reduced with $2\delta_{j,i}$ since the total width is not available for carrying the current density j_y (compare section 2.4.1). Consistent with the relation (5.5) the internal resistance of the segment can be written as

$$R_{in} = \frac{h}{\sigma_{app} s(b - 2\delta_{j,i})} \quad (5.6)$$

In writing down this relation it is assumed that σ_{app} is valid for the core (as discussed before) and that all electrical effects due to boundary layers are taken into account by means of ΔV (it is assumed that ΔV is located entirely in the Debye sheath so that the height is not corrected). Substitution of the relations (5.5) and (5.6) in (5.4) leads to

$$uB_z(h - 2\bar{\delta}_{1,e}) + j_y \frac{h}{\sigma_{app}} - \Delta V - I_{e1}R_L = 0$$

Introducing $h_{eff} = h - 2\bar{\delta}_{1,e}$ this can also be written as

$$j_y = -\sigma_{app} \left(uB_z \frac{h_{eff}}{h} - \frac{\Delta V}{h} - \frac{I_{e1}R_L}{h} \right) \quad (5.7)$$

A comparison of the relations (5.2) and (5.7) shows that

$$E_y = \frac{I_{e1}R_L + \Delta V}{h} \quad (5.8)$$

which is consistent with figure 5.

To obtain a convenient way for calculating j_y the external specific resistivity ρ_u is introduced according to

$$\rho_u = \frac{R_L s(b - 2\delta_{j,i})}{h} \quad (5.9)$$

Using the relations (5.5), (5.8) and (5.9) E_y can then be written in the form

$$E_y = \frac{\Delta V}{h} - j_y \rho_u \quad (5.10)$$

Substitution of the relations (5.8) and (5.10) in (5.7) then leads to

$$j_y = -\sigma_{app} \left(uB_z \frac{h_{eff}}{h} - \frac{\Delta V}{h} \right) - \sigma_{app} j_y \rho_u$$

or

$$j_y = \frac{-\sigma_{app} \left(uB_z \frac{h_{eff}}{h} - \frac{\Delta V}{h} \right)}{1 + \sigma_{app} \rho_u} \quad (5.11)$$

Elimination of σ_{app} from equation (5.11) by means of (5.3) yields

$$|j_y|(1 + \rho_u B^* |j_y|^{0.833}) = B^* |j_y|^{0.833} \left(\frac{u B_z h_{eff} - \Delta V}{h} \right)$$

or

$$|j_y|^{0.167} + B^* \rho_u |j_y| = B^* \left(\frac{u B_z h_{eff} - \Delta V}{h} \right) \quad (5.12)$$

It will be clear from the foregoing discussion that the boundary layers affect the value of the current density by means of their influence on the values of the parameters ρ_u and h_{eff} . In this way a simple relation has been derived for j_y , without the need to solve the Saha equations and the electron energy balance. Equation (5.12) results in a reduction of the process time of the computer by about a factor three.

Finally it should be mentioned that the approximation (5.3) also gives the possibility to take into account the relaxation of the current density which is always observed in the inlet region of an MHD generator. This effect is taken into account by introducing the relation

$$B^* = C^* [1 - \exp(\frac{-x}{L_r})] \quad (5.13)$$

For the calculations in this chapter the current relaxation length L_r and the voltage drop ΔV will be determined from experimental results obtained in the blow-down experiment.

The x-component of Ohm's law for the core flow, which has not been used up to this point, gives an expression for E_x which can be integrated along the flow direction to obtain the total Hall potential. Elimination of j_y from the equations (5.1) and (5.2) yields

$$E_x = -\beta_{app} (u B_z - E_y) \quad (5.14)$$

Using the relation (5.10) the expression with which E_x will be calculated in this chapter is then written as

$$E_x = -\beta_{app} u B_z \left[1 - \frac{(\Delta V/h) - j_y \rho u}{u B_z} \right] \quad (5.15)$$

The value used for β_{app} in the calculations is taken from shock-tube experiments performed at EUT which yield for high values of the magnetic induction [B12]

$$\beta_{app} = 0.5 \quad (5.16)$$

A survey of the differential equations describing the model of MHD core flow and MHD boundary layers

The equations, derived in the sections 2.2 and 2.4, will be collected here in order to obtain a good survey of the model used but they will be presented without further discussion.

Continuity equation for the core flow

$$\frac{d}{dx} (\rho u A_{eff}) = 0 \quad (2.37)$$

Momentum equation for the core flow

$$\rho u \frac{du}{dx} = - \frac{dp}{dx} + j_y B_z \quad (2.22)$$

Energy equation for the core flow

$$\rho u \frac{dH}{dx} = j \cdot \vec{E} \quad (2.23)$$

Friction and heat conduction effects are not present in the equations (2.22) and (2.23) since these effects are taken into account by means of the boundary layer equations and A_{eff} .

Momentum integral equation for the boundary layers

$$\frac{d\delta_{2,q}}{dx} + \delta_{2,q} \left\{ \frac{d \ln \rho_{\infty}}{dx} + \frac{d \ln u_{\infty}}{dx} \left(2 + \frac{\delta_{1,q}}{\delta_{2,q}} \right) + D_q \right\} = \frac{C_f}{2} + \frac{j y_{\infty} B_z}{\rho_{\infty} u_{\infty}^2} \delta_{j,q} \quad ; \quad q = e, i \quad (2.45)$$

Kinetic energy integral equation for the electrode wall boundary layer

$$\frac{d\delta_{3,e}}{dx} + \delta_{3,e} \left\{ \frac{d \ln \rho_{\infty}}{dx} + \frac{d \ln u_{\infty}}{dx} \left(3 - 2 \frac{\delta_{4,e}}{\delta_{3,e}} \right) + D_e \right\} = 2C_D + \frac{2j y_{\infty} B_z}{\rho_{\infty} u_{\infty}^2} \delta_{j,u,e} \quad (2.50)$$

Stagnation-enthalpy integral equation for the boundary layers

$$\frac{d\delta_{H,q}}{dx} + \delta_{H,q} \left\{ \frac{d \ln \rho_{\infty}}{dx} + \frac{d \ln u_{\infty}}{dx} + \frac{H_{\infty}}{H_{\infty} - H_w} \frac{d \ln H_{\infty}}{dx} \left(1 + \frac{\delta_{1,q}}{\delta_{H,q}} \right) - \frac{H_w}{H_{\infty} - H_w} \frac{d \ln H_w}{dx} + D_q \right\} = St + \frac{E y_{\infty} j}{\rho_{\infty} u_{\infty} (H_{\infty} - H_w)} \delta_{Ej,q} \quad ; \quad q = e, i \quad (2.55)$$

The profile in the electrode wall boundary layer is determined by three parameters (N_e , δ_e' and $\Delta Q/Q_0$) and in the insulator wall boundary layer by two parameters (R_i and δ_i'). This is the reason why the kinetic energy integral equation for the insulator wall boundary layer is not used.

5.2 Analysis of the electrical performance

It has already been mentioned in section 5.1 that the coefficient B^* and thus C^* in the expressions (5.3) and (5.13) for σ_{app} will be determined for one condition in such a way that the produced electric power as calculated from the model, equals the value realized in the experiment. For this condition the situation in run 303 at maximum electric power is chosen. Then the results calculated by the model at different values of the magnetic induction during run 302 and run 303 will be presented and compared with the experimental results. Before we can discuss the results of

this procedure, however, we must treat the experimental input into the model which consists of the voltage drop and the current relaxation length.

The figures 41 and 42 show the measured values of the total voltage drop ΔV at different times in run 302 and 303. For the calculations ΔV is needed as a function of the coordinate x . Since the voltage drops are measured only at two locations namely at the electrode pairs 19 and 29 the simplest profile namely a linear relation is assumed. Figure 41 shows the problem which may then arise since the straight line drawn through the measured points results in negative ΔV values at $x=0$ for $t=45$ and 50 s which is impossible. This problem has been arbitrarily solved by averaging the values for ΔV at $x=0$ obtained at $t=39.25$ and 55 s and using this value for all lines in figure 41. Apart from the solid straight lines for $t=45$ and 50 s the dotted lines which pass exactly through the measured points have also been used. It has been found that these different approximations to the actual ΔV profile have only a small influence on the calculated electrical power output. Since the measurements seem to indicate that the true ΔV profile is not a straight line, the accuracy of the calculations can be improved when ΔV is measured at more locations in the generator.

The four values of the time chosen in figure 41 are the values at which the calculations will be performed. These times have been chosen in the domain of decreasing magnetic induction. They are distributed almost uniformly over the time interval from maximum magnetic induction to the time of disconnecting the power supply of the magnet. For run 303 the four times at which the calculations are performed are also chosen with about equal time intervals. Since the power supply of the magnet was manually disconnected early during run 303, $t=48.25$ s occurs after the time of disconnection (at which time there is still a magnetic induction present due to the time constant of the RL circuit containing the magnet).

Figure 42 shows the approximation used for the ΔV profile at different times in run 303. Because the mutual differences between the values of ΔV from $t=40.25$ to 45.75 s are rather small one

straight line through the average values is used. For $t=48.25$ s two approximations to the ΔV profile have been used. The first one is the straight line starting at the same value of ΔV at $x=0$ as used for the other times in this run and the second one is the straight line passing exactly through the measured values. Again these different approximations to the ΔV profile at $t=48.25$ s have only a limited influence on the calculated power output. Finally it should be noted that the values of ΔV measured during run 302 appear to be more reliable than the values obtained during run 303. This is based on the observation that ΔV increases with increasing magnetic induction (and increasing power output) during run 302 both at the 19th and at the 29th electrode pair. This relation between voltage drop and magnetic induction (or power output) is not observed during run 303 as can be seen from figure 42.

The other experimental input required by the model is the current relaxation length. Values of this parameter for the runs 302 and 303 at the selected times have been collected in table V. These values have been completed with values determined at the same magnitude of the magnetic induction but in the domain in which the latter increases. The value for the current relaxation length is easily determined from the picture of the current per electrode pair I_{e1} as a function of distance in the generator (compare figure 32a). It has been found that a relaxation length equal to half of the length corresponding with the maximum value of I_{e1} gives a good approximation to the curve of I_{e1} as a function of x . The values collected in table V show two tendencies. The first one is the trend that the relaxation length decreases when the magnetic induction increases. The second tendency is that the relaxation length is in general larger for increasing than for decreasing magnetic induction (when compared at the same B-value). The latter tendency is attributed to the fact that the surface temperature of the electrodes increases with time since they are heated by the streamers. Table V shows that the value of the load resistance (9Ω in run 302, 6Ω in run 303) apparently does not influence the current relaxation length.

The figures 43 and 44 show the results of the calculations for the runs 302 and 303 together with the experimental curve of the electrical power output as a function of the magnetic induction. As mentioned before a unique value for the coefficient C^* in the expressions (5.3) and (5.13) for σ_{app} has been determined in run 303 at $t=40.25$ s (maximum power output) in such a way that the measured and the calculated value of the electric power correspond. Using the voltage drop profile from figure 42 and the relaxation length from table V this approach results in the value

$$C^* = 2.6 \cdot 10^{-3} \quad (5.17)$$

which is a constant in the other calculations presented in this chapter both for run 302 and for run 303.

The direction in which the time increases along the experimental curves in the figures 43 and 44 has been indicated since the curves show a large hysteresis. This phenomenon may be explained from the difference in relaxation length for increasing or for decreasing values of the magnetic induction. Apart from the influence of the temperature of the electrodes which has been mentioned before as an explanation, it seems also logical that the value of the magnetic induction at which power production starts is not equal to the value at which the generation of power stops. This is clearly illustrated in the figures 43 and 44. It may probably be explained by a generally observed property of arcs namely the difference between the ignition voltage and the arc voltage (see for instance [Hoy1]).

It should be mentioned that the voltage drops are smaller for increasing than for decreasing magnetic induction (when compared at the same B -value). This is clear from the measurements made during run 302 and is true both for the values determined at the 19th as well as at the 29th electrode pair. It corresponds with the trend observed from figure 41 where the voltage drop increases when the electric power increases. This observation can not explain the hysteresis in the figures 43 and 44, however, since it counteracts the illustrated trend.

The agreement between the calculated and the measured electric

power for run 302 is good, as is clear from figure 43. Since the values of ΔV and L_r for the domain of decreasing magnetic induction have been used in the calculations, the same regime of the experimental curve is followed in figure 43. The difference between theory and experiment is less than 20% for values of the magnetic induction between 3.5 and 4 T and less than 5% for B-values larger than 4.3 T. (It should be mentioned that the experimental input into the calculations, namely the values of ΔV and L_r , is only known with a limited accuracy as discussed above).

At this moment it is useful to estimate the importance of the detailed calculation of the boundary layers in determining the theoretical curve in figure 43. This estimate is obtained by comparing the values in figure 43 with the results of the same calculation using the quasi-one-dimensional MHD flow model presented in section 3.1. In this model, in which the effects of friction and heat conduction are smeared out over the circumference of the channel cross-section, the electrical model including the influence of streamers and current relaxation is introduced. The current density is thus calculated by means of the equations (5.12) and (5.13) but now ρ_u and h_{eff} in equation (5.12) do not include the influence of the boundary layers. In the calculations the same values are used for the current relaxation length, the voltage drop profile and the constant C^* as used in calculating the theoretical curve in figure 43. The quasi-one-dimensional MHD flow model then yields an increase of power output of 35% in comparison with the values calculated by the model of MHD core flow and MHD boundary layers for values of the magnetic induction from 3.51 to 4.74 T. This increase of power output is mainly due to the neglect of the displacement thicknesses $\delta_{1,e}$, $\delta_{1,i}$ and $\delta_{j,i}$. This indicates that a correct calculation of the power output of high interaction MHD generators is not possible without a detailed calculation of the boundary layers.

The agreement between the calculated and the measured electric power is far worse for run 303 as shown in figure 44 and the calculated values are consistently too low. At a value of the magnetic induction of 4.6 T the model predicts 85% of the measured value but at 3.45 T the model comes only to 39% of the value in the experiment.

The explanation for the good agreement between theory and experiment illustrated in figure 43 for run 302 and the limited concurrence shown in figure 44 for run 303 may be attributed to Hall shorting problems during run 303. (It is certain that external Hall shorting was temporarily present during run 303 which led to the dip in power output shown in figure 44 after which the shorting disappeared).

The Hall shorting problems during run 303 have led to a strange behaviour of the total Hall potential which is apparent from a comparison of the figures 45 and 46. By plotting the total Hall potential against the magnetic induction the coupling between the two parameters during run 302 is clear from figure 45. The results of the theoretical calculations of the total Hall potential (in the domain of decreasing values of the magnetic induction and using $\beta_{app}=0.5$) have also been drawn in the figures 45 and 46 and show a linear relationship. A linear relation between total Hall potential and magnetic induction is also approximately valid according to the measurements in run 302 both at increasing and at decreasing values of the magnetic induction (see figure 45). Figure 46 shows that this linear relation is completely absent in run 303 (at least for values of the magnetic induction smaller than 4.5T) which illustrates the strange behaviour of the total Hall potential during this run. It should be noted that the figures 45 and 46 show also a general discrepancy between the measured and the calculated values of the Hall potential for both run 302 and run 303. The maximum Hall potential measured in run 302 for instance is only 61% of the corresponding calculated value.

Another, perhaps even more striking, illustration of the strange behaviour of the Hall potential during run 303 may be obtained from a comparison of the figures 47 and 48. By plotting the total Hall potential against the electric power the coupling between these two

parameters during run 302 is clear from figure 47. Here the results of the theoretical calculations have also been drawn which show again a linear relationship. This linear relation between total Hall potential and electric power is also approximately valid according to the measurements in run 302 both at increasing and at decreasing values of the magnetic induction. Such a linear relation between total Hall potential and electric power has also been observed during the runs 501 and 502 in spite of the fluctuations in and the low level of the power output during these runs (compare figure 31). Figure 48 shows that this linear relation is completely absent during run 303. This figure illustrates that there is even a regime where the electric power decreases at a constant value of the total Hall potential (indicating a relative decrease of the Hall shorting problems). The situation at the smallest value of the magnetic induction used in the calculations for run 303 corresponds with the very special regime just indicated ($B=3.45T$, measured power production 182 kW). It is therefore not astonishing that there exists a large discrepancy between theory and experiment in this condition as shown in figure 44.

At this moment it may be concluded that the developed model is very useful for the interpretation of the measurements. This may be illustrated further by using the model of MHD core flow and MHD boundary layers to estimate the contribution of the various loss mechanisms to the reduction of the power output in comparison with the theoretical predictions presented in section 3.3. This will be performed for the situation corresponding with the maximum power production during run 303. For this comparison the value of the coefficient C^* under the various conditions will be estimated. For the profile of the voltage drop and for the value of the relaxation length the data from figure 42 and from table V will be used.

(i) From a recent compilation of experimental results of the EUT shock-tunnel experiment by Veeffkind [Vee3] and using the electrical model from section 5.1 a value $C^*=3.63_{10}^{-3}$ is determined for the shock-tunnel conditions. It is assumed that the main difference between the blow-down and the shock-tunnel conditions is the

virtual absence of Hall shorting problems under the latter conditions. The value $C^*=3.63 \cdot 10^{-3}$ gives a power output of 515 kW or in other words an increase of 49% relative to the maximum power output of run 303, which is therefore attributed to the elimination of Hall shorting.

(ii) Using the straight line approximation in figure 7 a value $C^*=4.56 \cdot 10^{-3}$ is determined, which thus corresponds with the theoretical model for the electron gas presented in section 2.2.3. This value of C^* gives a power output of 629 kW or in other words an increase of 22% relative to case (i). This increase is attributed to the absence of the adverse influence of streamers in the calculated curve in figure 7.

(iii) The difference in power output quoted at the end of chapter 3 relative to the value of case (ii) implies an increase of 30%. The main influence with which this increase can be explained, is current relaxation in the inlet region of the MHD generator which has not been taken into account in chapter 3.

It should be noted that the estimated contributions of the three loss mechanisms to the reduction of power output yield comparable values when the situation corresponding with the maximum power output of run 302 is considered.

5.3 Analysis of the gasdynamical behaviour

The only experimental quantity relevant to the gasdynamical behaviour which is measured during the experiment is the static pressure at different locations in the hot flow train. Figure 49 shows the variation of the static pressure with the coordinate x as measured in run 302 at maximum interaction and as calculated by the model presented in section 5.1 for the same conditions. Figure 49 shows a large discrepancy between the two curves in the second half of the generator and in the supersonic diffuser. This discrepancy between calculated and measured static pressures is typical for the gasdynamical behaviour of the MHD generator in the EUT blow-down experiment up to this moment. This is illustrated also by the

figures 50 and 51. It is shown by the figures 50 and 51 for run 302 that the discrepancy in the pressure p_{g5} is present over a large range of values of the electric power (and of the magnetic induction). It should be noted that the difference between the calculated and the measured static pressure at the location p_{g5} is of the same order of magnitude in run 303. The figures 50 and 51 show also that the measured and the calculated value of the static pressure are equal up to a value of the electric power of about 70 kW corresponding with a value of the magnetic induction of about 3.3 T. This may not be true for the entire MHD generator, however, since the figures 50 and 51 show the situation at the location where the pressure p_{g5} is measured ($x=0.563\text{m}$). Figure 37^b shows that the strong increase of the static pressure starts in the outlet region of the generator when the MHD interaction comes up. Since the pressure transducer measuring p_{g6} did not function properly during measurement series 3, pictures similar to the figures 50 and 51 can not be obtained for this location. Therefore a proper conclusion about the value of the power output at which the measured static pressures begin to deviate from the calculated values can not be drawn at this moment.

An estimate according to the approach of Huijgen [Hui] shows that the difference between the measured and the calculated value of the static pressure shown in figure 49 can be explained when the boundary layer thickness in the experiment is a factor 2.5 larger than the calculated value (at $x=0.8\text{ m}$). There are two possible explanations for such a large difference in boundary layer thicknesses. The first possibility is that the interaction of the streamers and the boundary layer may lead to an additional growth of the boundary layer thickness. High speed photography in the EUT shock-tube experiment [Sen] has led to the understanding that a streamer is attached for a relatively long time to an electrode pair. Since the streamers move with approximately the gas velocity in the core flow, this implies a lengthening of the streamer close to the wall. This process continues until the streamer length is so large that it is energetically more advantageous to make a connection to a following electrode pair. Flinsenbergh [Fl] has

shown that the interaction of the streamer with the gas flow may be described by considering the streamer as a solid body. Therefore the streamers may have a large influence on the boundary layer. The described interaction process seems very complicated. It is probably three-dimensional in nature and will require a thorough study before a description of the process can be attempted. The second possible explanation of the observed difference between the measured and the calculated value of the static pressures is the influence of Hall shorting in the experiment. The results discussed in section 5.2 have shown a strange behaviour of the total Hall potential during run 303. The figures 45 and 47, however, show that the measured Hall potential is also considerably smaller than the calculated value during run 302. The reduction of the Hall field, which has been observed in all runs of the blow-down experiment up to now, can be explained only through the action of Hall currents. The Hall currents have a preference to flow through the electrode wall boundary layer which leads to an additional thickening of this boundary layer because of two reasons. The Hall currents will lead to additional Joule dissipation in the boundary layer which implies a further increase of the parameter $\Delta Q/Q_0$ (compare section 2.6.3). Furthermore the Hall currents will give a vertical component of the Lorentz force which leads to additional thickening (possibly even early separation) of the cathode wall boundary layer (compare with the discussion at the end of section 4.3). Another consequence of a vertical component of the Lorentz force is that the static pressure measured at the wall may differ considerably from its value in the core flow. The experimental work of Reilly [Reil] confirms these statements. Reilly has measured a strong increase of static pressure in the second half of his MHD generator comparable to the profile shown in figure 49. Since his MHD generator was built up from peg walls, a large number of pressure taps was available. Reilly could therefore measure static pressures at many locations at the walls and showed that large gradients in static pressure occurred both in the y- and in the z-direction due to the action of Hall currents.

Demetriades [De2] has shown that Hall shorting can even lead to complicated three-dimensional flow phenomena since the y-component of the Lorentz force may create secondary flow cells. In the present work no attempt was made to take the effect of Hall shorting into account since the aim of the work was to develop a model for a properly working MHD generator. Apart from that, the effects of pressure gradients in the y- and z-direction can not be described in a one-dimensional model.

The conclusion of this section therefore has to be that there remains a difference between the calculated and the measured profile of the static pressures in the second half of the MHD generator. Two possible explanations of the discrepancy have been indicated namely boundary layer thickening due to the interaction with streamers or due to Hall currents. For a definite answer on the explanation of the discrepancy new experiments are required under conditions where Hall shorting is avoided.

Table V The current relaxation length L_r at different values of the magnetic induction (time t_1 at increasing values of B, time t_2 at decreasing values of B).

Run	B (T)	t_1 (s)	L_r (m)	t_2 (s)	L_r (m)
302	3.51	-	-	55	0.27
	3.87	33.25	0.35	50	0.23
	4.37	35.25	0.27	45	0.19
	4.5	36.25	0.23	43.5	0.22
	4.74	39.25	0.19	39.25	0.19
303	3.45	-	-	48.25	0.25
	4.6	34.75	0.23	45.75	0.21
	4.87	36	0.21	43	0.17
	5.07	40.25	0.17	40.25	0.17

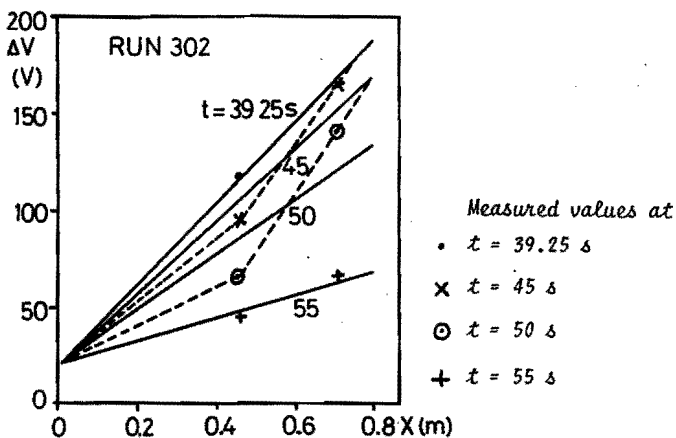


Fig. 41 Voltage drop ΔV as a function of distance in the generator.

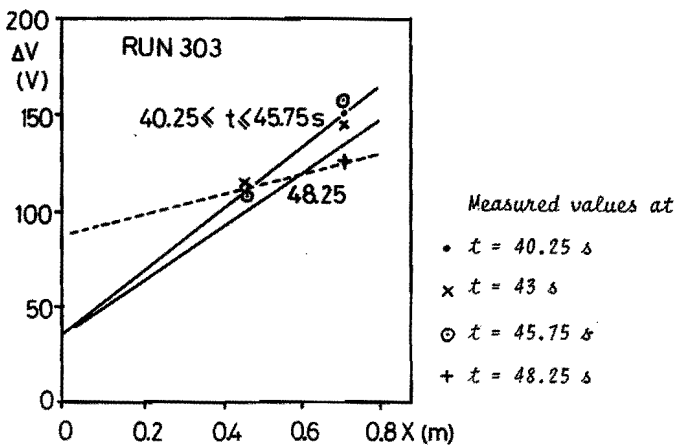


Fig. 42 Voltage drop ΔV as a function of distance in the generator.

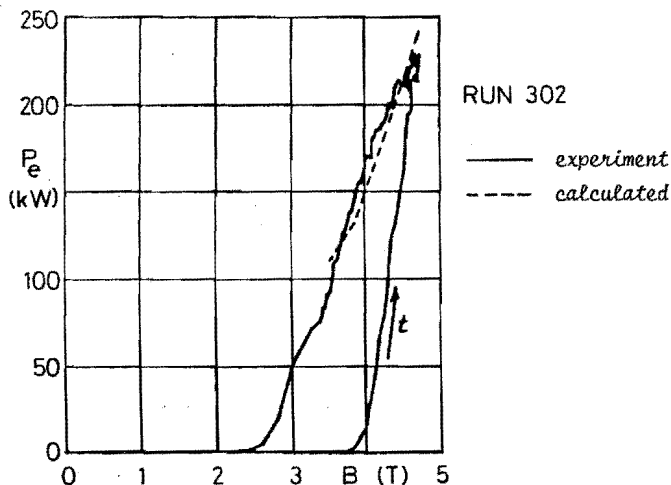


Fig. 43 Electrical power output P_e as a function of magnetic induction B .

Note that the arrow indicates the direction of increasing time.

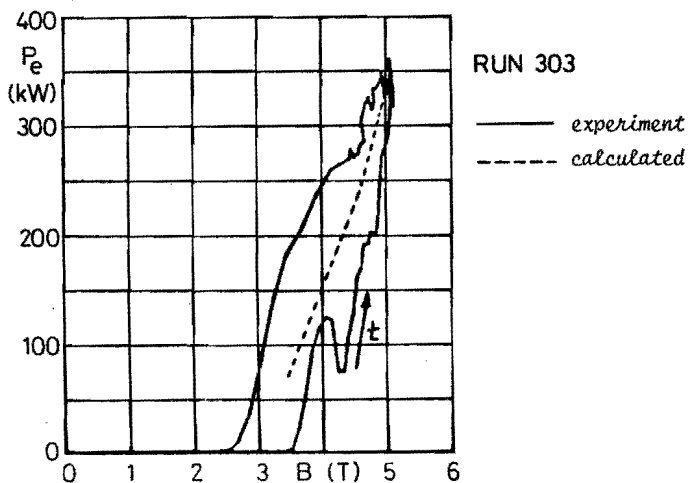


Fig. 44 Electrical power output P_e as a function of magnetic induction B .

Note that the arrow indicates the direction of increasing time.

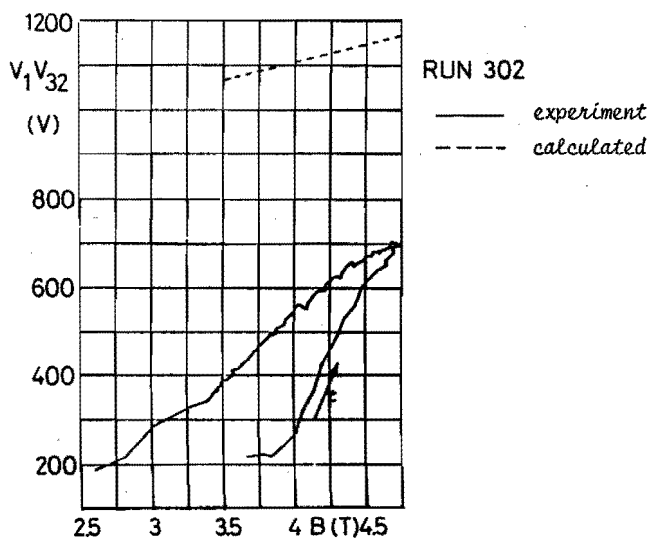


Fig. 45 Total Hall voltage V_1V_{32} as a function of magnetic induction B.

Note that the arrow indicates the direction of increasing time.

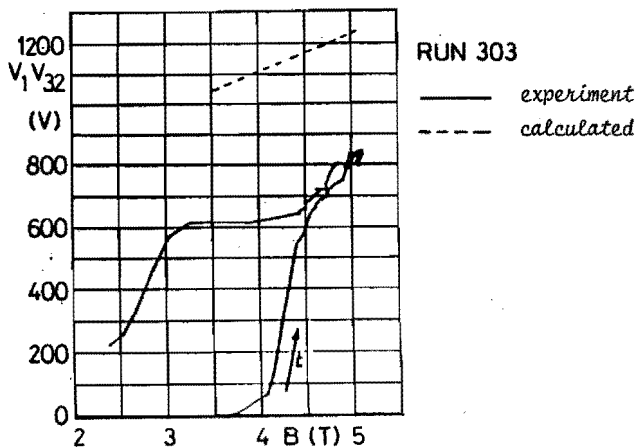


Fig. 46 Total Hall voltage V_1V_{32} as a function of magnetic induction B.

Note that the arrow indicates the direction of increasing time.

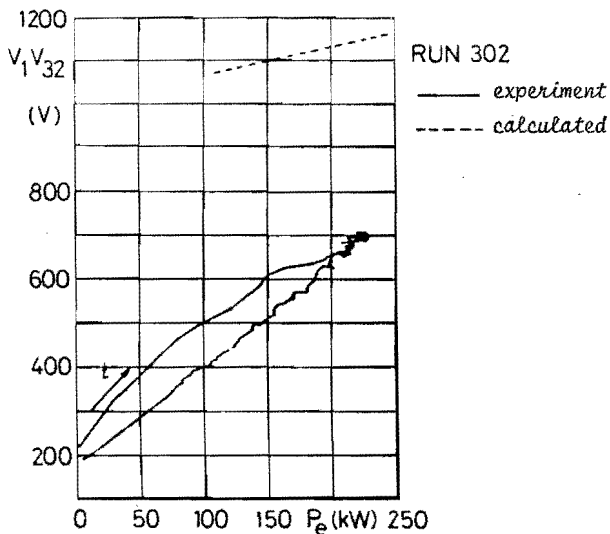


Fig. 47 Total Hall voltage V_1V_{32} as a function of power output P_e . Note that the arrow indicates the direction of increasing time.

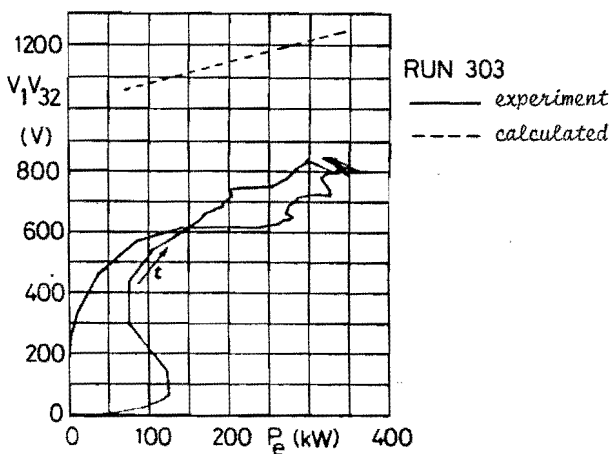


Fig. 48 Total Hall voltage V_1V_{32} as a function of power output P_e . Note that the arrow indicates the direction of increasing time.

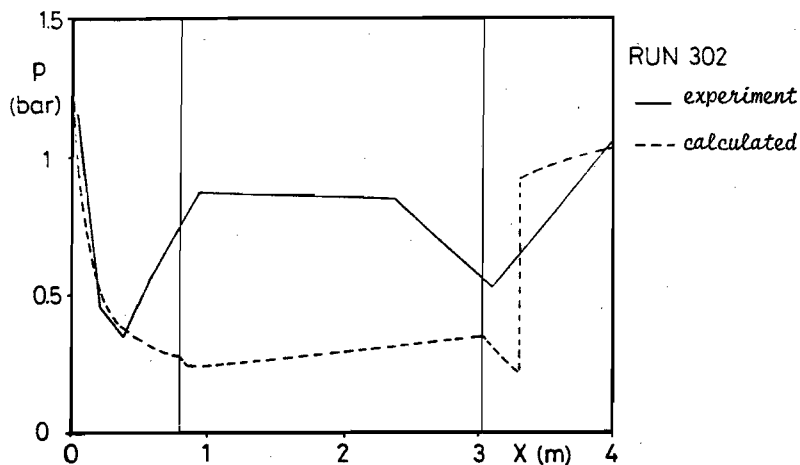


Fig. 49 Static pressure p as a function of distance through the hot flow train at $t = 39.25$ s ($P_e = 230$ kW).

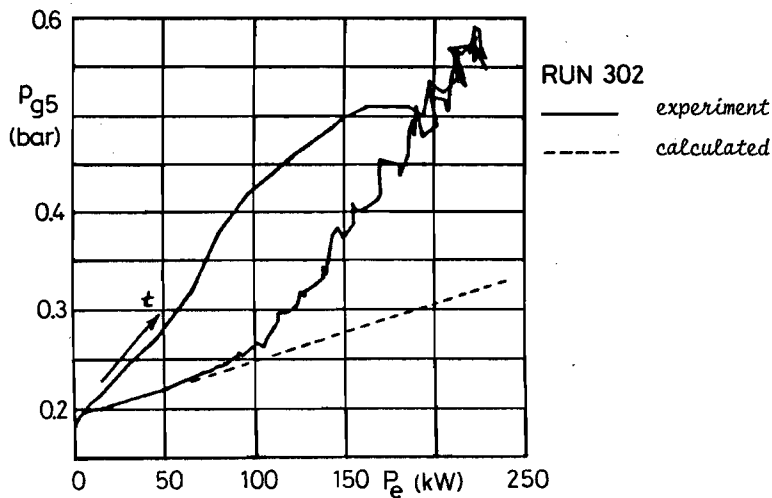


Fig. 50 Static pressure p_{g5} (at $x \approx 0.56$ m) as a function of power output P_e .

Note that the arrow indicates the direction of increasing time.

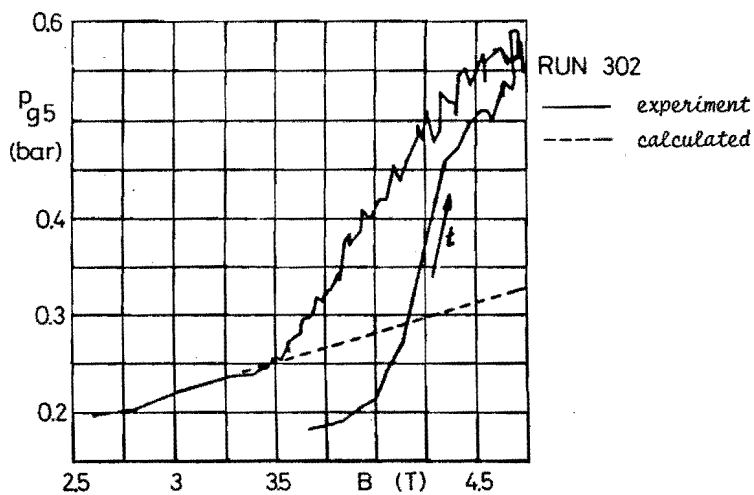


Fig. 51 Static pressure p_{g5} (at $x \approx 0.56$ m) as a function of magnetic induction B .

Note that the arrow indicates the direction of increasing time.

Conclusions

1. For a proper description of the gasdynamical behaviour of an MHD generator at high interaction, MHD effects should be taken into account in the boundary layer equations (chapter 3).
2. The results of the calculations presented in section 3.3 are sensitive to the value of the voltage drop. This can be explained from the fact that the boundary layer is sensitive to the magnitude of the Ohmic losses dissipated inside. This is in agreement with results from two-dimensional calculations.
3. The electric power generated up to now in the EUT blow-down experiment has been limited by the divergence of the generator (section 3.3), by the design of the supersonic diffuser (section 3.1) and by Hall shorting (chapter 5). The first limitation can be avoided by increasing the inlet stagnation pressure and/or by increasing the divergence of the MHD generator. Furthermore it may be considered to do special experiments for optimizing the length of the supersonic diffuser. Finally additional experiments are needed in order to reduce Hall shorting problems.
4. A one-dimensional model of MHD core flow and MHD boundary layers has been developed which may be used for the preliminary design of high interaction MHD generators and for studying the influence of the variation of parameters.
5. A correct calculation of the power output of high interaction MHD generators is not possible without a detailed calculation of the boundary layers. Under the conditions of run 302 the neglect of the displacement thicknesses $\delta_{1,e}$, $\delta_{1,i}$ and $\delta_{j,i}$ gives an over-estimation of the power output of 35%.

6. The model of MHD core flow and MHD boundary layers has appeared to be very useful for the interpretation of the measurements. An analysis at the condition of maximum power output in run 303 has led to the conclusion that the power output will increase with 49% when Hall shorting problems can be eliminated.
An increase of the power output of 22% as indicated by the model in case that the adverse influence of streamers is not present, is not considered achievable.
The power output can increase with 30% when the current relaxation in the inlet region of the MHD generator can be eliminated.
7. There is a discrepancy between the static pressure profile calculated by the model and the measured profile. The measured static pressures generally show a strong increase in the second half of the MHD generator, which is not predicted by the model.
8. The discrepancy between the measured and the calculated static pressures can be explained by boundary layer thicknesses which are larger in the experiment than the values calculated by the model.
9. There are two possible explanations for the extra thick boundary layers in the experiment. One explanation is the interaction of the streamers and the electrode wall boundary layer. The second explanation is the effect of Hall shorting. The Hall shorting is the result of Hall currents in the boundary layer leading to additional Joule dissipation and to a vertical component of the Lorentz force. Both effects result in additional thickening of the boundary layer.
10. In order to find out if the strong increase of the static pressures in the second half of the MHD generator can be prevented, additional measurements are needed particularly under conditions where Hall shorting is avoided.

Recommendations

1. The first recommendation is to pay extra attention to the mechanical construction of the MHD channel for the EUT blow-down facility in order to create the possibility of completing a full set of experimental runs during one measurement series.
2. Since the developed model requires the profile of the voltage drop as an input for the calculations, it is recommended to measure the voltage drop at least at four locations.
3. In order to avoid Hall shorting problems, experiments with increased pitch between the electrodes and experiments with a limited value of the magnetic induction are recommended.
4. An attempt should be made to use the codes developed by Demetriades et al. for a calculation of the processes in the hot flow train of the EUT blow-down experiment. In this way information can be obtained on the fact whether three-dimensional flow phenomena influence the experimental results at high interaction parameters.

References

- A11 Alber, I.E. and Coats, D.E., "Analytical investigations of equilibrium and nonequilibrium compressible turbulent boundary layers", AIAA paper no. 69-689, (1969).
- Ar1 Argyropoulos, G.S. et al., "Compressible turbulent Magnetohydrodynamic boundary layers", Phys. of Fluids, Vol. 11, p. 2559, (1968).
- Art1 Arts, J.G.A. and Merck, W.F.H., "Two-dimensional MHD boundary layers in Argon-Cesium plasmas", EUT Report 83-E-139, Eindhoven Univ. of Techn., Eindhoven, (1983).
- Ba1 Bates, D.R. et al., "Recombination between electrons and atomic ion. I optically thin plasmas", Proc. Roy. Soc. A, Vol. 267, p. 297, (1962).
- B11 Blom, J.H. "Relaxation phenomena in an MHD generator with pre-ionizer", Ph.D. thesis, Eindhoven Univ. of Techn., Eindhoven, (1973).
- B12 Blom, J.H. et al., "High power density experiments in the Eindhoven shock-tunnel MHD generator", Proc. of the 6th Int. Conf. on MHD, Washington, Vol. 3, p. 73, (1975).
- Br1 Brederlow, G. et al., "Reduction of the open circuit voltage by boundary layer leakage currents in experimental Faraday type MHD generators", Proc. of the 4th Int. Conf. on MHD, Warsaw, Vol. I, p. 419, (1968).
- Bro1 Brown, R.T., "Electron temperature and number density measurements in a nonequilibrium plasma boundary layer", SU-IPR Report no. 350, Stanford Univ. Inst. for Plasma Research, Stanford, Cal., (1970).
- Bro2 Brown, S.C., "Basic Data of Plasma Physics", John Wiley and Sons, Inc., New York, (1959).
- Bu1 Busemann, A., "Gasdynamik", Handbuch der Experimentalphysik, Vol. 4, pt. 1, p. 341, Akademische Verlagsgesellschaft, Leipzig, (1931).
- C11 Clauser, F.H., "Turbulent boundary layers in adverse pressure gradients", Journ. Aeronaut. Sci., Vol. 21, p. 91, (1954).
- Co1 Coles, D.E., "The law of the wake in the turbulent boundary layer", Journ. of Fluid Mech., Vol. 1, p. 191, (1956).

- Cool Cook, C.S. and Dickinson, K.M., "Argon contamination associated with ceramic regenerative heat exchangers for closed cycle MHD", Proc. of the 16th Symp. on Eng. Asp. of MHD, p. II.4, Pittsburgh, (1977).
- Cot1 Cott, D.W., "Ionizational and electron thermal nonequilibrium in MHD boundary layers", AIAA Journ., Vol. 9, p. 2404, (1971).
- Cr1 Crocco, L., "Su di un valor massimo del coefficiente di trasmissione del calore da una lamina piana a un fluido scorrente", L'Aerotechnica, Vol. 12, p. 181, (1932).
- Cra1 Crawford, M.E. and Kays, W.M., "Stan-5 a program for numerical computation of two-dimensional internal/external boundary layer flows", NASA CR 2742, (1976).
- Dal Dailey, J.W., "Boundary layer phenomena in combustion driven MHD power generators", Ph.D. thesis, Stanford Univ., Stanford, Cal., (1975).
- Del Demetriades, S.T. et al., "Progress in analytical modelling of MHD power generators", Proc. of the 12th Symp. on Eng. Asp. of MHD, p. I.5, Argonne, Ill., (1972).
- De2 Demetriades, S.T. et al., "Progress in analytical modelling of MHD power generators II", Proc. of the 21st Symp. on Eng. Asp. of MHD, p. 3.1, Argonne, Ill., (1983).
- Dol1 Doss, E.D., "MHD boundary layers on a segmented electrode wall of a nonequilibrium MHD generator", Ph.D. thesis, Univ. of California at Davis, Davis, Cal., (1972).
- Do2 Doss, E.D. et al., "Influence of Hall currents on flow separation and asymmetry in MHD channels", AIAA paper no. 74-509, (1974).
- Dol1 Dolson, R.C., "A computer analysis for the determination of electrode voltage losses in Magnetohydrodynamic generator plasmas", Ph.D. thesis, Naval Postgraduate School, Monterey, Cal., (1975).
- Dr1 van Driest, E.R., "Turbulent boundary layers in compressible fluids", Journ. Aeronaut. Sci., Vol. 18, p. 145, (1951).
- En1 von Engel, A. und Steenbeck, M., "Elektrische Gasentladungen", Vol. 1, p. 87, Verlag von Julius Springer, Berlin, (1932).
- Fel1 Felderman, E.J. et al., "HPDE performance in the Faraday mode", Proc. of the 20th Symp. on Eng. Asp. of MHD, p. 4.5, Irvine, Cal., (1982).

- F11 Flinsenberg, H.J., "Fossil fired closed cycle MHD power generating experiments", Ph.D. thesis, Eindhoven Univ. of Techn., Eindhoven, (1983).
- F12 Flinsenberg, H.J. et al., "Instability analysis of the first power runs with the Eindhoven MHD blow-down facility", Proc. of the 20th Symp. on Eng. Asp. of MHD, p. 12.1, Irvine, Cal., (1982).
- Gal Garner, H.C., "The development of turbulent boundary layers", ARC of Britain, Rep. and Memor. no. 2133, London, (1944).
- Gel Gertz, J. et al., "Modelling of MHD channel boundary layers using an integral approach", Proc. of the 18th Symp. on Eng. Asp. of MHD, p. B4.1, Butte, Mont., (1979).
- Ger1 Gerhart, P.M., "An integral method for predicting subsonic turbulent separating boundary layers with specified free stream input", Proc. ASME Conf. on "Turbulent boundary layers, forced, incompressible, non-reacting", edited by Weber, H.E., p. 59, New York, (1979).
- Gey1 Geyer, H.K. and Pierson, E.S., "Solar liquid metal MHD performance predictions", Proc. of the 20th Symp. on Eng. Asp. of MHD, p. 6.1., Irvine, Cal., (1982).
- Hal Hara, T. et al., "Numerical analysis of the nature of streamers in noble gas MHD generator", Proc. of the 8th Int. Conf. on MHD, Vol. 4, p. 136, Moscow, (1983).
- Hall Hale, F.J. and Kerrebrock, J.L., "Insulator wall boundary layers in Magneto-Hydrodynamic channels", AIAA Journ., Vol. 2, p. 461, (1964).
- He1 Hellebrekers, W.M., "Instability analysis in a nonequilibrium MHD generator", Ph.D. thesis, Eindhoven Univ. of Techn., Eindhoven, (1980).
- Hi1 High, M.D. and Felderman, E.J., "Turbulent MHD boundary layers with electron thermal nonequilibrium and finite rate ionization", AIAA Journ., Vol. 10, p. 98, (1972).
- Ho1 Houben, J.W.M.A. and Massee, P., "MHD power conversion employing liquid metals", TH-Report 69-E-06, Eindhoven Univ. of Techn., Eindhoven, (1969).
- Ho2 Houben, J.W.M.A., "Loss mechanisms in an MHD generator", Ph.D. thesis, Eindhoven Univ. of Techn., Eindhoven, (1973).

- Hof1 Hoffert, M.I. and Lien, H., "Quasi-one-dimensional, nonequilibrium gasdynamics of partially ionized two-temperature argon", Phys. of Fluids, Vol. 10, p. 1769, (1967).
- Hoy1 Hoyaux, M.F., "Arc Physics", Springer Verlag, Berlin, (1968).
- Hr1 Hruby, V.J. et al., "1000 hour MHD anode test", Proc. of the 20th Symp. on Eng. Asp. of MHD, p. 4.3, Irvine, Cal., (1982).
- Hul Huijgen, G., "Het gasdynamisch gedrag van MHD generatoren in relatie tot het opgewekte elektrische vermogen", M.Sc. thesis, Eindhoven Univ. of Techn., Eindhoven, (1983).
- Jal James, R.K., "Joule heating effects in the electrode wall boundary layer of MHD generators", HTGL Report no. 115, Stanford Univ. High Temp. Gasdynamics Lab., Stanford, Cal., (1980).
- Kal von Kármán, T., "Mechanische Ähnlichkeit und Turbulenz", Nachr. Ges. Wiss. Goett. Math.-Phys. Kl., p. 58, (1930).
- Kel Kerrebrock, J.L., "Similar solutions for boundary layers in constant temperature Magneto-Gasdynamic channel flow", Journ. of the Aerospace Sci., Vol. 27, p. 156, (1960).
- Ke2 Kerrebrock, J.L., "Electrode boundary layers in direct current plasma accelerators", Journ. of the Aerospace Sci., Vol. 28, p. 631, (1961).
- Kol Koester, J.K., "Analytical and experimental studies on thermionically emitting electrodes in contact with dense, seeded plasmas", Ph.D. thesis, Cal. Inst. of Techn., Pasadena, Cal., (1970).
- Kr1 Krause, J.C., "Gasdynamisch gedrag van MHD generatoren", M.Sc. thesis, Eindhoven Univ. of Techn., Eindhoven, (1981).
- Kul Kuhn, G.D. and Nielsen, J.N., "Prediction of turbulent separated boundary layers", AIAA paper no. 73-663, (1973).
- Lel Lengyel, L.L., "Two-dimensional current distributions in Faraday type MHD energy converters operating in the nonequilibrium conduction mode", Energy Conversion, Vol. 9, p. 13, (1969).
- Lul Ludwig, H. and Tillmann, W., "Investigations of the wall shearing stress in turbulent boundary layers", NACA TM 1285, (1950).
- Mal Masee, P. et al., "Gasdynamic performance in relation to the power extraction of the Eindhoven MHD blow-down facility", Proc. of the 20th Symp. on Eng. Asp. of MHD, p. 7.4, Irvine, Cal., (1982).

- Ma2 Masee, P. et al., "Gasdynamic performance in relation to the power extraction of the Eindhoven MHD blow-down facility", Proc. of the 8th Int. Conf. on MHD, Vol. 1, p. 192, Moscow, (1983).
- Mai1 Maise, G. and McDonald, H., "Mixing length and kinematic eddy viscosity in a compressible boundary layer", AIAA Journ., Vol. 6, p. 73, (1968).
- Mc1 McClaine, A.W. et al. "Performance characteristics of subsonic generators", Proc. of the 20th Symp. on Eng. Asp. of MHD, p. 4.1, Irvine, Cal., (1982).
- Me1 Merck, W.F.H., "On the fully developed turbulent compressible flow in an MHD generator", Ph.D. thesis, Eindhoven Univ. of Techn., Eindhoven, (1971).
- Mes1 Mesland, A.J., "Linear and nonlinear instability theory of a noble gas MHD generator, Ph.D. thesis, Eindhoven Univ. of Techn., Eindhoven, (1982).
- MHD4 MHD generator computer code, AVCO Everett Research Laboratory, Inc., Everett, Mass., unpublished.
- Mi1 Mitchner, M. and Kruger, C.H., "Partially Ionized Gases", John Wiley and Sons, Inc., New York, (1973).
- Na1 Nakamura, T., "An integral method analysis of the disk generator boundary layer", Proc. of the 20th Symp. on Eng. Asp. of MHD, p. 6.6, Irvine, Cal., (1982).
- O11 Olin, J.G., "Turbulence suppression in Magnetohydrodynamic flows", SU-IPR Report no. 85, Stanford Univ. Inst. for Plasma Research, Stanford, Cal., (1966).
- Ow1 Owen, P.R. and Thomson, W.R., "Heat transfer across rough surfaces", Journ. of Fluid Mech., Vol. 15, p. 321, (1963).
- Pal Patankar, S.V. and Spalding, D.B., "Heat and mass transfer in boundary layers", Intertex, London, (1970).
- Pi1 Pian, C.C.P. and Merck, W.F.H., "Boundary layer separation from the electrode wall of an MHD generator", AIAA Journ., Vol. 14, p. 1585, (1976).
- Pr1 Prandtl, L., "Bericht über Untersuchungen zur ausgebildeten Turbulenz", Z. Angew. Math. Mech., Vol. 5, p. 136, (1925).
- Ra1 Rankin, R.R., "Insulating wall boundary layer in a Faraday MHD generator", HTGL Report no. 106, Stanford Univ. High Temp. Gasdynamics Lab., Stanford, Cal., (1978).

- Rel Reshotko, E. and Tucker, M., "Approximate calculation of the compressible turbulent boundary layer with heat transfer and arbitrary pressure gradient", NACA TN 4154, (1957).
- Rei1 Reilly, J.P., "Open- and short circuit experiments with a nonequilibrium MHD generator using both cold and hot insulator walls", Energy Conversion, Vol. 10, p. 13, (1970).
- Ro1 Rosa, R.J., "Magnetohydrodynamic Energy Conversion", Mc.Graw Hill, New York, (1968).
- Ro2 Rosa, R.J., "Boundary layer voltage loss comparisons", Proc. of the 19th Symp. on Eng. Asp. of MHD, p. 5.3, Tullahoma, Tenn., (1981).
- Rot1 Röttenbacher, R. and Willmann, G., "Si SiC- a material for high temperature ceramic heat exchangers", European Colloquium on Ceramics in Advanced Energy Technologies, Petten, The Netherlands, (1982).
- Sal Sandborn, V.A. and Kline, S.J., "Flow models in boundary layer stall inception", Journ. Basic Eng., Trans ASME, Vol. 83, p. 317, (1961).
- Sc1 Schlichting, H., "Boundary layer theory", Mc. Graw Hill, New York, (1979).
- Se1 Seidman, M.H., "Rough wall heat transfer in a compressible turbulent boundary layer", AIAA paper no. 78-163, (1978).
- Sen1 Sens, A.F.C. et al., "Investigations on the gasdynamical effects of a non-uniform supersonic flow with streamers in a noble gas MHD generator", Proc. of the 20th Symp. on Eng. Asp. of MHD, p. 10.6, Irvine, Cal., (1982).
- Sh1 Sherman, A. and Reshotko, E., "The nonequilibrium boundary layer along a channel wall", AIAA paper no. 68-134, (1968).
- Sh2 Sherman, A. et al., "MHD boundary layers with nonequilibrium ionization and finite rates", AIAA paper no. 71-139, (1971).
- Sn1 Snel, H., Lindhout, J. et al., "Two-dimensional MHD duct flow: numerical analysis and measurements", Proc. of the 6th Int. Conf. on MHD, Vol. IV, p. 171, Washington, (1975).
- Sol1 Solbes, A., "Instabilities in nonequilibrium MHD plasmas, -a review", AIAA paper no. 70-40, (1970).
- Son1 Sonju, O.K. et al., "Comparison of experimental and analytical results for a 20 MW combustion driven Hall configuration MHD

- generator", Proc. of the 11th Symp. on Eng. Asp. of MHD, p. 5, Pasadena, Cal., (1970).
- Spal Spalding, D.B. and Chi, S.W., "The drag of a compressible turbulent boundary layer on a smooth flat plate with and without heat transfer", Journ. of Fluid Mech., Vol. 18, p. 117, (1964).
- Spl Spitzer, L., Jr., "The physics of fully ionized gases", Interscience, New York, (1956).
- Stal Proc. of the Stanford Conference on Computation of turbulent boundary layers, Stanford Univ., Stanford, Cal., (1968).
- Sul Sutton, G.W. and Sherman, A., "Engineering Magnetohydrodynamics", Mc. Graw Hill, New York, (1965).
- Tal Takeshita, T. and Grossman, L.M., "Excitation and ionization processes in non-equilibrium MHD plasmas", Proc. of the 4th Int. Conf. on MHD, Vol. 1, p. 191, Warsaw, (1968).
- Tel Teno, J. et al., "Boundary layers in MHD generators", Proc. of the 10th Symp. on Eng. Asp. of MHD, p. 15, Cambridge, Mass., (1969).
- Tsl Tseng, R.C. and Talbot, L., "Flat plate boundary layer studies in a partially ionized gas", AIAA Journ., Vol. 9, p. 1365, (1971).
- Veel1 Veefkind, A. et al., "Noble gas MHD generator experiments at low stagnation temperatures", Proc. of the 17th Symp. on Eng. Asp. of MHD, p. H.3, Stanford, Cal., (1978).
- Veel2 Veefkind, A., "Non-equilibrium phenomena in a disc-shaped Magnetohydrodynamic generator", Ph.D. thesis, Eindhoven Univ. of Techn., Eindhoven, (1970).
- Veel3 Veefkind, A., "Empirical model of the performance of closed cycle MHD channels derived from shock-tunnel experiments", Shock-tunnel MHD project Internal report 83/19, Eindhoven Univ. of Techn., Eindhoven, (1983).
- Wal Walz, A., "Boundary layers of flow and temperature", MIT press, Cambridge, Mass., (1969).
- Wh1 White, F.M., "Viscous Fluid Flow", Mc. Graw Hill, New York, (1974).
- Wh2 White, F.M. and Christoph, G.H., "A simple theory for the two-dimensional compressible turbulent boundary layer", Journ. Basic Eng., Trans. ASME, Vol. 94, p. 636, (1972).
- Zal Zauderer, B. et al., "Design of a 50 Mwt closed MHD blow-down experiment", EPRI final report RP233, Electric Power Research Institute, Palo Alto, Cal., (1975).

Appendix A Useful relations between boundary layer thicknesses and parameters

The relations will be obtained for the simple case of a non-MHD boundary layer by using the following simple profiles

$$\frac{u}{u_{\infty}} = \xi^{1/N} \quad ; \quad \frac{H - H_W}{H_{\infty} - H_W} = 1 - \alpha + \alpha \frac{u}{u_{\infty}} \quad (\text{A-1})$$

where the parameter ξ has been defined in equation (2.57). The following relations result from direct integration after substitution of equations (A-1) into the various definitions:

$$\delta_1 \equiv \int_0^{\delta} \left(1 - \frac{\rho u}{\rho_{\infty} u_{\infty}}\right) dy = \delta - \delta' \int_0^1 \frac{u}{u_{\infty}} d\xi = \delta - \frac{N}{N+1} \delta' \quad (\text{A-2})$$

$$\begin{aligned} \delta &= \int_0^{\delta} dy = \int_0^{\delta'} \frac{\rho_{\infty}}{\rho} dy' = \delta' \int_0^1 \frac{T}{T_{\infty}} d\xi = \\ &= \delta' \left\{1 - \frac{\alpha}{N+1} + \frac{T_W}{T_{\infty}} \frac{\alpha}{N+1} + \frac{M_{\infty}^2}{3} \left(\frac{2}{N+2} - \frac{\alpha}{N+1}\right)\right\} \end{aligned} \quad (\text{A-3})$$

$$\delta_2 \equiv \int_0^{\delta} \frac{\rho u}{\rho_{\infty} u_{\infty}} \left(1 - \frac{u}{u_{\infty}}\right) dy = \delta' \int_0^1 \frac{u}{u_{\infty}} \left(1 - \frac{u}{u_{\infty}}\right) d\xi = \frac{N\delta'}{(N+1)(N+2)} \quad (\text{A-4})$$

$$\delta_3 \equiv \int_0^{\delta} \frac{\rho u}{\rho_{\infty} u_{\infty}} \left(1 - \frac{u^2}{u_{\infty}^2}\right) dy = \frac{2N}{(N+1)(N+3)} \delta' \quad (\text{A-5})$$

$$\delta_H \equiv \int_0^{\delta} \frac{\rho u}{\rho_{\infty} u_{\infty}} \left(1 - \frac{H - H_W}{H_{\infty} - H_W}\right) dy = \alpha \frac{N}{(N+1)(N+2)} \delta' \quad (\text{A-6})$$

When the situation is considered of MHD boundary layers described by the profiles discussed in section 2.6.3, a substitution of these profiles into the definitions also leads to integrals which can be worked out analytically. In this way algebraic expressions for $\delta_{1,e}$, $\delta_{1,i}$ etc. can be obtained according to the same rules as outlined above.

Samenvatting

In dit proefschrift zijn de gasdynamische processen in MHD generatoren zowel theoretisch als experimenteel onderzocht. Deze processen worden sterk beïnvloed door de grootte van de magnetische interactie in de MHD generator. Het experimentele deel van de studie is uitgevoerd aan de 5 Mht "blow-down" installatie die bij de Technische Hogeschool Eindhoven in bedrijf is. Het profiel van de gemeten statische druk vertoont een sterke toename in de tweede helft van de generator tengevolge van de MHD interactie. Dit verloop kan worden verklaard door het optreden van dikke grenslagen. Een dergelijke situatie kan echter niet worden beschreven met het gebruikelijke quasi-ééndimensionale model, waarin de effecten van wrijving en warmtegeleiding over de omtrek van de dwarsdoorsnede zijn uitgesmeerd. Daarom is een model ontwikkeld, waarin de hoofdstroming en de grenslagen gekoppeld worden berekend. Om een snel werkend computerprogramma te krijgen, dat geschikt is voor ontwerp berekeningen en parameter studies is de quasi-ééndimensionale benadering gebruikt. Berekeningen hebben aangetoond dat voor de beschrijving van de grenslagen 3 integraal vergelijkingen nodig zijn, als de MHD effecten in de grenslagen correct in rekening worden gebracht. Deze integraal vergelijkingen zijn in dit proefschrift afgeleid uitgaande van de basis vergelijkingen voor de verandering van impuls, kinetische energie en stagnatie enthalpie. Berekeningen met het ontwikkelde model hebben aangetoond dat het opgewekte elektrische vermogen wordt beperkt door het ontwerp van de bestaande installatie. Tevens zijn uit de berekeningen echter mogelijkheden naar voren gekomen om deze beperkingen te omzeilen. In het proces van confrontatie tussen theorie en experiment is gebleken dat met behulp van het ontwikkelde model tekortkomingen in de werking van de MHD generator kunnen worden aangetoond. In het bijzonder is hierbij gebleken dat de werking van de MHD generator tot nog toe niet optimaal is geweest tengevolge van het optreden van Hall kortsluiting. Enige aanbevelingen zijn gedaan voor nieuwe, speciale experimenten om te onderzoeken of Hall kortsluiting kan worden vermeden. Een volledige verificatie van de uitspraken van het ontwikkelde model zal moeten wachten op de resultaten van deze toekomstige experimenten.

Acknowledgement

The present investigation would not have been completed without the constant encouragement and the advice of Prof. dr. L.H.Th. Rietjens. I would like to thank Prof. dr. ir. J.A. Steketee for many stimulating discussions in particular those regarding the theoretical foundations of this thesis. The discussions with, the advices and the critical remarks of dr. ir. J.H. Blom were of great value to me and have strongly contributed to the quality of this thesis. I am indebted to ir. G. Huijgen and to ir. J.C. Krause who contributed to this work during the final phase of their M.Sc. study. Thanks are also due to my colleagues of the group Direct Energy Conversion for their critical and useful remarks at the scientific meetings.

The experimental results which have been presented, were produced by a large number of people forming the blow-down society. For their friendship and cooperation I want to thank all of them.

I am very grateful to miss J.T.P. Daams, mrs. C.C.M. de Jong-Vriens and mrs. M.L. Spronck-Konings for carefully typing the manuscript and for keeping strictly to the planning. The contributions of mr. H.J. Mennen to the drawings are gratefully acknowledged.

Curriculum Vitae

De schrijver van dit proefschrift werd geboren op 27 september 1934 te Amsterdam. Na de lagere school bezocht hij de H.B.S. te Alkmaar waar in 1953 het eindexamen H.B.S.-B werd afgelegd. Hierna zette hij zijn studie voort aan de H.T.S. te Haarlem, studierichting Vliegtuigbouwkunde, waarvan het eindexamen in 1956 werd behaald. Na twee jaar militaire dienst trad hij in 1958 in dienst van het Nationaal Lucht- en Ruimtevaart Laboratorium te Amsterdam, waar hij zijn liefde voor wetenschappelijk onderzoek ontdekte. Hierdoor gemotiveerd pakte hij in september 1960 opnieuw zijn studie op en bezocht hij de Technische Hogeschool te Delft, studierichting Vliegtuigbouwkunde. Na het behalen van het kandidaatsexamen in juni 1963 studeerde hij een jaar aan de University of Michigan, Ann Arbor, U.S.A., waar hij voor het eerst met het onderwerp MHD kennis maakte. Zijn afstudeerwerk werd uitgevoerd onder leiding van Prof. dr. ir. J.A. Steketee en behandelde een onderwerp uit de theoretische stromingsleer. Het ingenieursdiploma werd hem uitgereikt in februari 1965, waarna hij als wetenschappelijk medewerker bij de groep van Prof. dr. ir. J.A. Steketee in dienst trad. Eind 1967 veranderde hij van werkkring en trad in dienst als wetenschappelijk medewerker bij de groep Direkte Energie Omzetting van de Afdeling der Elektrotechniek, Technische Hogeschool Eindhoven. Zijn werk onder leiding van Prof. dr. L.H.Th. Rietjens leidde tot dit proefschrift.

STELLINGEN

1. Drukmetingen vanuit één wand van een gesegmenteerde Faraday generator geven onvoldoende inzicht in het gasdynamisch gedrag.

Dit proefschrift, hoofdstuk 5.

2. Bij een MHD generator met hete wanden werken correlatie technieken goed als de generator slecht werkt.

Dit proefschrift, hoofdstuk 4.

3. De resultaten van de THE blow-down generator komen goed overeen met de relatie die door Demetriades voor open cyclus MHD generatoren is gevonden, mits het verschil in soortelijke warmte bij constante druk tussen open cyclus en gesloten cyclus omstandigheden in rekening wordt gebracht.

Demetriades, S.T. et al., Proc. of the 21st Symp. on Eng. Asp. of MHD, p. 3.1, Argonne, Ill., (1983).

4. Het doorrekenen van een discus-generator werkend met volledig geïoniseerd inzaai materiaal is veel eenvoudiger dan het aantonen van de praktische uitvoerbaarheid van dit concept.

Shioda, S. et al., Proc. of the 7th Int. Conf. on MHD, Vol. II, p. 685, Boston (1980).

Massee, P., Proc. of the 19th Symp. on Eng. Asp. of MHD, p. 7.1, Tullahoma, Tenn., (1981).

5. Het cesium injectie systeem dat voor het THE blow-down experiment is ontwikkeld, kan eenvoudig worden opgeschaald.

6. Door de ontwikkelingen op het gebied van de informatica kan bij de energievoorziening niet alleen de productie maar ook de consumptie van elektrische energie geregeld worden zonder de vrijheid van de gebruikers te beknotten.

Schweeppe, F., IEEE Spectrum, July 1978, p. 42.

7. Een hogere efficiency van het universitair onderwijs had doeltreffender bevorderd kunnen worden door het invoeren van een selectie bij de toelating dan door het invoeren van de tweefasenstructuur.
8. Het enige dat de science citation index bij het beoordelen van onderzoekers oplevert, is een getal.
9. De situatie dat vele promovendi hun proefschrift afwerken in een periode dat zij een WW-uitkering genieten, dient als een uitwas te worden beschouwd.
10. Het Amerikaanse systeem waarbij na verkiezingen ook topambtenaren op ministeries worden vervangen, kan bij introductie in Nederland gunstige effecten hebben.
11. Het aantrekkelijke van dorpspolitiek is dat een gering politiek inzicht gecompenseerd kan worden door een grote familie.
12. Als men bij regeringszaken net zo'n grondige aanpak zou hebben als bij de wisselteelt van een biologische tuin, dan zou het beleid al veel duidelijker zijn.